Quantum Hall effect in interacting fermionic lattice models

Leo Stenzel

München, 2020

Quantum Hall effect in interacting fermionic lattice models

Dissertation

an der Fakultät für Physik

der Ludwig-Maximilians-Universität München

vorgelegt von

Leo Johannes Martin Stenzel

aus Starnberg

München, den 29. Oktober 2020

Erstgutachter: Prof. Dr. Ulrich Schollwöck
Zweitgutachter: Prof. Dr. Monika Aidelsburger
Abgabedatum: 29. Oktober 2020
Datum der mündlichen Prüfung: 18. Dezember 2020

Kurzfassung

Die Entdeckung des Quanten-Hall (QH) Effekts stellt die erste Beobachtung von topologischen Phasen in Quantensystemen dar: Physikalische (Transport-) Eigenschaften eines Festkörpers nehmen exakt ganzzahlige Werte an, unabhängig von mikroskopischen Details des Materials. Symmetriegeschützte topologische Zustände wurden mittlerweile vollständig klassifiziert und weitere topologische Ordnungen im Experiment beobachtet. Fragen bezüglich des Zusammenspiels von topologischen Eigenschaften und starker Teilchen-Wechselwirkung bleiben jedoch unbeantwortet: Interaktionen liegen dem fraktionalen QH-Effekt zugrunde und es wird vermutet, dass sie anyonische Anregungen hervorrufen können. Ultrakalte Atome in optischen Gittern bieten vielversprechende Möglichkeiten, um diese Theorien zu überprüfen. Die Realisierung topologischer Bandstrukturen und starker Wechselwirkung in diesen Experimenten stellt jedoch nach wie vor Schwierigkeiten dar.

In dieser Arbeit untersuchen wir alternative Wege, um topologische Eigenschaften in Vielteilchensystemen zu realisieren und zu messen. Unserem Ansatz liegt die Analogie von 2D QH-Modellen, wie dem Hofstadter-Modell, und Familien von 1D Systemen, also topologischen Pumpen, zugrunde. Mittels numerischer Methoden untersuchen wir, ob es ähnliche Zusammenhänge in stark interagierenden Systemen gibt. Wir verwenden den DMRG Algorithmus, um Grundzustände wechselwirkender Gittermodelle zu finden. Dadurch beobachten wir Quantenphasenübergänge von einzelnen, endlichen Modellen, sowie topologische Phasenübergänge der Familien von Grundzuständen.

Der erste Teil beschäftigt sich mit Familien von 1D Modellen. Wir stellen fest, dass das Hinzufügen von Wechselwirkungen zu Mott-isolierenden Phasen für halbgefüllte Bänder führt, welche nicht triviale topologische Eigenschaften haben können. Außerdem beobachten wir, dass Teilchen-Interaktion bereits existierende topologische Eigenschaften ändern kann: Einige Systeme unserer Familie entsprechen dem AB_2 ionischen Hubbard-Modell, welches einen wechselwirkungsbedingten, zweifachen Phasenübergang zu einem stark korrelierten Isolator aufweist. Für starke Wechselwirkungen ist die transportierte Ladung auch topologisch quantisiert, jedoch ändern sich Vorzeichen und Betrag der Chern-Zahl. Wir bestimmen den topologischen Index durch numerische Integration der Vielteilchen Berry-Krümmung und zeigen, dass er auch mittels des Massenzentrums gemessen werden kann.

Im zweiten Teil behandeln wir die Beziehung von interagierenden 1D Ladungspumpen und wechselwirkenden 2D QH-Modellen. Um beide Systeme numerisch zu untersuchen betrachten wir das Hofstadter-Modell auf einem Zylinder und drücken es in gemischter Real- und Impulsraumbasis aus. In dieser können wir die Verbindung der interagierenden 1D und 2D Modelle parametrisieren. Die zylindrische Geometrie erlaubt uns außerdem topologische Eigenschaften zu bestimmen, indem wir permanente Ströme als Antwort auf ein lineares Potential berechnen. Wir können den topologischen Übergang der 1D Ladungspumpen reproduzieren, aber das Hofstadter-Hubbard-Modell bleibt durch einen topologischen Phasenübergang von stark wechselwirkenden 1D Systemen getrennt. Zwischen den 1D und 2D Hubbard Modellen finden wir ferromagnetische Grundzustände, welche einige topologische Eigenschaften erklären könnten.

Abstract

The discovery of the quantum Hall effect marks the first observation of quantum systems with topological properties: Physical observables, typically related to transport, of a solid-state system take exactly integer-quantized values, regardless of material properties or microscopic details. Today, symmetry-protected topological phases have been fully classified, and other topological orders have also been observed in experiments. However, there are open questions about the interplay of topological properties and strong particle interaction: Interactions are at the heart of the fractional quantum Hall effect, and are conjectured to give rise to anyonic excitations. Ultracold atoms in optical lattices promise to be the highly controllable experimental platform to test these theoretical predictions. However, realizing topological band structures with strong particle interactions in these experiments remains challenging.

In this thesis, we research alternative pathways to realizing and measuring topological properties in many-body systems. Our approach is based on the analogy of 2D quantum Hall models, e.g. the Hofstadter model, and families of 1D Hamiltonians, i.e., topological charge pumps. We study numerically, whether we can find a correspondence of 1D and 2D models as strong particle interactions are added. We use the DMRG algorithm to find ground states of interacting lattice models. Thus, we can observe quantum phase transitions of individual finite-size models, and topological phase transitions of families of ground states.

The first part of this thesis considers families of one-dimensional models. We find that introducing interactions creates Mott-insulating phases for half-filled bands, which can exhibit nontrivial topological properties. Furthermore, we find that particle interaction can also change existing topological properties: Some Hamiltonians of our family correspond to the AB_2 ionic Hubbard model, which is known to have an interaction-driven, two-fold quantum phase transition towards a strongly correlated insulator. For strong interactions, the pumped charge remains topologically quantized, but sign and magnitude of the Chern number change. We compute the topological index by numerically integrating the many-body Berry curvature, and we show how it can also be obtained from center-of-mass measurements.

In the second part, we discuss the relation of interacting 1D charge pumps and interacting quantum Hall models. To study both systems numerically, we put the Hofstadter model on a cylinder, and express it in a mixed real- and momentum-space basis. Thereby, we can parameterize the connection of the interacting 1D and 2D models. Furthermore, the cylindrical geometry allows us to probe topological properties by computing persistent Hall currents as response to a linear potential. We can reproduce the topological transition found in the interacting 1D charge pumps, but find that the Hofstadter-Hubbard model is separated by a topological phase transition from strongly-interacting 1D systems. Between the one- and two-dimensional Hubbard limits, we find models with a ferromagnetic ground state, which could explain some topological properties.

Publications

This work is based on the following publications.

Editors' Suggestion

Quantum phases and topological properties of interacting fermions in one-dimensional superlattices

L. Stenzel, A. L. C. Hayward, C. Hubig, U. Schollwöck, and F. Heidrich-Meisner

Phys. Rev. A **99**, 053614 (2019) [1]

The realization of artificial gauge fields in ultracold atomic gases has opened up a path towards experimental studies of topological insulators and, as an ultimate goal, topological quantum matter in many-body systems. As an alternative to the direct implementation of two-dimensional lattice Hamiltonians that host the quantum Hall effect and its variants, topological charge-pumping experiments provide an additional avenue towards studying many-body systems. Here, we consider an interacting two-component gas of fermions realizing a family of one-dimensional superlattice Hamiltonians with onsite interactions, and a unit cell of three sites, the ground states of which would be visited in an appropriately defined charge pump. First, we investigate the grand-canonical quantum phase diagram of individual Hamiltonians, focusing on insulating phases. For a certain commensurate filling, there is a sequence of phase transitions from a band insulator to other insulating phases (related to the physics of ionic Hubbard models) for some members of the manifold of Hamiltonians. Second, we compute the Chern numbers for the whole manifold in a many-body formulation, and show that, related to the aforementioned quantum phase transitions, a topological transition results in a change of the value and sign of the Chern number. We provide both an intuitive and a conceptual explanation, and argue that these properties could be observed in quantum-gas experiments.

Editors' Suggestion

Topological phases in the Fermi-Hofstadter-Hubbard model on hybrid-space ladders

L. Stenzel, A. L. C. Hayward, U. Schollwöck, and F. Heidrich-Meisner

Phys. Rev. A **102**, 023315 (2020) [2]

In recent experiments with ultracold atoms, both two-dimensional (2D) Chern insulators and one-dimensional topological charge pumps have been realized. Without interactions, both systems can be described by the same Hamiltonian, when some variables are being reinterpreted. In this paper, we study the relation of both models when Hubbard interactions are added, using the density-matrix renormalization-group algorithm. To this end, we express the fermionic Hofstadter model in a hybrid-space representation, and define a family of interactions, which connects 1D Hubbard charge pumps to 2D Hubbard Chern insulators. We study a three-band model at particle density $\rho = 2/3$, where the topological quantization of the 1D charge pump changes from Chern number $C = 2$ to $C = -1$ as the interaction strength increases. We find that the $C = -1$ phase is robust when varying the interaction terms on narrow-width cylinders. However, this phase does not extend to the limit of the 2D Hofstadter-Hubbard model, which remains in the $C = 2$ phase. We discuss the existence of both topological phases for the largest cylinder circumferences that we can access numerically. We note the appearance of a ferromagnetic ground state between the strongly interacting 1D and 2D models. For this ferromagnetic state, one can understand the $C = -1$ phase from a band-structure argument. Our method for measuring the Hall conductivity could similarly be realized in experiments: We compute the current response to a weak, linear potential, which is applied adiabatically. The Hall conductivity converges to integer-quantized values for large system sizes, corresponding to the system's Chern number.

Contents

List of symbols

In alphabetical order.

$\boldsymbol{\mathcal{A}}$	Berry connection
α	magnetic flux $\alpha = p/q$ per plaquette in the Hofstadter model, or superlattice wave number in a charge pump
$\hat{\boldsymbol{c}}^\dagger$	$SU(2)$-invariant fermionic particle creator
C	Chern number
χ_{Hall}	linear Hall current response
δ	superlattice phase (in chapter 3), or angle of twisted boundaries (in chapter 4)
Δ	many-body energy gap, cf. section 2.2.1 for definitions
E	energy
$\boldsymbol{\epsilon}$	electric field
$\mathcal{F}$	Berry curvature
$\hat{\boldsymbol{j}}$	current density operator
$\boldsymbol{k}$	quasimomentum coordinate
K	total quasimomentum, i.e., $\mathbb{Z}_W$ symmetry label of a many-body state
L	linear system size
m	MPS bond dimensions
M_i	MPS tensor on site i
μ	chemical potential
N	total particle number
ν	band index
p	numerator of α
q	denominator of α, i.e., number of Hofstadter bands
ρ	particle density, i.e., $N/(LW)$; Electrical resistivity in chapter 1
S	total spin, i.e., $SU(2)$ symmetry label
σ	label of spin-$1/2$ degree of freedom; Also, electrical conductivity in chapter 1
$t_{[y]}$	tunneling rate [along y]
τ	time (in units t^{-1})
θ	angle of twisted boundaries in chapter 3
U	interaction strength; Also, voltage in chapter 1
V	potential strength: Superlattice potential in chapter 3, and weak, linear potential in chapter 4
W	width of 2D lattice, typically the circumference of a cylinder
x	real-space coordinate along L in lattice sites
y	real-space coordinate along W in lattice sites

Context & Outline

> I am struck by how important the use of stripped down toy models has been in discovering new physics. It also used to be thought that one-dimensional models were just "homework exercises" to be carried out before tackling the "real" three-dimensional systems. F. Duncan M. Haldane [3]

Forty years ago, the discovery of the quantum Hall effect [4] kick-started research in entirely new phases of matter: Quantum systems, comprising many particles, exhibit exactly integer-quantized physical properties, regardless of noise, or dirt, or other microscopic details. The robust properties of such systems were quickly related to the mathematical concept of topology—and the 2016 Nobel Prize in physics honored theoretical contributions to *topological quantum matter* [5].

The first part of chapter gives a brief, historical review of topology in condensed matter physics. The aspects which are relevant for understanding this thesis will be discussed in more detail in chapter 1. The second section touches on the recent progress in realizing topological phases in ultracold-atom experiments. These very clean, and highly controllable quantum systems allow for experimental implementations of theoretical "toy models", and are the main motivation for this work.

Topological quantum matter

This section is based on the Nobel lecture by F. Duncan M. Haldane [3], who reviewed the historical development of this research field. After the surprising experimental discovery of robust, integer-quantized plateaus of the Hall conductivity in 1980 [4], many discoveries were made in a short time span. Arguably, experimental progress was quicker than the theoretical research: Tsui, Störmer, and Gossard [6] discovered fractionally-quantized Hall conductivity merely two years later. However, the rich physics associated with this effect is beyond the scope of this thesis. We will only briefly discuss possible generalizations of our methods to fractionally-quantized states in section 5.2.

The unexpected observation in the experiment by Klitzing et al. [4] was that the conductivity is *totally* insensitive to changes of charge carrier density. A naive explanation using Landau levels, as we will show in section 1.2, would expect that the number of charges has to match the number of states in the relevant level perfectly in order to observe such results. While modern experimental methods might allow for such precisely tuned configurations, it is clearly an unreasonable assumption for solid-state physics.

On the theoretical side, it was quickly realized that disorder in the sample is the reason behind quasi-perfectly ($1 : 10^9$) quantized conductivity. Disorder allows for localized states, which can be occupied by spare charges. Laughlin [7] made his famous argument for the gauge invariance of the localized states, such that the conductivity cannot change while a mobility gap exists. In 1982, Halperin [8] extended Laughlin's analysis, and noticed the importance of current-carrying states at the edge of the clean sample. To some extend, edge states can be understood as semi-classical skipping orbits, but they are key to the topological properties, due to the bulk-edge correspondence [9].

In the same year, Thouless, Kohmoto, Nightingale, and den Nijs (TKNN) [10] took a different route, and were able to relate *bulk* properties to a topological invariant. They performed calculations for the Hofstadter model [11], which was an odd choice at the time: The model rather applies to magnetic fields which are much stronger than realizable in solid-state systems. TKNN also did not include disorder in the Hamiltonian. Thus, despite the topological nature of the TKNN invariant, their result is not robust under changes of the carrier density. Nowadays, different implementations of artificial gauge fields allow for the experimental realization of the Hofstadter model [12–14]. This motivates us to choose a similar setting as TKNN, and we will discuss their derivation in section 1.4.

This thesis will not follow the historical order, and we will first introduce topology via the Berry phase in section 1.3. Berry's paper was only published in 1984 [15], but the relation of the TKNN invariant and Berry's was quickly discovered by Simon [16]. Actually, Simon's paper was published already in 1983, because Berry [15] was held up by the referees [17]. These relations give us the Berry curvature, an analog of the magnetic field in parameter, or momentum space. Its integral over a closed manifold then yields the topological invariant, i.e., the Chern number.

So far, topological properties were only known in "esoteric, field-dependent" models (quote: Haldane [3]), like the Hofstadter model. However, in 1988 Haldane realized that a net magnetic field is not necessary for a non-trivial Chern number, but that it is sufficient to break the time-reversal symmetry. At the time, the Haldane model [18] was no less of a toy model than the Hofstadter model, but today it has also been realized experimentally [19, 20].

Haldane's model also served as inspiration for the discovery of a new class of symmetry-protected topological (SPT) phases. In 2005, Kane and Mele [21] proposed a time-reversal symmetric model by basically combining conjugate copies of the Haldane model for each spin species. Due to preservation of time-reversal symmetry its Chern number must vanish, as does the charge Hall current. However, the *helical* edge modes are preserved, and can be related to a $\mathbb{Z}_2$ topological invariant. This in turn relates to quantized *spin* Hall conductivity. The quantum spin Hall effect [22] was soon after discovered by König et al. [23] in 2007. We note that combining conjugate Chern insulators is too simplistic: Realistic Hamiltonians which describe the quantum spin Hall effect contain spin-orbit coupling [24], such that the total spin is not a good quantum number.

The subsequent research on topological insulators is beyond the scope of this introduction. However, we want to comment on the use of definitions: Commonly, "topological insulator" is only used for models without an external magnetic field, and similarly "Chern insulator" may only be used for models exhibiting the quantum *anomalous* Hall effect. We think that these definitions do not really apply to the setting in cold-atom gases, because each term in the Hamiltonian has to be engineered, anyway. We will use "Chern insulator" more inclusively for any quantum phase which is associated to a non-trivial Chern number.

Today, the classification of SPT phases has been completed [25]. But the interplay of particle interactions and topological properties remains of research interest thanks to new experimental methods to engineer Hamiltonians.

Topological phases in ultracold-atom gases

The lattice models studied in this thesis are not directly targeted at particular experimental realization. The Hamiltonians are rather clean "toy models", and additional terms, like traps or disorder, would have to be considered to describe real physical systems. However, we are very much motivated by the recent progress in quantum simulation using ultracold atomic gases in optical lattices.

The main advantage of engineering Hamiltonians for cold-atom gases over solid-state materials is the ability to tune particle interactions [26, 27]. In particular onsite, Hubbard interactions, which are also of some theoretical interest, are commonly implemented. While there are other approaches to quantum simulation of topological models, they tend to be more limited than ultracold atoms: Photonic systems have been used to realize a number of topological Hamiltonians [28]—however, there is currently no way to implement interactions. Superconducting qubits have also been used as quantum simulator of topological systems [14, 29]. While qubits promise to be the most versatile approach to quantum simulation, the accessible system sizes are currently very limited.

In order to implement a topological band structure in cold-atom experiments [30], one typically has to engineer complex tunneling amplitudes in a 2D lattice [31–33]. Artificial gauge fields can for example be realized using laser-assisted tunneling in order to imprint phases [34]. The 2D Hofstadter Hamiltonian was implemented in real space using this method [12, 13, 35].

Since this approach requires laser-driven coupling between adjacent lattice sites, one can rethink the idea of dimensionality, and use e.g. spin [36] or momentum [37] as a *synthetic dimension*. The number of sites along the synthetic dimension is typically limited, but the edge states, due to their topological nature, are preserved [38]. These chiral edge modes were observed using the spin degree of freedom as a synthetic dimension [37, 39–41]. Furthermore, limited number of spin states can be mitigated by using periodic boundaries [42]. Synthetic-dimensional optical lattices have also been used to simulate spin-orbit coupling [43–47].

A different approach to realizing artificial gauge fields is based on *Floquet engineering* [48, 49]. Applying a periodic force to a cold-atom system can yield an effective, time-independent Hamiltonian which may include gauge fields [50]. This approach yielded experimental realizations of the Haldane model [19, 51, 52]. Due to the driving forces, the topological invariants in Floquet systems are defined on periodic quasienergy bands with no exact analog in energy-conserving systems [53, 54].

So far, most experiments have been performed with either non-interacting particles or hard-core interactions. In this case, the topological properties also exists in a family of lower-dimensional Hamiltonians [55]. The resulting models often do not contain complex terms, potentially simplifying the experimental setup. In realizations of parameterized models, the Zak phase obtained through shifting superlattice potentials was measured [56], as well as the Berry phase gained by moving a wave packet around a Dirac cone [57].

As we will discuss in section 1.5.2, families of 1D periodic lattices can also represent topological charge pumps, which have been realized with ultracold atoms [58, 59]. The concept of reducing physical dimensions while increasing the parameter space has been extended to simulate 4D quantum Hall physics [60]: Realizing a two-dimensional charge pump in optical lattices, the second Chern number [61] can be measured [62].

Having argued that both interactions and topological bands can be realized in ultracold-atom experiments, it is the next logical step to put both things together, and study the rich physics of interacting topological phases of matter [63]. Unfortunately, such experiments have so far only been performed in the few-body limit [64], or certain 1D systems [58, 65] due to heating: Implementations of complex tunneling rates typically do not conserve energy, and will therefore increase the temperature indefinitely [66, 67]. However, the relevant timescales depend on experimental parameters, and optimizing the lifetime of low-energy states in driven systems is a field of active research in ultracold atoms [68–74].

Outline

This thesis is structured as follows: Chapter 1 introduces the physics of the quantum Hall effect, and motivates the models studied in the following chapters. We start from the simplest description, i.e., Landau levels in section 1.2. Section 1.3 motivates the definition of the Berry curvature, and in section 1.4, we follow TKNN to derive a similar formula, albeit with different assumptions, and a different interpretation. We proceed to introduce the paradigmatic Hofstadter model in section 1.5, and discuss its topological band structure, as well as its relation to Thouless pumps.

Chapter 2 discusses our numerical methods. Primarily, we rely on the DMRG algorithm: We will only sketch this method in section 2.1, because implementing DMRG was not part of this thesis. Instead, we will discuss the numerical observables used throughout the following chapters in more detail in section 2.2. We will also touch on our methods to improving, and verifying convergence of the DMRG algorithm in section 2.3.

Chapter 3 and 4 discuss our numerical findings in one- and two-dimensional lattice models. In chapter 3, we restrict ourselves to strictly 1D systems. Topological properties are then defined for a family of models, which may be interpreted as a topological charge pump. We discuss insulating phases in 1D superlattice models in section 3.2, and recover the quantum phase transitions of the well-known ionic Hubbard model for some members of our family of Hamiltonians. We continue to discuss topological pumping in those interacting insulators in section 3.3. We find that interactions both create and change topological indices as the quantum phase transitions open and close many-body gaps. We try to give an intuitive explanation for our findings, and discuss whether these effects are observable in a cold-atom experiment.

In chapter 4, we proceed to studying two-dimensional descriptions of Hofstadter models. We show in section 4.2 that the 1D topological transitions, discussed in section 3.3, can also be observed as quantized Hall conductivity in a cylindrical geometry—albeit with an uncommon choice of particle interactions. We observe a topological transition as we go to the usual 2D Hofstadter-Hubbard model, which seems to remain adiabatically connected to the free Hofstadter model. In section 4.3, we find a region in our space interaction parameters where the ground state is ferromagnetic. Ferromagnetism has implications for topological properties, and this observation seems to support our intuitive argument from section 3.3. We conclude by extending our results to the isotropic Hubbard-Hofstadter model in section 4.4.

Chapter 5 discusses directions in which our research could be continued. A main open question is understanding the mechanism for the ferromagnetic ground state. In section 5.1, we propose a way to derive an effective model, which would rely on a particular choice of interaction terms. Section 5.2 discusses applying our numerical methods to fractional quantum Hall states. We show preliminary results for a simplified lattice model, and describe the problems which prevented us from obtaining more and better results.

1 A brief introduction to quantum Hall physics

This chapter introduces the quantum Hall effect and its relation to topology. It aims to give context to some concepts used in the rest of this thesis—but has no aspirations to be exhaustive. For a more in-depth introduction to quantum Hall physics, we recommend the lecture notes by David Tong [75], which are the basis for some parts of this chapter. However, many modern books on condensed-matter theory cover topological phases, and discuss the quantum Hall effect from different angles [76–79].

1.1 Quantum Hall effect

The quantum Hall effect was discovered by Klaus von Klitzing [4] in 1980, and he was awarded the Nobel Prize five years later [80]. Interestingly, he did not share the prize with any theoretical physicists who explained the effect. However, this discovery created a much larger field of theoretical research, which was acknowledged by the 2016 Nobel Prize. In this context, some original publications on quantum Hall physics were also referenced [5].

The measurements by Klitzing et al. [4] are shown in fig. 1.1. They were performed in a 2D electronic system at Helium temperatures, subject to a constant, perpendicular magnetic field. The current I along the long axis, parallel to U_{PP}, is also constant. The density of free electrons is controlled by, and proportional to, the gate voltage V_g.

The measurements of longitudinal voltage U_{PP}, and transversal Hall voltage U_H show notable features for the same carrier density: U_H takes a constant value while U_{PP} vanishes for some gate voltages V_g. On these plateaus, the Hall voltage takes the constant values

$$U_H = I \times \frac{1}{i}\frac{h}{e^2}, \quad i \in \mathbb{N}. \tag{1.1}$$

The measurements of U_H and U_{PP} directly relate to the resistivity tensor ρ: Assuming a homogeneous and isotropic medium, and applied electric field ϵ, the steady-state observables fulfill

$$\boldsymbol{\epsilon} = \begin{pmatrix} U_{PP}/L \\ U_H/W \end{pmatrix} = \rho \boldsymbol{j} = \begin{pmatrix} \rho_{xx} & \rho_{xy} \\ -\rho_{xy} & \rho_{xx} \end{pmatrix} \begin{pmatrix} I/W \\ 0 \end{pmatrix}, \tag{1.2}$$

which yields for a plateau, where $U_{PP} = 0$,

$$\rho_{xy} = -\frac{U_H}{I}, \quad \text{and} \quad \rho_{xx} = 0. \tag{1.3}$$

The fact that U_{PP} vanishes greatly improves the accuracy of the measurements of U_H at the respective plateaus. The aspect ratio L/W of the 2D Hall devices becomes irrelevant, as do any imperfections of the orthogonal alignment of the voltage probes [4, 81].

While formally equivalent, one sometimes prefers to study the conductivity tensor,

$$\sigma := \rho^{-1} = \frac{e^2}{h}\begin{pmatrix} 0 & i \\ -i & 0 \end{pmatrix}, \quad i \in \mathbb{N}. \tag{1.4}$$

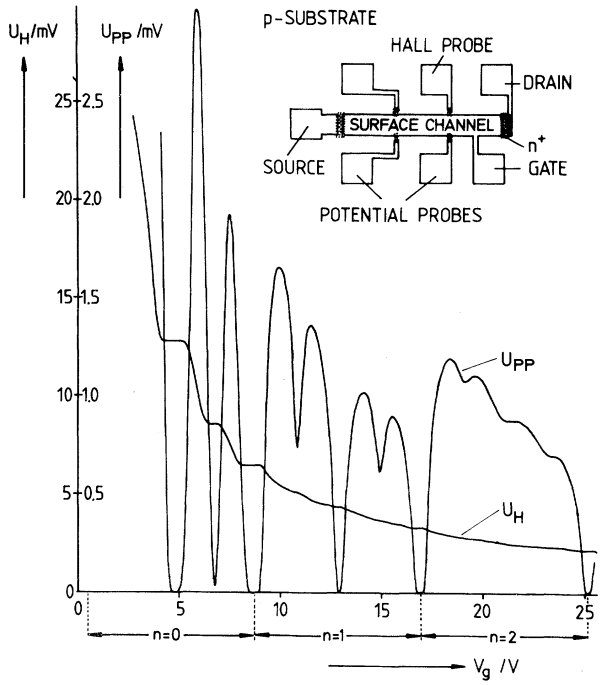

Figure 1.1: *Discovery of the quantum Hall effect by Klitzing et al. [4].* Hall voltages are measured at a constant current $I = 1\,\mu$A, such that the shown plateaus of U_H correspond to $R_H = \frac{1}{i}\frac{h}{e^2}$ for $i \in \{2, 3, 4, 6, 8, 12\}$. In this experiment, the magnetic field is constant at $B = 18$T, and the carrier concentration is directly proportional to the gate voltage V_g. The label n denotes the respective Landau levels, which are occupied four times due to spin and valley degree of freedom. The plateaus coincide with the vanishing voltage U_{PP}, parallel to the current I.

The fact that $\rho_{xx} = \sigma_{xx} = 0$ seems counterintuitive, the system is an insulator despite the constant current I. The catch is that the current is orthogonal to the voltage, therefore no work is performed on the system, and there is no dissipation.

1.2 Landau levels

The first ingredient to understanding quantized Hall conductivity is basic quantum mechanics: The motion of a charged particle in a magnetic field, cf. Landau and Lifschitz [82]. While the remaining chapters consider lattice models, we will start with a continuum description, and introduce the lattice in section 1.4.2.

The Hamiltonian for a particle with charge $-e$ and mass m subject to a magnetic field is given by minimal coupling,

$$\hat{H} = \frac{1}{2m}\left(\hat{\boldsymbol{p}} + e\hat{\boldsymbol{A}}\right)^2 , \tag{1.5}$$

where $\hat{\boldsymbol{A}}$ is the vector potential of the external field. Here, and in the rest of this work, we will restrict the particles' motion to the x-y plane, and apply an orthogonal magnetic field B. We will use the Landau gauge, such that

$$\hat{\boldsymbol{A}} = \begin{pmatrix} 0 & B\hat{x} & 0 \end{pmatrix}^T . \tag{1.6}$$

Noting that the Hamiltonian preserves momentum $\hat{p}_y$, we can express it in the respective basis, using eigenvalues $\hbar k_y$,

$$\hat{H} = \frac{1}{2m}\left(\hat{p}_x^2 + (\hbar k_y + eB\hat{x})^2\right) , \tag{1.7}$$

and find a set of 1D harmonic oscillators shifted in x by $-\frac{\hbar k_y}{eB}$. The eigenenergies are therefore given by

$$E_n = \frac{e\hbar B}{m}\left(n + \frac{1}{2}\right) , \tag{1.8}$$

and, interestingly, do not depend on k_y momentum. This indicates a macroscopic degeneracy of the energy levels. The allowed momenta k_y are restricted by the boundary conditions. Assuming that the centers of all oscillators need to be inside the 2D system of width W and length L, there is a second constraint,

$$k_y = \frac{2\pi}{W} \times n,\ n \in \mathbb{N}_0 , \qquad \text{and} \qquad k_y \leq \frac{eBL}{\hbar} , \tag{1.9}$$

such that the degeneracy D of each energy level is proportional to the system's surface,

$$D = \left\lfloor \frac{eBLW}{2\pi\hbar} \right\rfloor . \tag{1.10}$$

Applying an electric field

In order to induce a Hall current, we add a linear potential along the x direction, corresponding to an applied voltage $U = \epsilon L$,

$$\hat{H} - e\epsilon\hat{x} = \frac{1}{2m}\left(\hat{p}_x^2 + \left(eB\hat{x} + \hbar k_y - \frac{\epsilon m}{B}\right)^2\right) + \hbar k_y \frac{\epsilon}{B} - \frac{\epsilon^2 m}{2B^2} . \tag{1.11}$$

We will use a similar setup to compute Hall responses numerically in section 4.1.2. The electric field shifts the centers of the harmonic oscillators by $-\epsilon m/B$, polarizing the system. However, we can ignore such shift when we only care about bulk properties. The additional term which is linear in ϵ and k_y is more relevant: It lifts the degeneracy of each Landau level and creates a current along the y axis,

$$\langle \hat{v}_y \rangle_{\text{bulk}} = \langle \partial_\tau \hat{y} \rangle_{\text{bulk}} = \left\langle \frac{1}{i\hbar}\left[\hat{y}, \hat{H} - e\epsilon\hat{x}\right] \right\rangle_{\text{bulk}} = \frac{\epsilon}{B} , \tag{1.12}$$

where we denote the time by τ in order to avoid confusion with the tunneling rate t in the following chapters. Putting things together, we find for the current along the y axis of a fully occupied Landau level,

$$I = -e\,\langle \hat{v}_y \rangle\,\frac{D}{W} = -\frac{e^2}{h}U . \tag{1.13}$$

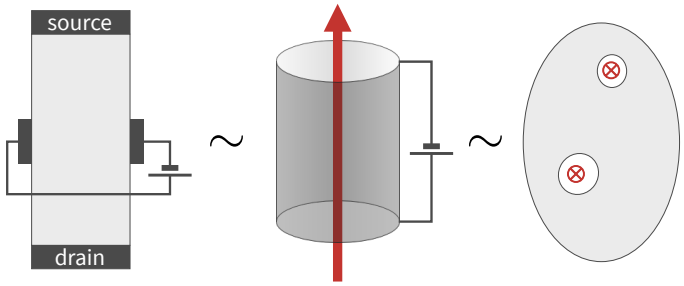

Figure 1.2: *Topology of a quantum-Hall experiment.* Considering the leads as part of the experiment (left), it can be understood as a flux-pierced disc or cylinder (center) as in Laughlin's argument [7]. It is topologically equivalent to a domain with two flux-pierced holes (right), as considered by Avron and Seiler [85]. Illustration inspired by Avron and Seiler [85].

This matches the Hall voltage U_H in eq. (1.1), measured for each plateau—Landau levels can give the correct value for the quantized Hall conductivity. However, that is not what makes the data in fig. 1.1 remarkable. The fact that $U_H(V_g)$ exhibits plateaus, which do not depend on the precise particle number, is something Landau levels cannot explain.

In short, the great precision of the quantized plateaus is actually due to disorder in the sample, and the localized states it creates. We do not actually consider disorder in this thesis, because we are rather interested in experimental realizations with ultracold atoms: Optical lattices are pretty much perfectly clean and periodic, and in order to realize disorder, aperiodic optical potentials have to be added [83, 84]. Therefore, we do not expect to observe Hall plateaus in our numerical simulations. However, the robustness of the Hall plateaus can be understood in terms of the system's topology, which we will discuss in the following sections.

1.3 Berry phase

In order to define topological quantities, we need to talk about boundary conditions. They are at the heart of the famous argument by Laughlin [7], why localized states do affect quantized conductivity: It relies on using a geometry which is periodic in y, a Corbino ring, such that flux can be threaded though its center. Changing the flux adiabatically pumps extended states from one side to the other, while localized states are unaffected. We will come back to topological charge pumping in section 1.5.2.

Assuming certain boundary condition might be unsatisfying, physically. However, as pointed out by Avron and Seiler [85], the experimental setup of fig. 1.1 is not topologically trivial: When the connections of source and drain, as well as the Hall probes are taken into account, one ends up with a toroidal geometry, see fig. 1.2. Using a cylindrical geometry, we may thread a flux δ trough the hole, equivalent to introducing a twist angle to the periodic boundaries. We assume that we can increase the flux adiabatically, and that the system is gapped for all values of δ. Under these circumstances, the adiabatic theorem tells us that the system needs to return to the initial state as $\delta \to \delta + 2\pi$.

When we say that the system returns to its initial state after a cyclic and adiabatic evolution, we mean that the final state is in the same equivalence class: There can always be a complex phase ϕ, which usually is physically irrelevant,

$$|\psi\rangle \xrightarrow[\text{adiabatically}]{\delta \to \delta+2\pi} \mathrm{e}^{i\phi} |\psi\rangle \ . \tag{1.14}$$

In order to calculate the phase, we introduce an instantaneous eigenbasis $\{|\psi_n(\delta)\rangle\}$ for each δ,

$$\hat{H}(\delta) |\psi_n(\delta)\rangle = E_n(\delta) |\psi_n(\delta)\rangle \ . \tag{1.15}$$

We prepare a state $|\psi(\tau = 0)\rangle$ in an eigenstate $|\psi_n(\delta)\rangle$ for $\delta = \delta(\tau = 0)$. Assuming that state is gapped for the entire evolution, $|\psi(\tau)\rangle$ will remain in the nth eigenstate, but will acquire a complex phase,

$$|\psi(\tau)\rangle = \exp\left(\frac{-i}{\hbar}\int_0^\tau \mathrm{d}\tau' E\left(\delta\left(\tau'\right)\right)\right) \mathrm{e}^{i\gamma(\tau)} |\psi_n(\delta(\tau))\rangle \ . \tag{1.16}$$

The first exponential is just the time evolution of the eigenstate. But there is an additional, geometric phase γ, related to the change of eigenstates with respect to δ. This is known as the Pancharatnam-Berry phase [15, 86], and we can find an expression for it by plugging our ansatz, eq. (1.16), into the Schrödinger equation,

$$\frac{\mathrm{d}\gamma}{\mathrm{d}\tau} = i \langle \psi_n(\delta) | \partial_\delta \psi_n(\delta)\rangle \frac{\mathrm{d}\delta}{\mathrm{d}\tau} \, . \tag{1.17}$$

Here, we have assumed that $|\psi_n(\delta)\rangle$ is differentiable, putting some constraints on the gauge choices. However, this will not be relevant for us studying only finite differences numerically in section 2.2.3. More importantly, eq. (1.17) is not uniquely defined, as it depends on the gauge chosen for $|\psi_n(\delta)\rangle$. But that is okay, in the end, we are only interested in the phase after completing a closed loop $\mathcal{C}$ in parameter space,

$$\gamma(\mathcal{C}) = \oint_{\mathcal{C}} \mathrm{d}\delta \underbrace{i \langle \psi_n(\delta) | \partial_\delta \psi_n(\delta)\rangle}_{=:\mathcal{A}_n(\delta)} \, . \tag{1.18}$$

We see that the phase does not depend on time τ anymore, assuming that the evolution is adiabatic. Therefore, we may define the *Berry connection* $\mathcal{A}_n(\delta)$, which is time-independent, but depends on gauge.

1.3.1 Berry curvature

In order to define further physical, i.e., gauge-invariant quantities we have to consider a higher-dimensional parameter space. We will take a family of Hamiltonians $\hat{H}(\boldsymbol{\delta})$, parameterized by a vector of parameters $\boldsymbol{\delta} \in \mathbb{P} \subset \mathbb{R}^d$.

As a consequence, the Berry connection $\boldsymbol{\mathcal{A}}$ also becomes a vector. Once more assuming differentiability of the ground state w.r.t. $\boldsymbol{\delta}$, we find,

$$\boldsymbol{\mathcal{A}}(\boldsymbol{\delta}) := i \langle \psi(\boldsymbol{\delta}) | \nabla_{\boldsymbol{\delta}} \psi(\boldsymbol{\delta})\rangle \ . \tag{1.19}$$

Under reasonable assumptions on our parameter space $\mathbb{P}$, we can rewrite the path integral over $\mathcal{C} = \partial\mathcal{S}$ into an integral over the surface it encloses. Here, the fact that we considered $\boldsymbol{\delta}$ in a d-dimensional parameter space comes back to bite us: We are used to the same procedure, expressing the magnetic field $\boldsymbol{B} = \nabla \times \boldsymbol{A}$ in terms of its vector potential. But this vectorial definition only works in 3D.

We will briefly work in the d-dimensional case, but in the rest of this thesis we will only explicitly consider the parameter space spanned by two flux piercings $\mathbb{P} = \mathbb{T}^2$. Understanding of differential geometry will not be required, though we may recommend the book by Hubbard and Hubbard [87] to the avid reader. Using the generalized Stokes' theorem, we find

$$\gamma = \oint_{\partial\mathcal{S}} \sum_i \mathcal{A}_i(\boldsymbol{\delta})\,\mathrm{d}\delta_i = \int_{\mathcal{S}} \mathrm{d}\left(\sum_i \mathcal{A}_i(\boldsymbol{\delta})\,\mathrm{d}\delta_i\right) = \int_{\mathcal{S}} \sum_{ij} \frac{\partial \mathcal{A}_i(\boldsymbol{\delta})}{\partial \delta_j}\,\mathrm{d}\delta_j \wedge \mathrm{d}\delta_i\,. \tag{1.20}$$

We can thus introduce the *Berry curvature* as the field, which is integrated over $\mathcal{S}$. Typically, the tensorial Berry curvature is defined in an antisymmetrized way [75, 88],

$$\mathcal{F}_{ij}(\boldsymbol{\delta}) = \frac{\partial \mathcal{A}_j}{\partial \delta_i} - \frac{\partial \mathcal{A}_i}{\partial \delta_j}\,. \tag{1.21}$$

The Berry curvature $\mathcal{F}$ has the desired properties of a field, i.e., it is local in $\mathbb{P}$ (unlike $\gamma(\mathcal{C})$), and gauge independent (unlike $\boldsymbol{\mathcal{A}}(\delta)$). The latter will become more obvious in section 1.3.2.

In most cases, two- or three-dimensional parameter spaces $\mathbb{P}$ suffice. The case of a 3D system was considered in the original paper by Berry [15]. The Berry curvature $\mathcal{F}$ can then be interpreted as a vector, just like the magnetic field in real space,

$$\mathcal{F}_k := \sum_{i,j} \epsilon_{kij}\mathcal{F}_{ij} = (\nabla \times \boldsymbol{\mathcal{A}})_k\,. \tag{1.22}$$

In section 2.2.3, we will only compute the Berry curvature in a 2D parameter space, which has only a single independent entry. However, we will extend the parameter space in section 3.3.3, which could also be described by a tensorial curvature.

1.3.2 Poles & degeneracies

Working in a higher dimensional space, we can now close the (orientable) surface $\mathcal{S} = \partial\mathcal{V}$ and apply Stokes' theorem a second time to arrive at an integration over the enclosed volume $\mathcal{V}$. Defining $\partial_i := \frac{\partial}{\partial\delta_i}$, we find

$$\oint_{\mathcal{S}} \sum_{ij} \partial_j \mathcal{A}_i(\boldsymbol{\delta})\,\mathrm{d}\delta_j \wedge \mathrm{d}\delta_i = \int_{\mathcal{V}} \sum_{ijk} \partial_k\partial_j \mathcal{A}_i(\boldsymbol{\delta})\,\mathrm{d}\delta_k \wedge \mathrm{d}\delta_j \wedge \mathrm{d}\delta_i\,. \tag{1.23}$$

This integral does not directly relate to $\gamma(\mathcal{C})$, anymore, but it is easy to compute: If $\partial_k\partial_j\mathcal{A}_i$ exists everywhere in $\mathcal{V}$, the derivatives commute, while the wedge product anticommutes. The integral therefore needs to vanish—which is simply a generalization of the three-dimensional statement $\operatorname{div}\operatorname{rot}\boldsymbol{\mathcal{A}} = 0$.

However, there can be poles of the Berry curvature $\mathcal{F}$, defined in eq. (1.21). Once again, we use a countable eigenbasis $\{|\psi_n(\boldsymbol{\delta})\rangle\,,\ n \in \mathbb{N}_0\}$ for each Hamiltonian $\hat{H}(\boldsymbol{\delta})$. The Berry curvature of the ground state $|\psi_0\rangle$ can then be written as

$$\mathcal{F}_{ij} = \partial_i \mathcal{A}_j - \partial_j \mathcal{A}_i = 2\Im \langle \partial_j \psi_0 \,|\, \partial_i \psi_0 \rangle = 2 \sum_{n>0} \Im \left[\langle \partial_j \psi_0 \,|\, \psi_n \rangle \langle \psi_n \,|\, \partial_i \psi_0 \rangle \right] . \tag{1.24}$$

We left out $n = 0$ when inserting the identity, because from $|\psi_n\rangle$ being normalized it follows that

$$i \langle \psi_n \,|\, \partial_i \psi_n \rangle \in \mathbb{R} \,, \tag{1.25}$$

such that this term does not contribute to the sum in eq. (1.24). The terms $\langle \psi_n \,|\, \partial_i \psi_0 \rangle$ depend on gauge choice, and require the derivative to be well defined. We can reformulate the expression by acting on the instantaneous basis with a partial derivative,

$$\left(\partial_i \hat{H}\right) |\psi_n\rangle + \hat{H} \,|\partial_i \psi_n\rangle = (\partial_i E_n)\, |\psi_n\rangle + E_n \,|\partial_i \psi_n\rangle \ , \tag{1.26}$$

and take the overlap with a second eigenstate $m \neq n$,

$$\left\langle \psi_m \middle| \partial_i \hat{H} \middle| \psi_n \right\rangle + E_m \langle \psi_m \,|\, \partial_i \psi_n \rangle = E_n \langle \psi_m \,|\, \partial_i \psi_n \rangle \ . \tag{1.27}$$

This yields an explicitly gauge-independent expression of the Berry curvature, which exhibits poles for parameters $\boldsymbol{\delta}$ where the ground state $|\psi_0\rangle$ becomes degenerate,

$$\mathcal{F}_{ij} = 2 \sum_{n>0} \Im \langle \partial_j \psi_0 \,|\, \psi_n \rangle \langle \psi_n \,|\, \partial_i \psi_0 \rangle = 2 \sum_{n>0} \Im \frac{\left\langle \psi_0 \middle| \partial_j \hat{H} \middle| \psi_n \right\rangle \left\langle \psi_n \middle| \partial_i \hat{H} \middle| \psi_0 \right\rangle}{(E_n - E_0)^2} \,. \tag{1.28}$$

The integrated Berry curvature over a closed, orientable surface $\mathcal{S}$ can therefore be written as

$$\frac{1}{2} \oint_{\mathcal{S}} \sum_{ij} \mathcal{F}_{ij}(\boldsymbol{\delta})\, \mathrm{d}\delta_j \wedge \mathrm{d}\delta_i = 2\pi C \,, \quad C \in \mathbb{Z} \,. \tag{1.29}$$

where the *Chern number* C is given by the enclosed degeneracies.

1.4 TKNN equation

We have introduced the Berry curvature $\mathcal{F}$ in eq. (1.28), and shown that integrating it over a closed, orientable surface in parameter space yields integer quantized values. Here, we will derive a very similar formula for two-dimensional lattice models. This derivation was published by Thouless, Kohmoto, Nightingale, and den Nijs [10], and their result is therefore known as TKNN equation. They take a more "physical" approach, starting from linear-response theory, and find that the integral of the Berry curvature actually relate to physical observables.

1.4.1 Linear Response

Quantized Hall conductivity can be probed by applying weak external fields. Therefore, we want to compute low orders of the system's response to a perturbation—in particular the *linear response*. We follow the original derivation of the Kubo formula [89], but similar steps can be found in most books on many-body physics [90, 91], or lecture notes, for example by Giamarchi et al. [92].

We consider a non-perturbed system which is described by a constant Hamiltonian $\hat{H}_0$. Initially, the system is in a steady state, described by a density matrix $\hat{\rho}$. At time $\tau = 0$ a weak, time-dependent perturbation $\hat{H}_p$ is turned added. Thus, the state $\hat{\rho}'$ of the perturbed system becomes time-dependent,

$$\hat{H}(t) = \hat{H}_0 + \hat{H}_p(\tau)\,, \qquad \frac{\mathrm{d}\hat{\rho}(t)}{\mathrm{d}\tau} = \frac{i}{\hbar}\left[\hat{H}(\tau), \hat{\rho}(\tau)\right]\,. \tag{1.30}$$

We assume that the physical state will only be slightly perturbed. Thus, we express the density matrix $\hat{\rho}$ by the unperturbed state $\hat{\rho}_0$ and a small, time-dependent perturbation $\hat{\rho}_p(\tau)$,

$$\hat{\rho}(\tau) = \hat{\rho}_0 + \hat{\rho}_p(\tau)\,. \tag{1.31}$$

We can split the equation of motion and ignore quadratically small terms,

$$\frac{\mathrm{d}\hat{\rho}_p(\tau)}{\mathrm{d}t} \approx \frac{i}{\hbar}\left[\hat{H}_0, \hat{\rho}_p(\tau)\right] + \frac{i}{\hbar}\left[\hat{H}_p(\tau), \hat{\rho}_0\right]\,. \tag{1.32}$$

The first commutator corresponds to the 'natural motion' due to the unperturbed Hamiltonian $\hat{H}_0$. We get rid of it by switching to the *interaction picture*, which is the Heisenberg picture with respect to the time-independent Hamiltonian $\hat{H}_0$. We transform the density matrix as,

$$\hat{\rho}_p^{\mathrm{I}}(\tau) := \mathrm{e}^{-i\hat{H}_0\tau/\hbar}\,\hat{\rho}_p(\tau)\,\mathrm{e}^{i\hat{H}_0\tau/\hbar}\,. \tag{1.33}$$

The first term of the equation of motion, eq. (1.32), thus vanishes,

$$\frac{\mathrm{d}\rho_p^{\mathrm{I}}}{\mathrm{d}\tau} = \frac{1}{i\hbar}\left[\hat{H}_0, \rho_p^{\mathrm{I}}(\tau)\right] + \mathrm{e}^{-i\hat{H}_0\tau/\hbar}\,\frac{\mathrm{d}\rho_p}{\mathrm{d}\tau}\,\mathrm{e}^{i\hat{H}_0\tau/\hbar} = \frac{i}{\hbar}\left[\hat{H}_p^{\mathrm{I}}, \rho_0\right]\,, \tag{1.34}$$

and we can formally integrate the equation,

$$\hat{\rho}_p^{\mathrm{I}}(\tau) = \frac{i}{\hbar}\int_0^\tau \mathrm{d}\tau'\left[\hat{H}_p^{\mathrm{I}}(\tau'), \hat{\rho}_0\right]\,. \tag{1.35}$$

Thus, we compute how the expectation value of an observable $\hat{O}$ changes due to the perturbation of the density matrix,

$$\begin{aligned}\left\langle \hat{O} \right\rangle(\tau) &= \frac{i}{\hbar}\,\mathrm{tr}\left(\hat{O}^{\mathrm{I}}(\tau)\int_0^t \mathrm{d}\tau'\left[\hat{H}_p^{\mathrm{I}}(\tau'), \hat{\rho}_0\right]\right) \\ &= \frac{i}{\hbar}\,\mathrm{tr}\left(\int_0^\tau \mathrm{d}\tau'\hat{\rho}_0\left[\hat{O}^{\mathrm{I}}(\tau), \hat{H}_p^{\mathrm{I}}(\tau')\right]\right)\,.\end{aligned} \tag{1.36}$$

In order to arrive at the Kubo formula for the response to a weak external field $h(\tau)$, we consider linear coupling to an operator $\hat{P}^{\mathrm{I}}(\tau)$,

$$\hat{H}_p^{\mathrm{I}}(\tau) = h(\tau)\hat{P}^{\mathrm{I}}(\tau)\,. \tag{1.37}$$

Thus, we define the susceptibility χ,

$$\chi(\tau,\tau') = \frac{i}{\hbar}\Theta(\tau-\tau')\left\langle\left[\hat{O}^{\mathrm{I}}(\tau)\,,\hat{P}^{\mathrm{I}}(\tau')\right]\right\rangle_0\,, \tag{1.38}$$

such that the linear response of an operator $\hat{O}$ to a weak applied field $h(\tau)$ can be expressed as

$$\left\langle\hat{O}\right\rangle(\tau) = \int \mathrm{d}\tau'\,\chi(\tau,\tau')h(\tau')\,. \tag{1.39}$$

Note that the time dependence in equation eq. (1.38) is merely the time evolution due to $\hat{H}_0$. Therefore, we use its eigenbasis $\hat{H}_0\left|n\right\rangle = E_n\left|n\right\rangle$ to simplify the expression for the susceptibility—this is usually called frequency representation, or Lehmann representation,

$$\chi(\tau,\tau') = \frac{i\Theta(\tau-\tau')}{\hbar Z}\sum_{n,m}\left(\mathrm{e}^{-\beta E_n}-\mathrm{e}^{-\beta E_m}\right)\mathrm{e}^{i(E_m-E_n)(\tau-\tau')/\hbar}\left\langle n\middle|\hat{O}\middle|m\right\rangle\left\langle m\middle|\hat{P}\middle|n\right\rangle\,, \tag{1.40}$$

where we expanded the commutator. We find that the susceptibility only depends on time differences. Even though we will only be interested in constant fields in the end, it turns out to be easier to express the calculations in frequency space. We perform the Fourier transformation in the upper half-plane,

$$\begin{aligned}\chi(\omega) &= \int \mathrm{d}\tau\,\mathrm{e}^{i[\omega+i0^+]\tau}\,\chi(0,\tau)\\ &= \frac{1}{\hbar Z}\sum_{m,n}\frac{\mathrm{e}^{-\beta E_n}-\mathrm{e}^{-\beta E_m}}{\omega+(E_m-E_n)/\hbar}\left\langle n\middle|\hat{O}\middle|m\right\rangle\left\langle m\middle|\hat{P}\middle|n\right\rangle\,.\end{aligned} \tag{1.41}$$

The response in eq. (1.39) simplifies, and becomes a product in frequency space,

$$\left\langle\hat{O}\right\rangle(\omega) = \chi(\omega)h(\omega)\,. \tag{1.42}$$

1.4.2 Quantized Hall response

To arrive at the TKNN equation, we just have to plug in the operators relevant to Hall conductivity. As we did in section 1.2, we have to apply an external electric field to observe a Hall current. Thus, we add a time-dependent vector potential via minimal coupling,

$$\hat{\boldsymbol{p}} \to \hat{\boldsymbol{p}} - q\boldsymbol{A}(\tau)\,. \tag{1.43}$$

Here, the potential $\boldsymbol{A}$ is in addition to the vector potential which may, or may not [93], already be included in the unperturbed Hamiltonian $\hat{H}_0$. The linearized perturbation now couples to the current operator $\hat{\boldsymbol{j}}$,

$$\hat{H}_p = \boldsymbol{A}(\tau)\cdot\hat{\boldsymbol{j}}\,. \tag{1.44}$$

The conductivity tensor σ is thus given by the linear current-current response, i.e., we find in frequency space,

$$\left\langle \hat{\boldsymbol{j}} \right\rangle(\omega) = \sigma(\omega)\boldsymbol{\epsilon}(\omega)\,, \qquad \text{where} \qquad \boldsymbol{\epsilon}(\omega) = i\omega \boldsymbol{A}(\omega)\,. \tag{1.45}$$

Eventually, we are interested in the off-diagonal entries of σ, and want to find the response to a constant electric field, i.e., $\omega \to 0$. Plugging the current operators into the Kubo formula, eq. (1.41), and taking the low frequency limit, we find

$$\begin{aligned}\sigma(\omega) &= \frac{1}{i\hbar\omega Z}\sum_{m,n}\frac{\mathrm{e}^{-\beta E_n} - \mathrm{e}^{-\beta E_m}}{\omega + (E_m - E_n)/\hbar}\left\langle n\middle|\hat{j}_x\middle|m\right\rangle\left\langle m\middle|\hat{j}_y\middle|n\right\rangle \\ &\overset{\omega\ll 1}{\approx} \frac{1}{i\hbar Z}\sum_{n,m}\left[\frac{\mathrm{e}^{-\beta E_n} - \mathrm{e}^{-\beta E_m}}{\omega(E_m - E_n)/\hbar} + \frac{\mathrm{e}^{-\beta E_n} - \mathrm{e}^{-\beta E_m}}{(E_m - E_n)^2/\hbar^2}\right]\left\langle n\middle|\hat{j}_x\middle|m\right\rangle\left\langle m\middle|\hat{j}_y\middle|n\right\rangle\,.\end{aligned} \tag{1.46}$$

The first summand in the brackets $\propto \omega^{-1}$ is symmetric under exchange of $m \leftrightarrow n$, such that its contribution to σ is purely imaginary. We can therefore ignore it, even though it seems to diverge for $\omega \to 0$.[1]

Finally, we introduce a lattice, and take the low-temperature limit, i.e., only consider the ground state. Assuming the Fermi energy E_F lies in a band gap, we can express it by a sum over occupied bands ν, and integrate over the Brillouin zone,

$$\sigma_{xy} = \frac{1}{\hbar}\sum_{\nu}\oint_{\mathrm{BZ}}\mathrm{d}k_x\,\mathrm{d}k_y\sum_{\substack{m\\E_m>E_F}}\Im\frac{\left\langle \boldsymbol{k},\nu\middle|\hat{j}_x\middle|m\right\rangle\left\langle m\middle|\hat{j}_y\middle|\boldsymbol{k},\nu\right\rangle}{(E_F - E_m)^2/\hbar^2}\,. \tag{1.47}$$

Since $\hat{\boldsymbol{j}}$ is a single-particle observable, we need only sum over single-particle states $|m\rangle$. Furthermore, we can restrict the sum over m to states above the Fermi energy, since other terms would cancel. TKNN [10] realized that the velocity operator for Bloch electrons can be expressed by derivatives of the unperturbed Hamiltonian,

$$\hat{\boldsymbol{j}} = \frac{e}{\hbar}\left(\nabla_{\boldsymbol{k}}\hat{H}_0\right)\,. \tag{1.48}$$

Therefore, we can directly use our results from eqs. (1.28) and (1.29) to evaluate eq. (1.47), and find the TKNN formula,

$$\begin{aligned}\sigma_{xy} &= \frac{e^2}{2\pi h}\sum_{\nu}\oint_{\mathrm{BZ}}\mathrm{d}k_x\,\mathrm{d}k_y\sum_{E_m>E_F}\Im\frac{\left\langle \boldsymbol{k},\nu\middle|\partial_{k_x}\hat{H}_0\middle|m\right\rangle\left\langle m\middle|\partial_{k_y}\hat{H}_0\middle|\boldsymbol{k},\nu\right\rangle}{(E_F - E_m)^2} \\ &= \frac{e^2}{h}\sum_{\nu}C_\nu\,.\end{aligned} \tag{1.49}$$

Unsurprisingly, the result looks a lot like the Hall conductivity measured by Klitzing et al. [4], see eq. (1.4). Except that the Chern number can also be a negative integer. Though, it is surprising that this calculation is actually really precise: Even for very weak perturbations, linear response is not typically accurate to 10^{-9}.

[1] For quantum Hall systems, the term proportional to ω^{-1} actually vanishes due to gauge invariance, cf. ref. [75].

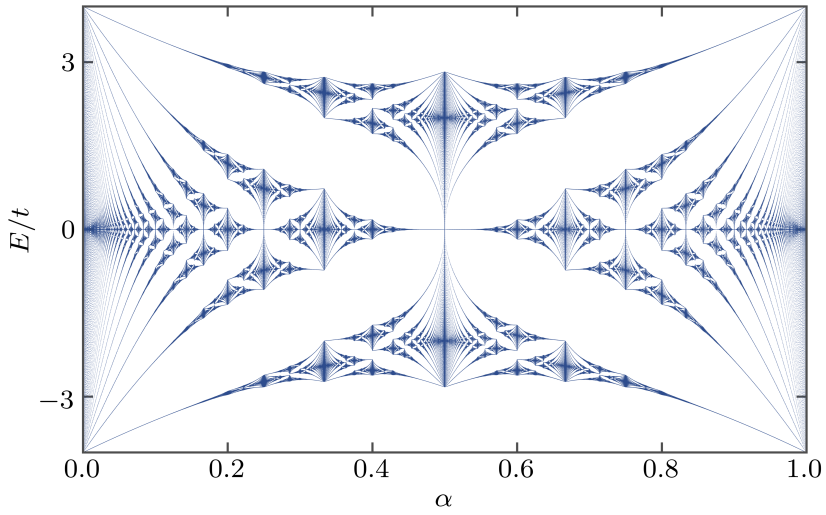

Figure 1.3: *The fractal Hofstadter-butterfly band structure.* For magnetic flux $\alpha = p/q$ per lattice plaquette, there are q energy bands, albeit the two center bands touch for even denominators q. We increased the size of energy bands for large q for visualization purposes.

1.5 The Hofstadter model

The TKNN formula motivates the notion of a topological band structure, and relates it to quantized physical observables. Now, we also need a model Hamiltonian which possesses bands with nontrivial Chern numbers.

Throughout this thesis, we will be studying variants of the Harper-Hofstadter Hamiltonian [11, 94], which was already used in the derivation by Thouless et al. [10]. Using annihilation (creation) operators $\hat{c}^{(\dagger)}$ of spin-1/2 fermions on a square lattice of width W and length L, it can be expressed as,

$$\hat{H}_H = \sum_{x=1}^{L} \sum_{y=1}^{W} \sum_{\sigma=\downarrow,\uparrow} \left(-t_y \, \mathrm{e}^{2i\pi\alpha x} \, \hat{c}^\dagger_{x,y,\sigma} \hat{c}_{x,y+1,\sigma} - t \hat{c}^\dagger_{x,y,\sigma} \hat{c}_{x+1,y,\sigma} \right) + \mathrm{H.c.} \tag{1.50}$$

Particles tunnel between adjacent lattice sites in x (y) direction at rate $t_{(y)}$. Analog to the Landau gauge chosen for the magnetic field in section 1.2, there is an x-dependent complex phase as particles hop along the y direction. As a particle moves around a lattice plaquette, it gains a phase $\mathrm{e}^{2i\pi\alpha}$, corresponding to α flux quanta per plaquette.

By this definition, the two spin species are uncoupled, and observe the same flux piercing. Thus, the model breaks time-reversal symmetry, which is required to find nonzero Chern numbers. On can also define, and realize [12], a time-reversal symmetric variant of the Hofstadter model by making the sign of α spin dependent. The model may then realize the quantum spin-Hall effect, described by a $\mathbb{Z}_2$ topological invariant.

The Hofstadter model is not actually a good description for condensed-matter systems: As noted by Hofstadter [11], extremely strong magnetic fields would be required to realize $\alpha = \mathcal{O}(1)$ magnetic flux-density per plaquette in a typical crystal. Yet, he was

fascinated by the fractal spectrum of the Hamiltonian: The band structure of the Hofstadter model strongly depends on the parameter α. Assuming a rational flux density $\alpha = p/q$, and periodic boundaries along the width, $\hat{c}^{(\dagger)}_{x,W+1,\sigma} \equiv \hat{c}^{(\dagger)}_{x,1,\sigma}$, we can perform a Fourier transformation along the y axis,

$$\hat{H}_H = \sum_{x=1}^{L} \sum_{k_y=1}^{W} \sum_{\sigma=\downarrow,\uparrow} \left[-t_y \cos\left(2\pi(\alpha x + k_y/W)\right) \hat{n}_{x,k_y,\sigma} - t\hat{c}^{\dagger}_{x,k_y,\sigma}\hat{c}_{x+1,k_y,\sigma} \right] + \text{H.c.} \quad (1.51)$$

Here, the cosinusoidal dispersion relation inherits the spatial dependence of the gauge field in eq. (1.50). As a result, the magnetic unit cell is q sites long, which reduces the number of allowed momenta k_x, and generally creates q energy bands. We show the resulting "butterfly" spectrum in fig. 1.3. As noted already in the original work by Hofstadter [11], the case of irrational flux α is particularly interesting from a theoretical point of view. We will briefly touch on this case in the context of section 1.5.2.

1.5.1 Topological band structure

Most bands ν of the Hofstadter model exhibit nontrivial Chern numbers $C_\nu \neq 0$, which are defined by identifying $\boldsymbol{\delta}$ in eq. (1.29) with quasimomenta $\{k_x, k_y\}_{\mathbb{T}^2}$, as we did for the TKNN formula in eq. (1.49). We do not have to diagonalize eq. (1.51), and compute the Berry curvature explicitly, because the Chern numbers are solutions to a simple diophantine equation [10, 95, 96],

$$r = s_r q + C_r p\,, \quad \text{where} \quad s_r, C_r \in \mathbb{Z} \ \wedge\ |C_r| \leq q/2\,. \quad (1.52)$$

When the Fermi energy lies in the rth band gap, the total Chern number of all occupied bands is given by $C_r = \sum_{\nu=1}^{r} C_\nu$. Conversely, the Chern number of the νth band is given by the difference of the Chern numbers of the adjacent gaps, $C_\nu = C_{r=\nu} - C_{r=\nu-1}$.

The band structure for $\alpha = 1/3$, which we consider in this thesis, is shown in fig. 1.4. For this case, we will label the lower, middle, and upper band by $\nu = l, m, u$ to avoid confusion with the indices for the gaps. In this case, eq. (1.52) gives $C_1 = 1,\ s_1 = 0$ and $C_2 = -1,\ s_2 = 1$, such that we have Chern numbers $C_l = 1$, $C_m = -2$ and $C_u = 1$.

Due to particle-hole symmetry, we can relate the topological index of the rth gap to the $(r' := q - r)$th gap via $s_{r'} = 1 - s_r$ and $C_{r'} = -C_r$. From this, we can follow that for even denominators, $q \in 2\mathbb{Z}$, the Chern number of the central gap needs to vanish, $C_{q/2} = 0$ However, this is no solution to eq. (1.52)! The contradiction is resolved by the fact, that the $q/2$th band gap does not exist: For all even values of q, the center bands touch, and the Chern number is ill defined.

1.5.2 Charge pumps

In the previous section 1.3, and 1.4, we have used that, for a free model, quasimomentum is formally the same thing as any other parameter δ of the Hamiltonian. By this analogy, we can reinterpret the mixed real- and momentum-space representation of the Hofstadter Hamiltonian in eq. (1.51) as a family of 1D systems,

$$\hat{H}_H(\delta) = \sum_{x=1}^{L} \sum_{\sigma} \left[-\frac{V}{2} \cos\left(2\pi\alpha x + \delta\right) \hat{n}_{x,\sigma} - t\hat{c}^{\dagger}_{x,\sigma}\hat{c}_{x+1,\sigma} \right] + \text{H.c.} \quad (1.53)$$

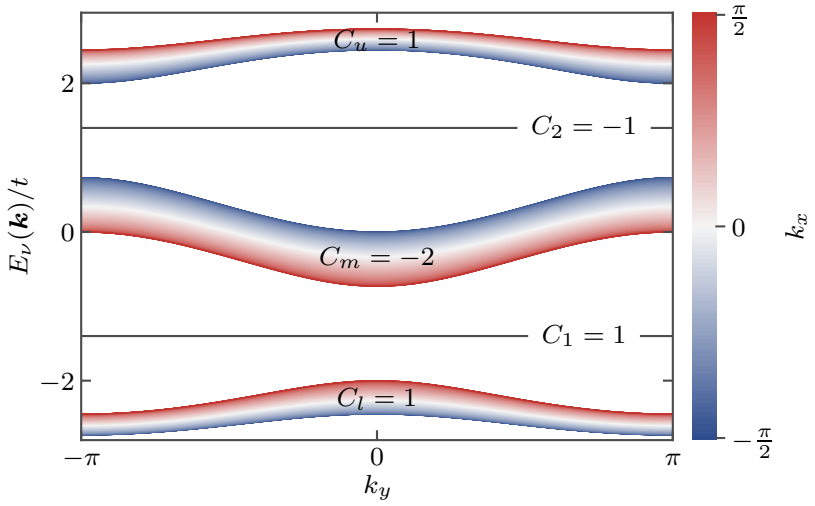

Figure 1.4: *Energy bands of the Hofstadter model for flux $\alpha = 1/3$.* We show Chern numbers of the gaps, $C_{1,2}$ according to eq. (1.52), and define the Chern numbers of lower, middle, and upper band $C_{l,m,u}$ as the difference of the respective gaps.

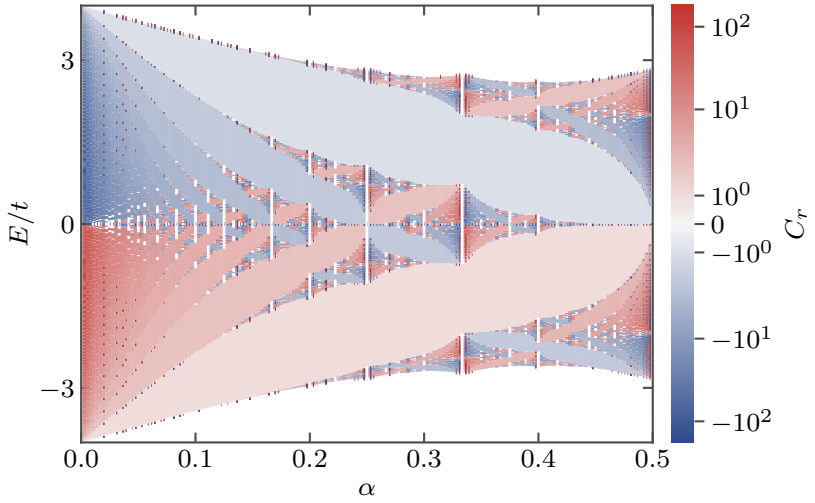

Figure 1.5: *Chern numbers in the Hofstadter butterfly.* The color of each rth band gap in fig. 1.3 is given by its Chern number C_r, as defined in eq. (1.52). The Chern numbers are bounded by $|C_r| \leq q/2$, and diverge in a continuum limit—the corresponding gaps also become arbitrarily small, such that the limit $q \to \infty$ is not physically relevant. The color scale is logarithmic for $|C_r| > 2$ in order to make $C_r = 1$ and $C_r = -1$ distinguishable.

Obviously, renaming variables does not affect topological properties. However, their physical interpretation changes: In such cases of a periodic potential, shifted by a parameter δ, Thouless [55] discovered that the number of particles transported through the lattice in each adiabatic cycle $\delta \to \delta + 2\pi$ is integer quantized in the infinite-size limit. Therefore, such models are commonly referred to as *Thouless pumps* or topological charge (as opposed to: spin) pumps.

We will only motivate the relation of pumped particles and topological invariants, a more pedagogic derivation can be found in the book by Asbóth et al. [97]. We assume adiabatic pumping, i.e., that the time-dependent state $|\psi(\tau, k)\rangle$ is close to the instantaneous ground state, $|\langle\psi(\tau, k)\,|\,\psi_0(\delta(\tau), k)\rangle| \approx 1$. The ansatz wave function, as used by Thouless [55], needs to take excited states into account,

$$|\psi(\tau,k)\rangle = \exp\left[\frac{-i}{\hbar}\int_0^\tau \mathrm{d}\tau' E_0(\delta(\tau'),k)\,\mathrm{d}\tau'\right] \times\left[|\psi_0(\delta,k)\rangle + i\hbar\sum_{n>0}|\psi_j(\delta,k)\rangle\,\frac{\langle\psi_n(\delta,k)\,|\,\partial_\delta\psi_0(\delta,k)\rangle}{E_n - E_0}\frac{\mathrm{d}\delta}{\mathrm{d}\tau}\right]. \tag{1.54}$$

We can reuse the expression for the velocity (particle current) operator in terms of $\partial_k \hat{H}$, we have already seen in section 1.4, and express it using the spectral decomposition of $\hat{H}$,

$$\hat{v} = \frac{1}{\hbar}\partial_k \hat{H} = \frac{1}{\hbar}\sum_n \left([\partial_k E_n]\,|\psi_n\rangle\langle\psi_n| + E_n\,|\partial_k\psi_n\rangle\langle\psi_n| + E_n\,|\psi_n\rangle\langle\partial_k\psi_n|\right). \tag{1.55}$$

The number of pumped particles Δ_N is then given by expectation value of the velocity operator, integrated over one pump cycle, and over all momenta k,

$$\Delta_N = \int \mathrm{d}\tau \oint_{\mathrm{BZ}} \frac{\mathrm{d}k}{2\pi}\,\langle\psi(\tau,k)\,|\,\hat{v}\,|\,\psi(\tau,k)\rangle\,. \tag{1.56}$$

We are only interested in the case of fully occupied bands. This simplifies the overlap in eq. (1.56), since

$$\oint_{\mathrm{BZ}} \mathrm{d}k\,\partial_k E_n = 0\,, \tag{1.57}$$

and we are left with an integer quantized result,

$$\Delta_N = \oint \mathrm{d}\delta \oint \frac{\mathrm{d}k}{2\pi}\sum_{n>0} i\,\langle\partial_k\psi_0(\delta,k)\,|\,\psi_n(\delta,k)\rangle\,\langle\psi_n(\delta,k)\,|\,\partial_\delta\psi_0(\delta,k)\rangle + \mathrm{H.c.} = C\,. \tag{1.58}$$

This derivation requires a system which is both infinite and periodic [55]. However, the deviations from integer values found in finite models are typically well behaved [98, 99], and $1/L$ extrapolation may be used to improve the results. We show finite-size corrections for the free model, discussed in this section, in fig. 1.6. Variants of topological pumps have been realized both in ultracold-atomic systems [58, 59, 62, 100] and using photonics [101, 102].

The 1D model given in eq. (1.53) is also interesting for irrational flux densities α. It is then known as the Audry-André model [103], and of theoretical interest for its transition to an Anderson-localized state with potential strength V [104–109]. It has been realized using ultracold atoms [110, 111] and photonic systems [101].

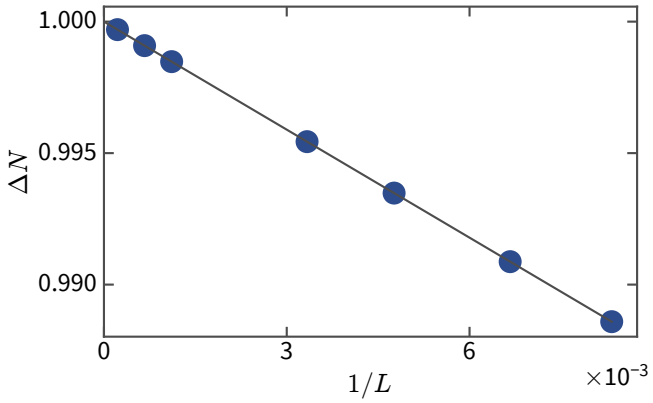

Figure 1.6: *Finite-size deviation from the quantized result of the Thouless pump.* Data are shown for the free model given in eq. (1.53) and system sizes $L \in \{120, 150, 210, 300, 900, 1500, 4500\}$. For a single spin species, we reproduce the integer quantized Chern number of the lowest band $C_l = 1$ upon polynomial finite-size extrapolation in $1/L$. Data are computed in an open system, corresponding to some models studied in section 3.3. In this setting, finite-size effects are due to the finite extent of edge states.

1.6 Discussion

We have now introduced the basic physical concepts required for our numerical analysis in the following chapters. We want to briefly recapitulate some results, and put them into context.

Integer-quantized Hall conductivity can be understood in terms of basic quantum mechanics, which yields Landau levels, or in terms of a topological band structure in lattice models. For strong magnetic fields, the latter exhibits richer physics, as the quantized Hall conductivity can be of either sign. We do not really care about the absolute sign of the Hall conductivity—we actually use opposite conventions in chapter 3 and chapter 4, corresponding to ref. [1] and ref. [2]. However, in section 3.3.2 and section 4.2 we will study topological transitions, where the sign of the Chern number changes with interaction strength.

Introducing topology, we can understand that integer-quantization is protected by the energy gap. This strong statement comes at a cost: We have to consider boundary conditions. Following the TKNN derivation in section 1.4, we have swept them under the rug: By integrating over quasimomenta $k_{x,y}$, we have implicitly assumed an infinite, toric system.

While it is instructive to define topology of band structures on the $\{k_x, k_y\}$ space, this can only work when the quasimomenta are good quantum numbers. In order to define topological invariants in interacting systems, we will have to introduce twisted boundary conditions [112, 113], as we used in section 1.3. Instead of going the instructive way via linear response as in section 1.4, the analogy of twist angle δ and quasimomentum

k_y can also be read off from the Fourier-space Hamiltonian. Choosing a spatially homogeneous implementation of the twist angle,

$$\hat{H}(\delta) = \sum_x t_y \, \mathrm{e}^{i\delta/W} \, \hat{c}_y^\dagger \hat{c}_{y+1} + \mathrm{H.c.} \quad \rightarrow \quad \hat{H}(\delta, k_y) = \sum_{k_y} 2t_y \cos\left(k_y + \delta/W\right) \hat{n}_{k_y} \,, \tag{1.59}$$

we find that k_y and δ enter the free Hamiltonian in the same way. Therefore, one should consider the Berry curvature definition on a family of Hamiltonians to be the more general one, and topological band structure to be the special case for free models.

Considering a family of Hamiltonians on some parameter space might seem unsatisfying, and variable twist angles may not be realizable in some experimental setups. Indeed, for typical Hamiltonians, the dependence of bulk properties on twist angles is exponentially suppressed in linear system size [114]. In particular, this means that the Berry curvature becomes constant in the parameter space of twist angles [115, 116], for sufficiently large systems.

Lastly, a comment on the dimensionality of parameter spaces. In his original paper, Berry [15] studied a three-dimensional parameter space, which is required to create degeneracies in generic Hamiltonians. By only considering two quasimomenta, we find the Hofstadter model to be gapped throughout, but still topologically nontrivial. By the parameterization of eq. (1.50), we have wrapped the Brillouin zone around the degenerate points. For the one-dimensional model in eq. (1.53), representing a charge pump, it is easy to see how to recover the degeneracies: By sending the superlattice potential strength V, or, equivalently, the anisotropy t_y/t in eq. (1.51) to zero, we recover a 1D tight-binding model, and all gaps vanish.

2 Methods & observables

This section will outline the numerical methods, and define the observables used in this thesis. Most results were obtained using the density-matrix renormalization-group algorithm (DMRG) [117–119] for ground-state search. We will sketch this method in section 2.1, and note some aspects which are particular to our simulations. The following section 2.2 will introduce the observables which we study in the rest of this thesis. Section 2.3 will discuss some of our methods to improve and verify DMRG accuracy.

2.1 DMRG 101

The DMRG algorithm was invented by Steven R. White [117] in 1992, and is, in general, the methods of choice to numerically solve 1D models. Implementing the DMRG algorithm was not part of this work, instead we used the SyTen toolkit [120]. This section will therefore be brief: We will introduce some definitions used in the following chapters, and point out the algorithm's capabilities and limitations. For the more interested reader, we recommend the review by Ulrich Schollwöck [119], and also the thesis of Claudius Hubig [121], who implemented most of our DMRG toolkit.

2.1.1 Matrix-product states

We consider a lattice of length L, where each site i has d degrees of freedom, i.e., there exists a local basis $\{\hat{c}^\dagger_{\sigma_i} |0\rangle\}$ with a countable set of labels $|\{\sigma_i\}| = d$ for spin, particle number, etc. Any state can then be written as,

$$|\psi\rangle = \sum_{\sigma_1} \cdots \sum_{\sigma_L} c_{\sigma_1,\ldots,\sigma_L} \prod_{i=1}^{L} \hat{c}^\dagger_{\sigma_i} |0\rangle \ , \quad c_{\sigma_1,\ldots,\sigma_L} \in \mathbb{C} \, . \tag{2.1}$$

Thanks to second quantization, this expression looks harmless. But, the indices give it away, the coefficient tensor c is a huge object with $\mathcal{O}(d^L)$ entries. While there are constraints on c, normalization, symmetries, etc., a generic states for $L = \mathcal{O}(100)$ can never be represented on a classical computer.

The simplest way to make the coefficient tensor c manageable is by approximating it with a product of coefficients,

$$c_{\sigma_1,\ldots,\sigma_L} \xrightarrow{\text{product state}} \prod_{i=1}^{L} c_{\sigma_i} \, , \quad c_{\sigma_i} \in \mathbb{C} \, . \tag{2.2}$$

Such product state is defined by $\mathcal{O}(dL)$ coefficients, however it does not allow any correlations between sites $i \neq j$, rendering it useless for many-body physics.

Matrix-product states are—as the name suggests—also product states, but use matrices rather than scalar variables,

$$c_{\sigma_1,\ldots,\sigma_L} \xrightarrow{\text{MPS}} \prod_{i=1}^{L} (M_i)_{\sigma_i} \ , \quad (M_i)_{\sigma_i} \in \mathcal{M}\left(m_{i-1} \times m_i, \mathbb{C}\right) \ , \tag{2.3}$$

where we have introduced the bond-dimensions m_i. A priori, it is not clear that this approximation is useful. However, we reduced the number of parameters to $\mathcal{O}(m^2 dL)$, assuming $m_i \approx m$ constant, and we recover the product state for $m = 1$.

Graphical representation

Equation (2.3) looks deceivingly simple, because we let matrix multiplication take care of all contracted indices. Here, we introduce a graphical representation which retains readability while making tensor contractions explicit.

Treating the local basis of dimension d on the same footing as the correlation bonds of dimension m, A is a tensor of rank 3. We will thus represent it by a circle with three "legs", as shown in fig. 2.1 (a). Suitable tensor legs can be connected, which represents a contraction of the corresponding dimension. The coefficient tensor c is a contraction over all MPS bonds, as shown in fig. 2.1 (b).

Importantly, the contraction fig. 2.1 (b) can also be performed in reverse: *Any* finite coefficient tensor c can be decomposed into an MPS by means of repeated singular value (SVD) or QR decomposition, cf. ref. [119]. This statement means that MPS are dense in the full Hilbert space. However, it is rather of theoretical interest, since the required bond dimensions m will be exponential in system size L.

2.1.2 Ground-state search

Having introduced MPS, DMRG can be understood as a variational optimization of the state's energy [122, 123], one site at a time [119, 124]. Here, we will sketch this method, and comment on the DMRG3S algorithm [125], which we use throughout this thesis.

The optimization of the MPS tensors can be performed efficiently, because the Hamiltonian can also be decomposed into a series of local low-rank tensors. Since a Hamiltonian $\hat{H}$ connects two states, the tensors representing the corresponding matrix-product operator (MPO) needs to have two physical legs. As shown in fig. 2.1 (c), such tensors of rank $r \geq 4$ can be decomposed into $r - 2$ rank-three tensors. Generating MPOs for arbitrary Hamiltonians efficiently is not trivial, we refer the reader to ref. [126] for more details on our methods. We denote the bond-dimensions of the MPO by w_i.

Once we have the MPO tensors and a suitable matrix-product state, expectation values can be computed via a contraction of the tensor network as shown in fig. 2.1 (d). Note that the order in which tensor legs are contracted greatly affects numerical cost.

The single-site DMRG method then optimizes the total energy by solving the eigenvalue equation shown in fig. 2.2 for one site i at a time. The optimization is performed during a right (left) *sweep* over the MPS: The optimized tensor M_i' is then contracted with W_i and L_{i-1} (R_{i+1}) yielding L_i (R_i). The procedure is then repeated for site $i + 1$ ($i - 1$), where the tensor R_{i+1} (L_{i-2}) had been stored in the previous sweep.

This primitive version of a single-site DMRG algorithm unfortunately tends to get stuck. To find the true ground state, one either increases the unit cell and optimizes two sites at once, or adds perturbations to the optimized single-site tensors. We choose the latter,

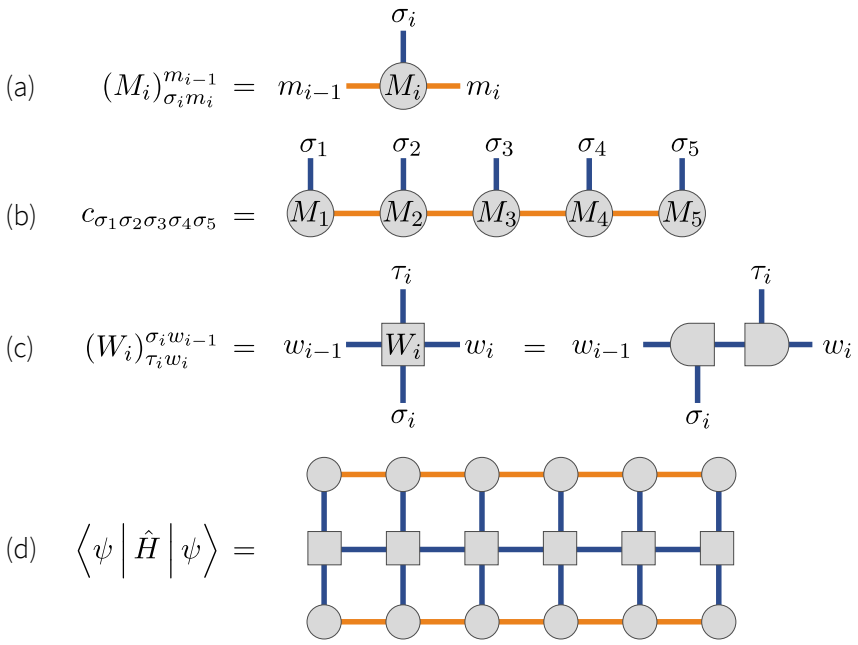

Figure 2.1: *Graphical representation of MPS and MPO tensors.* (a) depicts an MPS tensor with three legs, as it is of rank three. In order to match our color scheme of section 2.1.3, we draw bonds representing MPS correlations in orange, and bonds encoding the Hamiltonian in blue. (b) is the graphical representation of eq. (2.3): Contracting an MPS reproduces the coefficient tensor $c_{\sigma_1,\ldots,\sigma_L}$. Bonds 0 and L are one dimensional, and are therefore not shown tensor legs. (c) shows a MPO tensor with four indices. Higher-rank tensors can always be decomposed into rank-three tensors. Expectation values are computed by contracting a tensor network as depicted in (d). Here, the 'upper' MPS tensors are obtained through Hermitian conjugation. The choice of shape for each tensor is inspired by refs. [119, 121].

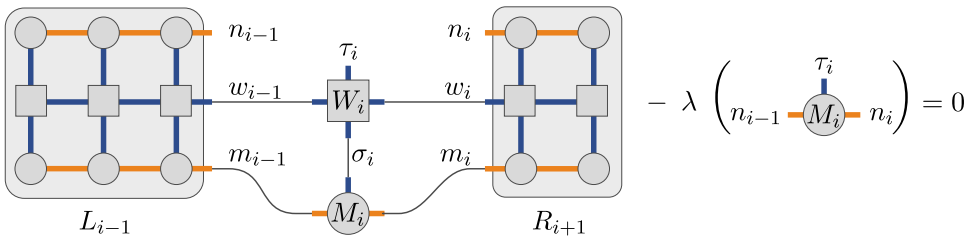

Figure 2.2: *Graphical representation of the single-site DMRG eigenvalue problem.* The optimized tensor M'_i is found via a Lanczos method where L_{i-1}, M_i, W_i and R_{i+1} are contracted along the thin lines in each iteration. The L_{i-1} (R_{i+1}) tensors can be restored from the previous right (left) DMRG sweep.

since it tends to perform better when the Hamiltonians are inhomogeneous, or contain long-range terms. The choice of perturbation generally affects numerical cost and speed of convergence. A detailed description of our DMRG3S method and comparison with related algorithms can be found in ref. [125].

2.1.3 Boundaries and dimensionality

The reason why DMRG works so well for ground states of 1D models is the entanglement area law: When we split a ground state of a gapped, local Hamiltonian into two, simply connected parts, their entanglement is proportional to the *area*, which separates them, rather than the volume of the subsystems [127, 128], due to exponentially decaying correlations. This *area law* is particularly favorable in 1D, because the area of any such bisection is independent of system size [129].

Entanglement entropy

To be more explicit, we partition a lattice into parts A and B, such that a state $|\psi\rangle \in \mathcal{H} = \mathcal{H}_A \otimes \mathcal{H}_B$ can be Schmidt decomposed as,

$$|\psi\rangle = \sum_j s_j \, |a_j\rangle \, |b_j\rangle \ , \quad |a_j\rangle \in \mathcal{H}_A, \ |b_j\rangle \in \mathcal{H}_B \, . \tag{2.4}$$

The entanglement entropy S_{AB} is then defined in terms of the Schmidt values s_j,

$$S_{AB} := -\sum_j |s_j|^2 \log |s_j|^2 \, . \tag{2.5}$$

We are primarily interested in the entanglement of a bipartition along one bond of the MPS. In that case, Schmidt values, or singular values are cheaply obtained during each DMRG sweep.

Importantly, the number of Schmidt values is given by the bond dimensions m at the bisection, and thus, the entanglement is bounded by $S \leq \log m$. Conversely, the entanglement area law means that finite bond dimensions m suffice to describe ground states of non-critical 1D systems.

Periodic boundaries

Most numerical methods perform better for models with periodic boundary conditions, because quasimomentum conservation can be exploited. For DMRG, this is generally not true, because periodic boundaries increase the entanglement of the MPS. As we sketch in fig. 2.3, any MPS bond then has to encode two physical nearest neighbors. Therefore, periodic boundaries generally double the entanglement at each bond, such that bond-dimensions $m \to m^2$ would be required to achieve similar precision.

Note that this rough argument assumes a homogeneous model. The entanglement of the states simulated in chapter 3, will depend on bond i. Choosing the lowest-entanglement bond to cross through the entire MPS can then improve numerical performance. This is a baby version of lattice reordering, which is important for DMRG in quantum chemistry applications [130–134].

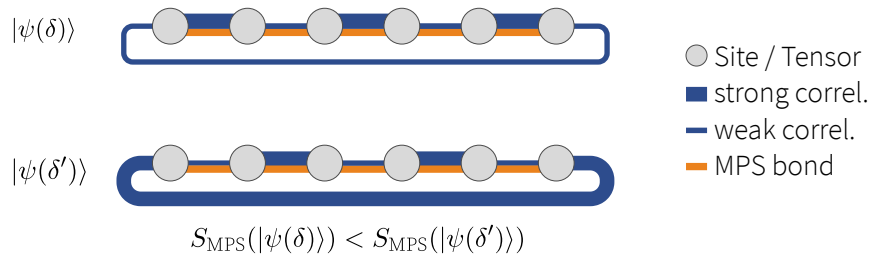

Figure 2.3: *Representing a periodic system with an open MPS.* The periodic boundary yields long-distance entanglement in the MPS chain. If the state breaks translational symmetry, shifting MPS sites can reduce the entanglement entropy, and numerical cost.

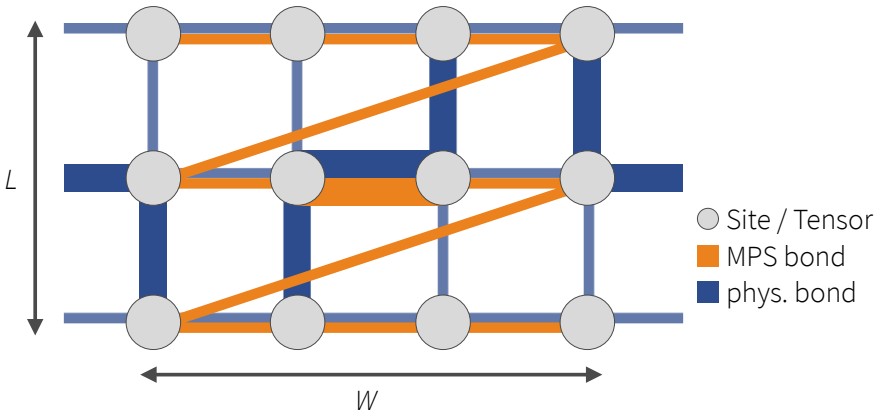

Figure 2.4: *Representing a 2D system with a 1D MPS.* The MPS (orange) moves through the 2D lattice (blue) in a "Z" shape. As an example, we show a lattice of length $L = 3$ and width $W = 4$, with periodic boundary conditions only along the width. As a result, the thick, orange MPS bond in the center needs to encode $6 = W + 2$ physical bonds, shown by the thick blue lines. Assuming an area law, the entanglement grows affinely in the system's width, requiring exponentially large MPS bond dimensions.

2D models

DMRG can also be used for finite, higher-dimensional lattice models: We just have to map the terms of a 2D Hamiltonian onto a 1D MPS chain with long-range interactions as sketched in fig. 2.4.

Unfortunately, the area law in 2D will make things difficult for us: The entanglement at any bond of such MPS will be proportional to the width W of the system. Thus, simulating 2D model generally requires bond dimensions $m \to m^{W+1}$, and we have to limit ourselves to $W \leq 6$ in this thesis.

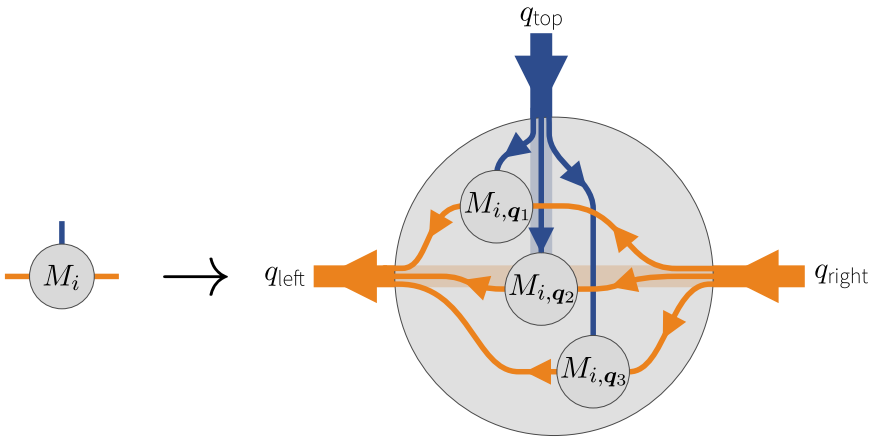

Figure 2.5: *Decomposition of an MPS using local quantum numbers.* Each dense tensor block $M_{i,\boldsymbol{q}_j}$ carries a vector (for each symmetry) of quantum numbers $\boldsymbol{q}_j = (q_{j,\text{left}} \quad q_{j,\text{top}} \quad q_{j,\text{right}})^T$, where the number of entries corresponds to the rank of M_i. For Abelian symmetries, only blocks with $q_{\text{right}} + q_{\text{top}} - q_{\text{left}} = 0$ can be nonzero, where the signs correspond to the direction of the arrows.

The exponential cost clearly stems from the fact that our ansatz does not match the physical model. Indeed, there are variational wave functions, e.g., projected entangled pair states [135, 136], which are more efficient for representing 2D area-law states. Unfortunately, though, the ground-state search in these tensor networks is more expensive than DMRG. Therefore, DMRG results compare quite well with "real" 2D methods [137–139], and we expect DMRG to be advantageous for the ladder-like systems studied here.

2.1.4 Symmetries

The performance of DMRG can be improved when symmetries of the Hamiltonian are taken into account. In this work, we use particle number conservation, and the $SU(2)$ spin symmetry. In chapter 4, we study 2D models on a cylinder, and we also exploit quasimomentum conservation along the system's width.

Abelian

In order to implement an Abelian symmetry, there need to be well-defined quantum numbers for the physical index σ_i on each site. For the particle number, this is usually trivial, because the local basis is built-up from particle-creation operators. For any state which preserves the symmetry, we can also label the MPS bonds with quantum numbers: Each rank-three MPS tensor M_i can then be decomposed into blocks labeled by a vector of quantum numbers,

$$M_i = \bigoplus_j M_{i,\boldsymbol{q}_j}\,, \qquad q_{j,\text{left}} = q_{j,\text{top}} + q_{j,\text{right}}\,, \quad \forall i,j\,, \tag{2.6}$$

and only blocks which preserve the symmetry are possible. Such tensor decomposition is sketched in fig. 2.5. Here, we also show arrows on each tensor leg, indicating the "direction" of the symmetry labels, i.e., for Abelian symmetries, the signs in eq. (2.6).

Enforcing quasimomentum conservation is slightly more involved. Firstly, our Hamiltonian needs to preserve momentum, meaning there have to be periodic boundaries. Then, we need a description of the model, where quasimomentum has local symmetry labels, i.e., express it in k space. Finally, we need to take into account that the quasimomentum is 2π periodic, and tensor blocks need to be merged accordingly. The last point is a technicality, and rather straightforward. Let us elaborate on the prior ones:

- As we discussed in section 2.1.3, periodic boundaries are generally inefficient with DMRG. This also holds for 2D models: As sketched in fig. 2.4, cylindrical boundaries increase the required bond dimensions for an area-law state. However, models with periodic boundaries may converge much quicker in $W \to \infty$, especially when twist angles are taken into account [140–142], such that the increased cost might be worth it.
- In order for k to be a local quantum number, we need to Fourier transform the model into momentum space. This simplifies the kinetic terms, but increases the complexity of real-space interactions: Onsite Hubbard repulsion will be delocalized over the entire system. This does not only have consequences for the MPO construction, but it also means that the Hamiltonian becomes nonlocal, and the entanglement area law need not hold.

Performance wise, quasimomentum conservation yields W tensor blocks, which generally reduces the numerical cost as $\mathcal{O}(m^3) \to \mathcal{O}(W(m/W)^3)$. This argument is a bit simplistic, because the entanglement may be different in Fourier space. We are not aware of a general relation of bond dimensions m in real space and momentum space, for fixed accuracy. The bond dimensions m required to achieve a target accuracy depend on model parameters, like interaction strength, system size, and particle number, but also on the ordering of k labels along the MPS [143–146]. In our simulations, we find it to be advantageous to exploit the quasimomentum conservation along the width of an elongated cylinder. For the narrow widths $W \leq 6$ studied here, the loss of the entanglement area law seems to be outweighed by the benefits of the additional symmetry. In contrast, enforcing momentum conservation along a 1D model typically yields poor performance.

Non-Abelian

Enforcing non-Abelian symmetries, e.g., $SU(2)$ spin symmetry, in DMRG is not a new idea [147]. However, they are less commonplace in tensor-network toolkits, because their implementation is technically more involved than for Abelian symmetries. We will not go into any details, which can be found in the thesis by Claudius Hubig [121], but discuss the consequences of $SU(2)$ invariance from a user's perspective.

Firstly, the dimension of the local basis is reduced: we can no longer tell $\uparrow$ and $\downarrow$ states apart, but only label them as $S = 0$ (vacuum or doubly occupied) or $S = 1/2$ (singly

occupied). These quantum numbers can be attached to each tensor leg, and, as we had seen with Abelian symmetries, only tensor blocks with matching labels may be contracted. The technical difficulties now stem from the fact that the outgoing quantum number q_{left} is not uniquely determined by the incoming legs q_{right} and q_{top}. Instead, the possible combinations are given by (generalized) Clebsch-Gordon coefficients.

For the user, this just means that in addition to making MPS tensors more sparse (as the Abelian S^z symmetry would do), we can work in a reduced space. Since the Hamiltonian is $SU(2)$ invariant, we can ignore the S^z quantum label: A single vector for spin S is sufficient to describe the $2S+1$ dimensional subspace. Therefore, we effectively reduce the required bond dimensions m_i by a factor

$$\frac{m_{i,U(1)}}{m_{i,SU(2)}} \approx \langle 2S_i + 1 \rangle \ . \tag{2.7}$$

where we average the occupation of symmetry labels at each MPS bond—i.e., S_i denotes the total spin to the right of bisection i. This relation is not exact, since $\langle S_i \rangle$ depends on the magnitude of the respective Schmidt values, while the ratio of bond dimensions does not.

For Hamiltonians with Hubbard-like particle-particle repulsion, the ground state is usually the global spin-singlet. In this case, one typically finds $m_{i,U(1)}/m_{i,SU(2)} \approx 2.5$. Since DMRG scales as m^3, and the overhead for operations involving Clebsch-Gordon coefficients is generally small, one should then expect a speed up by a factor of 16. However, the performance advantage can be much larger when the true ground state is in an $S > 0$ symmetry sector. We will discuss one such case in section 4.3.

2.2 Observables

This section will define the observables we use to characterize ground states and quantum phases. We can obviously compute the state's energy, which is optimized variationally, and expectation values of local observables, e.g. the particle number, which are used to label symmetry sectors, cf. section 2.1.4. These basics are explained in most reviews on MPS, e.g. ref. [119]. Importantly, due to enforcing $SU(2)$ spin symmetry, the S^z expectation values vanish identically,

$$\left\langle \hat{S}^z \right\rangle := \frac{1}{2} \langle \hat{n}_\uparrow - \hat{n}_\downarrow \rangle = 0 \, . \tag{2.8}$$

Furthermore, we can only compute the $SU(2)$-invariant single-particle correlators,

$$\left\langle \hat{\boldsymbol{c}}_i^\dagger \cdot \hat{\boldsymbol{c}}_j \right\rangle := \left\langle \begin{pmatrix} \hat{c}_{i,\uparrow}^\dagger & \hat{c}_{i,\downarrow}^\dagger \end{pmatrix} \cdot \begin{pmatrix} \hat{c}_{j,\uparrow} \\ \hat{c}_{j,\downarrow} \end{pmatrix} \Big|_{S=0} \right\rangle \ . \tag{2.9}$$

Details on the definition and implementation of such $SU(2)$ invariant operators can be found in ref. [121]. We can thus compute the spin-independent one-particle (reduced) density-matrix (OPDM) $\rho^{(1)}$, which contains all single-particle correlators,

$$\rho_{i,j}^{(1)} = \sum_\sigma \left\langle \hat{c}_{i,\sigma}^\dagger \hat{c}_{j,\sigma} \right\rangle \ . \tag{2.10}$$

We use the OPDM in chapter 3 to extract occupations of eigenstates of the free Hamiltonian. The noninteracting eigenbasis is obtained from a linear transformation $\hat{c}_{\nu,\tilde{k},\sigma} = \sum_j \left(\boldsymbol{a}_{\nu,\tilde{k}}\right)_j \hat{c}_{j,\sigma}$. For nondegenerate states, we can thus compute the total occupation n_ν of the νth bands

$$n_\nu := \sum_{\tilde{k}} \langle \hat{n}_{\nu,\tilde{k}} \rangle = \sum_{i,j} \left(\boldsymbol{a}_{\nu,\tilde{k}}\right)_i^\dagger \rho^{(1)}_{i,j} \left(\boldsymbol{a}_{\nu,\tilde{k}}\right)_j , \tag{2.11}$$

where $\langle \hat{n}_{\nu,\tilde{k}} \rangle = \sum_\sigma \langle \hat{n}_{\nu,\tilde{k},\sigma} \rangle$ and $\langle \hat{n}_{\nu,\tilde{k},\sigma} \rangle$ is the quasi-momentum distribution function of fermions with spin σ in the νth band, with $\nu \in \{l, m, u\}$ corresponding to the lower, middle and upper band, respectively.

2.2.1 Energy gaps

By adapting the DMRG algorithm, we can not only find the ground state but also few excited states, which gives us access to the energy gap Δ. Since we are speaking of many-body states, we can define different types of gaps.

The first gap is between the lowest-lying states for the same symmetry labels S, N (and, potentially, K). We will call this the internal gap Δ_{int}. It is obtained by performing a second DMRG run, while projecting out the true ground state [119],

$$\Delta_{\text{int}} := E_1(N, S[, K]) - E_0(N, S[, K]) . \tag{2.12}$$

This gap is related to topological quantization, i.e., the many-body Chern number of the ground state in a given symmetry sector changes only if Δ_{int} vanishes. We can already see this from eq. (1.28), where the operators $\partial_i \hat{H}$ only couple states in the same symmetry sector.

As an alternative, we can compute the lowest-energy states in different symmetry sectors. Varying the total particle number, we define the charge gap in a symmetric way,

$$\Delta_{\text{charge}}(N) = \left[E_0(N+2, S=0) + E_0(N-2, S=0) - 2E_0(N, S=0)\right]/2 . \tag{2.13}$$

This is the discretized second derivative of the ground-state energy, and can also be understood in terms of the chemical potential μ when considering ground states,

$$\Delta_{\text{charge}}(N) = \partial_N \mu(N)\big|_{S,V} = \partial_N^2 E(N)\big|_{S,V} . \tag{2.14}$$

Following this analogy, we may also compute the chemical potential as the first discretized derivative of E_0 with respect to N. A finite charge gap Δ_{charge} corresponds to an incompressible, i.e., insulating state.

Analogously, we may define the gap Δ_{spin} for ground states in different spin sectors. If the singlet is the lowest-energy sector, we define

$$\Delta_{\text{spin}}(N) = E_0(N, S=1) - E_0(N, S=0) . \tag{2.15}$$

We note, for the numerically inclined, that $\Delta_{\text{spin}} < \Delta_{\text{int}}$ is possible in this definition. Had we defined Δ_{spin} using only S^z symmetry labels, the internal gap would always be

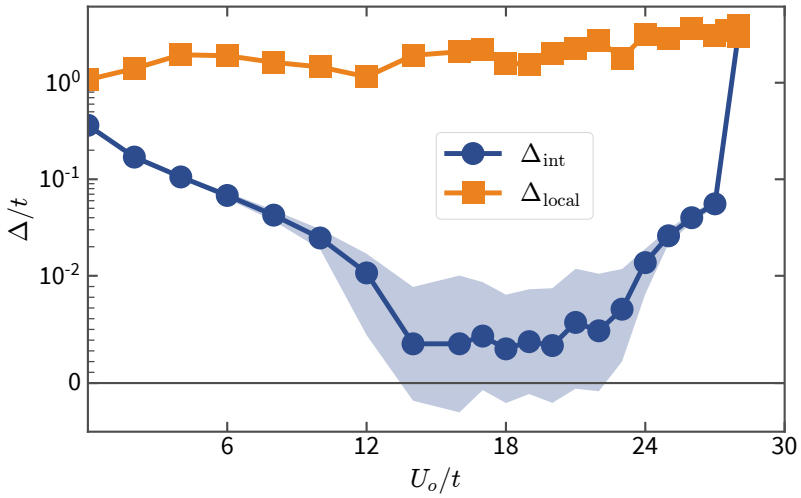

Figure 2.6: *The internal energy gap Δ_{int} compared to the local gap Δ_{local} of Lanczos states during a two-site DMRG sweep.* Data are shown for the 2D model studied in chapter 4 and parameters $L = 18$, $W = 3$, $U_d = 30t$, $\delta = \pi$ and $t_y = 1.5t$. We take the square root of the sum of the two-site energy variances $\text{var}_2(\hat{H})$ to estimate the error of Δ_{int}. This typically overestimates the error, see section 2.3.1.

smaller than or equal to the spin gap, $\Delta_{\text{int}} \leq \Delta_{\text{spin}}$, because there is a $S^z = 0$ representant in all S multiplets.

We can also define the single-particle gap as a combination of spin and charge gap,

$$\Delta_{\text{single}} = \left[E_0(N+1, S=1/2) + E_0(N-1, S=1/2) - 2E_0(N, S=0)\right]/2\,. \tag{2.16}$$

In the bulk of the system, the behavior of this gap can be related to spin and charge gaps. However, it may be qualitatively different to Δ_{charge} and Δ_{spin} in the presence of single-particle edge modes.

In chapter 4, we will also enforce quasimomentum conservation, yielding an additional $\mathbb{Z}_W$ invariant. We do not consider the gap related to this quantum number here, because the lowest-energy state is always in the sector with total quasimomentum $K = 0$, and the gap to higher K values is much larger than all other gaps. However, this relation is not generally true: We will discuss ground states with $K > 0$ in section 5.2, and such states also exist in the doped 2D Fermi-Hubbard model [121, 145].

Computing energy gaps is numerically more expensive than the initial ground-state search: For Δ_{int} and Δ_{spin}, we need to compute an excited state, and the additional states required for Δ_{charge} are generally not gapped. Therefore, the entanglement area law needs not hold. We note that there is a method to obtain larger parts of the low-energy spectrum through a single, two-site DMRG sweep [148]. Since this method is implemented in the SyTen toolkit, we used it for some systems, but could not find agreement with true orthogonalization in most cases. One such comparison is shown in fig. 2.6

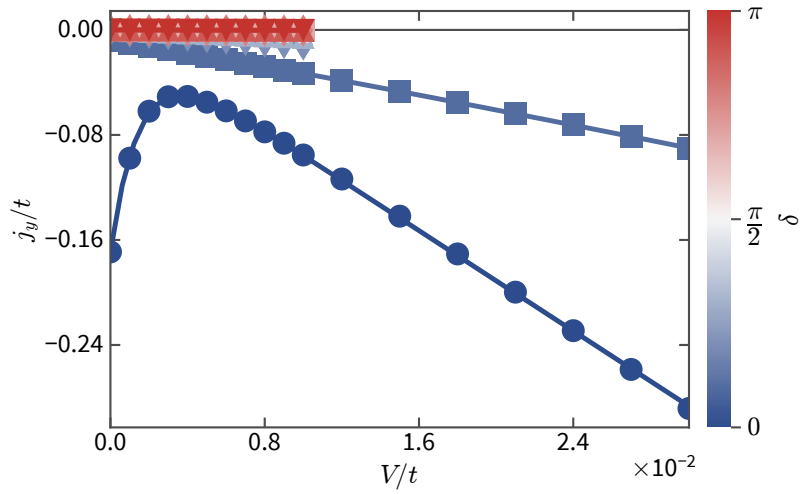

Figure 2.7: *Finite-size effects can yield non-linear contributions to response functions.* Here, we show the Hall current j_y as response to a linear potential V. For values of the twist angle $\delta \neq 0$, the response in j_y is linear in the range of V shown here. However, for $\delta = 0$, finite-size effects yield an exponentially decaying contribution as $V \to 0$. The lines are the result of fitting eq. (2.17). We have subtracted the fit parameter $a(\delta)$ for all curves. Data correspond to a cut through fig. 4.7 for $U_d = 30t$.

2.2.2 Susceptibilities

In addition to ground-state observables as a function of model parameters, we will be interested in linear ground-state responses to weak perturbations in chapter 4. In principle, we just search ground states for different strengths of the perturbation, and compute the observable of interest. In practice, this will not always give sufficient results.

Firstly, the ground states need to be accurate enough to resolve potentially very small perturbations. We will come back to improving DMRG accuracy in section 2.3. Secondly, we encounter finite-size effects which cause non-linear responses for very weak perturbations. An example for such behavior is shown in fig. 2.7: The blue curves for $\delta \approx 0$ are close to a quantum phase transition, yielding non-linear behavior of the Hall current j_y for a very weak external potential V. Clearly, performing a linear fit to these curves will not give reasonable results.

We expect a proper finite-size analysis to take care of these effects. However, performing a more elaborate data analysis for small systems is cheaper than simulating larger ones. We find that an exponentially decaying contribution explains the data in fig. 2.7 well,

$$j_y(V) \approx a + \chi_{\text{Hall}} V + b\, \mathrm{e}^{-cV} \ . \tag{2.17}$$

To avoid over fitting, we add terms $\propto |b|$ and $\propto 1/|c|$ to the cost function, such that the exponential correction is weak and long range.

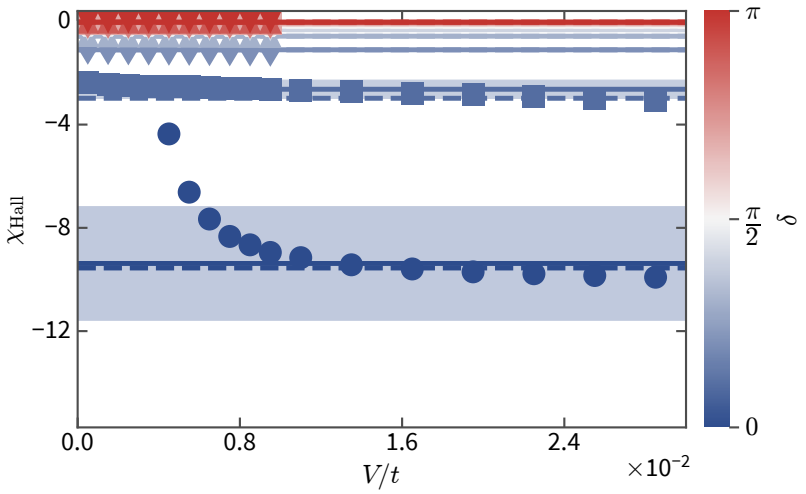

Figure 2.8: *Determining linear susceptibility through numeric differentiation.* Markers correspond to finite differences of data from fig. 2.7. The horizontal lines show the result of taking a *robust* mean similar to eq. (2.18). The shaded regions indicated the corresponding cost functions, which we interpret as the error of our fit. The dashed lines are the result of fitting eq. (2.17) as shown in fig. 2.7 for the same data set.

As an alternative method for extracting linear response, we compute finite differences, and fit a "mean" value, which disregards very far outliers, e.g.,

$$\chi_{\text{Hall}} = \arg\min \left[\sum_i \text{cost}\left(\left| \frac{j_y(V_{i+1}) - j_y(V_i)}{V_{i+1} - V_i} - \chi_{\text{Hall}} \right| \right) \right] . \tag{2.18}$$

We choose slowly increasing cost functions, like $\text{cost}(z) = \ln(1 + z)$ to suppress the effect of outliers due to nonlinearities or convergence issues.

The results of both fitting methods are compared in fig. 2.8. Here, both fits give similar results, but the more complex ansatz eq. (2.17) seems to match the data better. However, data were chosen for illustrative purposes, and in many cases we have fewer data points and more noise. For those parameters, we trust eq. (2.18) to yield less biased, and more robust results.

2.2.3 Berry curvature

For many-body systems, quasimomentum is no longer a good quantum number. Therefore, we cannot use the instructive TKNN formula [10] to compute the Berry curvature, but we need to resort to the definition based on external parameters, we motivated in section 1.3. Here, we will consider finite 1D Hamiltonians, which depend periodically on a superlattice phase δ, and a twist angle θ, to match the setting of chapter 3. However, the phase δ can also be interpreted as a second twist angle in a 2D lattice, such that this method could be applied to the models discussed in chapter 4. We do not compute the

Berry curvature for interacting 2D models, because using DMRG to find ground states on a toric geometry is exceedingly expensive, cf. section 2.1.3.

We will use the method published by Fukui et al. [149], which directly corresponds to the definitions from Niu et al. [113] for a discrete set of models for parameter (δ, θ). This approach replaces the derivates used in eq. (1.21) with a line integral around each plaquette in parameter space $(\delta, \theta) \to (\delta', \theta) \to (\delta', \theta') \to (\delta, \theta') \to (\delta, \theta)$. This is pretty much the same idea as discretizing the vector potential $\boldsymbol{A}$ to arrive at the Hofstadter model, cf. eq. (1.50). The resulting expression is, of course, gauge independent and does not require derivatives, which tend to be numerically unstable,

$$\mathcal{F}(\delta, \theta) = \Im \ln \frac{\langle \delta, \theta \,|\, \delta', \theta \rangle \langle \delta', \theta \,|\, \delta', \theta' \rangle}{\langle \delta, \theta' \,|\, \delta', \theta' \rangle \langle \delta, \theta \,|\, \delta, \theta' \rangle} , \tag{2.19}$$

$$\hat{H}(\delta, \theta) \,|\delta, \theta\rangle = E_0(\delta, \theta) \,|\delta, \theta\rangle \ . \tag{2.20}$$

We will generally use a homogeneous spacing $\Delta_{\delta,\theta}$ for the parameters,

$$\delta' := \delta + \Delta_\delta \,, \quad \theta' := \theta + \Delta_\theta \,. \tag{2.21}$$

The step size $\Delta_{\delta,\theta}$ has to be chosen with some care, because the resulting many-body Chern number,

$$C = \frac{1}{2\pi} \sum_{\delta,\theta} \mathcal{F}(\delta, \theta) \,, \tag{2.22}$$

will always be an integer, even if it is the wrong one, e.g. if the grid is too coarse. We find that taking the real part of the overlaps in eq. (2.19), i.e.,

$$\mathrm{err}_{\mathcal{F}}(\delta, \theta) \approx \Re \ln \left\langle \delta, \theta \,\middle|\, \delta', \theta \right\rangle \left\langle \delta', \theta \,\middle|\, \delta', \theta' \right\rangle \left\langle \delta', \theta' \,\middle|\, \delta, \theta' \right\rangle \left\langle \delta, \theta' \,\middle|\, \delta, \theta \right\rangle \ , \tag{2.23}$$

gives a good check for numerical consistency. Using MPS, calculating the overlaps in eq. (2.19) is straightforward once the ground states are found. The Berry curvature for one strongly-correlated insulating phase is shown in fig. 2.9 as an example.

Symmetry in parameter space

The family of Hamiltonians, whose ground states give the topological invariant in eq. 2.22 is defined on a torus $\{\hat{H}(\delta, \theta)\}_{\mathbb{T}^2}$, and we choose the parameters to be 2π periodic. However, in chapter 3, the Hamiltonian will exhibit a higher symmetry with respect to δ: Shifting $\delta \to \delta + 2\pi/q$, merely translates the lattice by j sites. Here, q is the denominator of the wave number $\alpha = p/q$ of the superlattice, and j is defined through the modulo inverse,

$$pj = 1 \mod q \,, \quad \text{where} \quad j > 0 \,. \tag{2.24}$$

Since the lattice is periodic, a translation does not change physical properties, but it does change the MPS description and its entanglement, cf. section 2.1.3. Therefore, it is advantageous to restrict DMRG simulations to a subset of $\delta \in [0, 2\pi)$, and to infer the full Berry curvature by exploiting the symmetry.

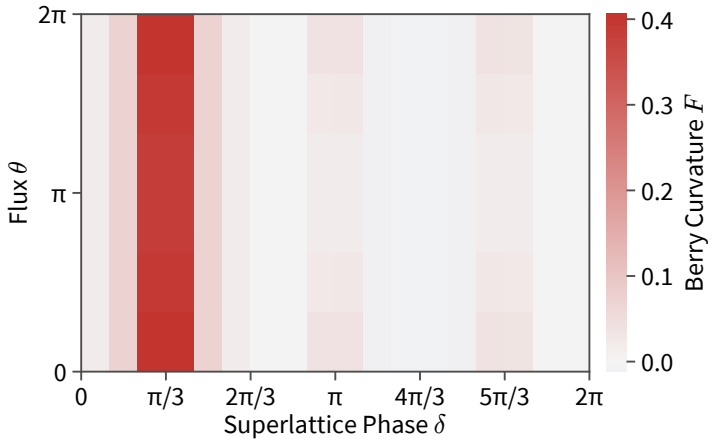

Figure 2.9: *Berry curvature for a strongly interacting model.* Data are computed for the models from chapter 3 for $L = 24$, $V = 3t$, $U = 12t$ and $\rho = 2/3$. The integrated curvature yields a Chern number $C = 1$. Only ground states for $\delta \in [0, 2\pi/3)$ were simulated. All other overlaps were obtained exploiting the symmetry in parameter space, see section 2.2.3. The curvature is computed from 6×6 values for the parameters δ and θ.

Restricting the ground-state search to parameters $\delta, \delta' \in [0, 2\pi/q)$, we can construct the remaining states via,

$$|\delta + 2\pi/q, \theta\rangle = \hat{T}_j \exp\left(-i\theta \sum_{l=0}^{j-1} \hat{n}_l\right) |\delta, \theta\rangle \ . \tag{2.25}$$

where the phase stems from the inhomogeneous implementation of the twisted boundary conditions in section 3.1. The operator $\hat{T}_j$ translates the state by j sites, which can be realized with MPS by a repeated application of SWAP gates. Such gates are commonly used for time-evolution methods [150, 151].

We can use eq. (2.25) to find the remaining terms of eq. (2.19). If both superlattice phases δ and δ' are shifted, the overlap remains unchanged,

$$\left\langle \delta + 2\pi/q, \theta \,\middle|\, \delta' + 2\pi/q, \theta \right\rangle = \left\langle \delta, \theta \,\middle|\, \delta', \theta \right\rangle \ . \tag{2.26}$$

For different values of θ, the overlap will change as we translate δ and δ' by $2\pi/q$,

$$\left\langle \delta + 2\pi/q, \theta \,\middle|\, \delta + 2\pi/q, \theta' \right\rangle = \langle \delta, \theta | \left[\exp\left(i\left(\theta - \theta'\right) \sum_{l=0}^{j-1} \hat{n}_l \right) |\delta, \theta'\rangle \right] \ . \tag{2.27}$$

Finally, we have to take special care for overlaps between the regions $\delta \in [0, 2\pi/q)$ and $\delta \in [2\pi/q, 4\pi/q)$. In this case, the translation operators $\hat{T}_j$ do not cancel, and we need to shift the MPS,

$$\langle 2\pi/q - \Delta_\delta, \theta \,|\, 2\pi/q, \theta\rangle = \langle 2\pi/q - \Delta_\delta, \theta | \left[\hat{T}_j \exp\left(-i\theta \sum_{l=0}^{j-1} \hat{n}_l\right) |0, \theta\rangle \right] \ . \tag{2.28}$$

Importantly, the Berry curvature is not invariant under a transformation $\delta \to \delta + 2\pi/q$ due to inhomogeneous gauge choice in section 3.1, and the overlaps have to be computed after the operator application. The Berry curvature shown in fig. 2.9 is computed from ground states for six values of $\delta \in [0, 2\pi/3)$ and six different twist angles $\theta \in [0, 2\pi)$, which is the spacing we use for most simulations in section 3.3.

2.3 Convergence

Having sketched the DMRG algorithm, we shall touch on how to improve and verify its convergence. There are generally two reasons why DMRG gives wrong results:

(i) The maximal bond dimensions m are insufficient for a "good" description of the true ground state. The DMRG result is then not an eigenstate of $\hat{H}$, but a low-entanglement superposition of low-energy states. As the contribution of the true ground state should increase with bond dimensions, extrapolation can improve the results.

(ii) DMRG can also get stuck due to a bad initial MPS, or an insufficient number of sweeps. This is more common in 2D, or periodic 1D lattices, where DMRG can have a hard time moving particles through the MPS. The result can still be an eigenstate of $\hat{H}$, such methods for detecting (i) are generally insensitive to this problem.

Most of the systems studied in this thesis are numerically rather simple, given the optimized toolkit [120], and available computational resources. Therefore, we are generally not too worried about (i). However, we will study a rather high-dimensional parameter space, which requires many DMRG runs, and thus, robust methods to avoid (ii).

2.3.1 Energy variance

If the bond dimensions m are insufficient to represent the true ground state $|\psi_0\rangle$ of a Hamiltonian $\hat{H}$, DMRG will end up in some superposition of eigenstates $\{|\psi_n\rangle\}$. This can be detected by computing the variance of $\hat{H}$ for the DMRG result $|\psi_{\text{DMRG}}\rangle$,

$$\text{var}\left(\hat{H}, \psi_{\text{DMRG}}\right) := \left\langle \psi_{\text{DMRG}} \middle| \hat{H}^2 \middle| \psi_{\text{DMRG}} \right\rangle - \left\langle \psi_{\text{DMRG}} \middle| \hat{H} \middle| \psi_{\text{DMRG}} \right\rangle^2 . \tag{2.29}$$

The variance is zero if, and only if, $|\psi_{\text{DMRG}}\rangle$ is an eigenstate of $\hat{H}$. If we assume that only the two lowest-energy states contribute,

$$|\psi_{\text{DMRG}}\rangle = a\,|\psi_0\rangle + b\,|\psi_1\rangle\ , \qquad a, b \in \mathbb{C}\,, \tag{2.30}$$

the error of the DMRG result becomes,

$$\Delta_{\text{DMRG}} := \left\langle \psi_{\text{DMRG}} \middle| \hat{H} \middle| \psi_{\text{DMRG}} \right\rangle - \left\langle \psi_0 \middle| \hat{H} \middle| \psi_0 \right\rangle = |b|^2 \left(E_1 - E_0\right) . \tag{2.31}$$

Using the internal gap $\Delta_{\text{int}} := E_1 - E_0$ (cf. section 2.2.1), we can furthermore compute the variance,

$$\text{var}\left(\hat{H}, \psi_{\text{DMRG}}\right) = \left(|b|^2 - |b|^4\right) \Delta_{\text{int}}\,. \tag{2.32}$$

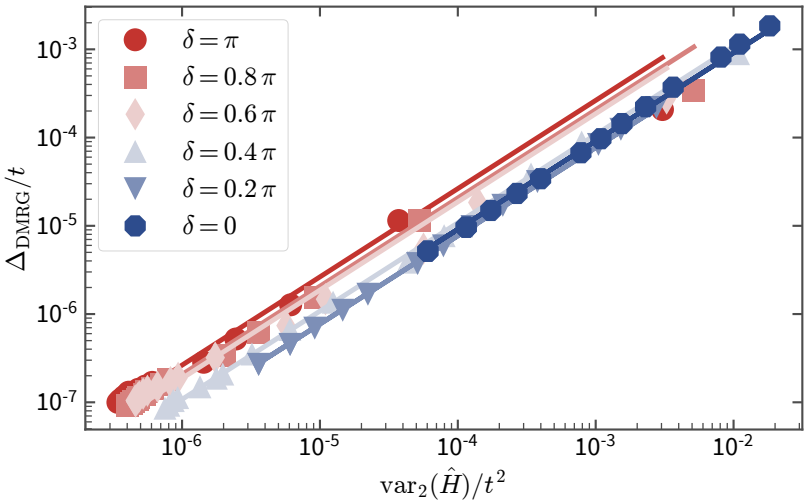

Figure 2.10: *Estimating the DMRG error* Δ_{DMRG} *from the two-site variance* var_2. We estimate the true ground-state energy E_0 by assuming a linear dependence $\Delta_{\mathrm{DMRG}} = c(\delta)\,\mathrm{var}_2(\hat{H}, \psi_{\mathrm{DMRG}})$. The coefficient $c(\delta)$ is obtained by a fit to the shown data sets. Results were computed for the 2D model discussed in chapter 4 for parameters $L = 18$, $W = 3$, $U_d = 25t$, $U_o = 15t$ and $t_y = 1.5t$, which corresponds to a numerically rather challenging regime. Bond dimensions up to $m_{SU(2)} = 2 \times 10^4$ were used for each curve, however, the accuracy depends strongly on the value of the twist angle δ.

Our assumption in eq. (2.30) requires the DMRG error to be significantly smaller than the internal gap $\Delta_{\mathrm{DMRG}} \ll \Delta_{\mathrm{int}}$. We can thus approximate to low orders,

$$\Delta_{\mathrm{DMRG}} = \Delta_{\mathrm{int}} \frac{1 - \sqrt{1 - 4\,\mathrm{var}\left(\hat{H}, \psi_{\mathrm{DMRG}}\right)/\Delta_{\mathrm{int}}^2}}{2} \approx \frac{\mathrm{var}\left(\hat{H}, \psi_{\mathrm{DMRG}}\right)}{\Delta_{\mathrm{int}}} + \frac{\mathrm{var}\left(\hat{H}, \psi_{\mathrm{DMRG}}\right)^2}{\Delta_{\mathrm{int}}^3} + \dots . \tag{2.33}$$

This relation is interesting, because Δ_{int} is a quantity we typically try to compute, see section 2.2.1.

Unfortunately, computing $\langle \hat{H}^2 \rangle$ is significantly more expensive than evaluating $\langle \hat{H} \rangle$ or performing the ground-state search. Instead, we use an approximation to var, the two-site variance var_2 [152]. As shown in this reference, var_2 can be very accurate, especially for $\mathrm{var}(\hat{H}) < 10^{-8}t$, when formally exact methods can fail due to insufficient floating point precision. For the models studied in ref. [152], the variance is on the same order as the true DMRG error.

As shown in fig. 2.10, the two-site variance seems to be proportional to the true error for our models. However, the prefactor should depend on model parameters, as we expect it to be related to the energy gap, cf. eq. (2.33). For the simulations shown in

fig. 2.10, our error estimate in eq. (2.33) does not seem to hold, but the DMRG error is much smaller:

	$\delta = 0$	$\delta = 0.2\pi$	$\delta = 0.4\pi$	$\delta = 0.6\pi$	$\delta = 0.8\pi$	$\delta = \pi$
$\mathrm{var}_2(\hat{H})/\Delta_{\mathrm{DMRG}}/t$	11.0	13.0	9.36	6.00	5.38	4.42
Δ_{int}/t	0.075	0.065	0.061	0.052	0.050	0.0499

There are two obvious explanations for this discrepancy:

- var_2 might not be a good approximation to the full variance for 2D models with long-range entanglement in the MPS.
- Our ansatz in eq. (2.30) is wrong, and higher excited states contribute to the low-*entanglement* DMRG result.

We find the second point to be more convincing, since we generally expect $\mathrm{var}_2 \leq \mathrm{var}$, but further research is necessary. For now, we will just use the result $\Delta_{\mathrm{DMRG}} \propto \mathrm{var}_2(\hat{H}, \psi_{\mathrm{DMRG}})$ and assume that both quantities are on the same order of magnitude.

2.3.2 Initial states and sweeping

Making sure that DMRG does not get stuck in the wrong state is conceptually easy, but requires more care as the number of different DMRG simulations increases. Our approaches fall into three categories:

- Improving the inital state for DMRG. Starting from states which are believed to be similar to the true ground state can greatly improve convergence speed, but will generally bias the ground-state search.
- Adding additional terms to the Hamiltonian to "guide" DMRG. The terms are usually ramped down in later stages of the ground-state search, but bias the algorithm, e.g. might break a symmetry of the ground state.
- Post-selecting DMRG results. Ideally, one has obtained multiple DMRG results for the same parameters, using different initial states, or sweeping procedures. As DMRG is a variational method, the more accurate result is then determined by the lower energy. We can extend this energy comparison to weakly-perturbed states, which we compute to determine susceptibilities, cf. section 2.2.2.

Reusing initial states

Several times in this thesis, we will sample over a twist angle, or, equivalently, a superlattice phase δ. It is tempting to think that twist angles do not significantly affect physical properties. However, for narrow systems this is wrong, and we are particularly interested in the values of δ where states become degenerate.

In this case, biasing DMRG can be advantageous: In fig. 2.11, we compare the energies of a left- $E_{\leftarrow}$ and right-moving $E_{\rightarrow}$ parameter sweep over δ. The model exhibits nearly-degenerate edge states which are notoriously hard to resolve when starting from a random

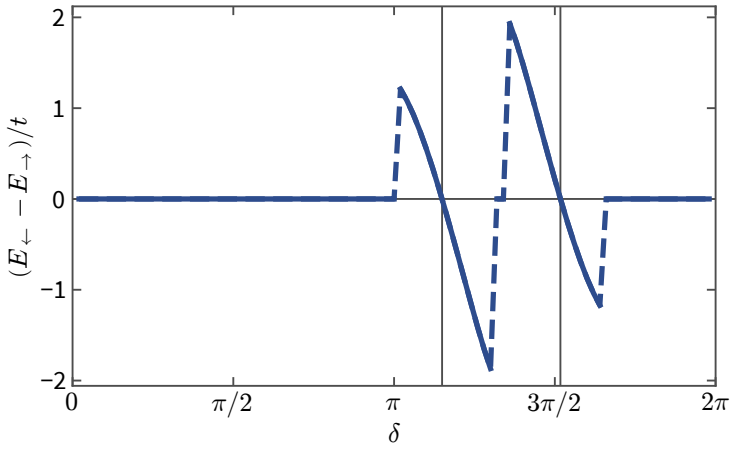

Figure 2.11: *Reusing DMRG results for a parameter sweep.* We perform a left $\leftarrow$ (right $\rightarrow$) sweep over the parameter δ, i.e., go from $\delta \to \delta - 2\pi/100$ ($\delta \to \delta + 2\pi/100$), and reuse a truncated version of the previous DMRG result as initial state. For some values of δ, there are edge states in our system. By the choice of initial state, DMRG is biased towards keeping the previous edge state, even if the other one becomes energetically favorable. As indicated by the gray, vertical lines, we can thus determine the parameters where both edge states are degenerate. The dashed lines indicate where DMRG jumps to the true ground state, despite the wrong starting point. For other values of δ, both energies agree to machine precision, $|E_{\leftarrow} - E_{\rightarrow}| \approx 10^{-14} t$. Data were computed for fig. 3.19, for length $L = 120$, and interaction strength $U = 3.2t$.

initial MPS. Instead, we truncate the DMRG result for δ to bond dimensions $m' \approx 0.1\, m$, and use it as initial state for δ'. DMRG will then quickly converge to a low energy result, but it will require several iterations to move the edge state through the model. Being aware of this bias, we sweep over δ in both directions, and obtain consistent results for both edge states.

Using initial states as bias is also advantageous when computing ground-state susceptibilities in section 2.2.2. There, we compute ground states for different values of a weak perturbation. A "perfect" overlap with the true ground state might not be necessary in that case, but it is important that the superposition of eigenstates in the DMRG result is unchanged as we increase the perturbation strength.

Sweeping

Having discussed the advantages of biasing DMRG towards previously obtained results: Most simulations in this thesis were started from random initial states. While this is generally good enough for 1D models, systems with periodic boundaries, as studied in chapter 3, sometimes required up to a thousand sweeps at small bond dimensions in order to converge. This was particularly problematic for strong superlattice potentials,

which effectively reduce the tunneling rate along the lattice. In these cases, it is very effective to include long-range hopping terms between superlattice cells, or to ramp-up the strength of the superlattice potential while sweeping.

2.3.3 Energy filtering for weak perturbations

Measuring susceptibilities requires particularly accurate DMRG results. We are interested in the ground-state response to very weak perturbations, in order to remain in the regime of linear response, cf. section 1.4.1. Depending on model Hamiltonian, this may require perturbations smaller than $10^{-3}t$, and generally yields responses on a similarly small scale.

However, we can use the assumption of linear response to our advantage, and require linear behavior of the ground-state energy $E_{\text{gs}}(V)$ on perturbation strength V,

$$E_{\text{gs}} = E_{\text{gs}}(V) + cV\,. \tag{2.34}$$

In section 4.1.2, we perturb the system using a linear potential, which is, in our definition, a positive semi-definite operator. It follows that the response coefficient $c \geq 0$ is nonnegative.

Starting from a DMRG result for potential strength V, we truncate the state, and use it as starting point for $V + \Delta_V$. Thus, the DMRG error $\Delta_{\text{DMRG}} = E_{\text{DMRG}}(V) - E_{\text{gs}}(V)$ should only decrease as V is increased step by step, while the energy $E_{\text{gs}}(V)$ increases with V.

As a result, we expect $E_{\text{DMRG}}(V)$ to be a convex function, and we find an approximation E^*_{gs} by fitting the lower, linear envelope to the DMRG data. In practice, we use a asymmetric, differentiable cost function for the fitting procedure,

$$\begin{aligned}\text{cost} = \sum_V \Bigg(& -A\left(E^*_{\text{gs}}(V) - E_{\text{DMRG}}(V) + O\right) \\ & + \exp\left(B\left[E^*_{\text{gs}}(V) - E_{\text{DMRG}}(V) + O\right]\right)\Bigg)\,.\end{aligned} \tag{2.35}$$

The prefactor B controls the allowed deviation below the "lower envelope", and large values of $B \approx 10^2, \ldots, 10^6/t$ are chosen for accurate results. The value of A did not affect the result significantly, and was generally chosen as $A \approx 1/t$. Unfortunately, we can only verify these parameter choices heuristically, by studying results of the fit procedure similar to fig. 2.13. The term O denotes an offset shifting the minimum of the cost to the position $E^*_{\text{gs}} = E_{\text{DMRG}}$, i.e., $O := 1/B \log A/B$. The shape of the cost function for typical parameters is shown in fig. 2.12. This figure also includes real DMRG results after the fitting procedure, and their contribution to the sum in eq. (2.35).

We choose a smooth cost function in order to improve the convergence of the minimization method. Using automatic differentiation via the Autograd package [153] in Python, we find robust results for sufficiently large data sets. The downside of using a smooth function is, that we will allow $E_{\text{DMRG}} < E^*_{\text{gs}}$ in some cases, as shown in fig. 2.12 on the left. Since we are not really interested in the precise value of E_{gs}, but only use E^*_{gs}

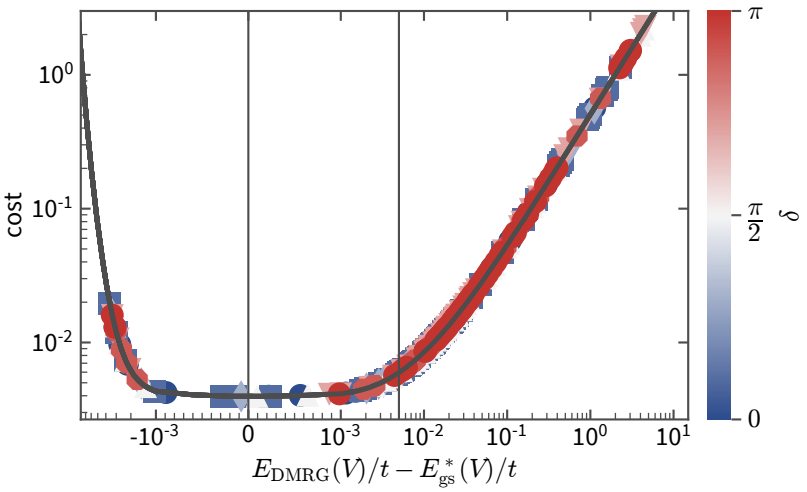

Figure 2.12: *Cost function for fitting a lower envelope.* The colored data points correspond to summands in eq. (2.35) after minimization. For the parameters $A = 1/t$, $B = 10^3/t$ shown here, we can reduce the error to roughly $\Delta_{\mathrm{DMRG}} \lesssim 10^{-2}t$, by choosing a cutoff after minimization. The gray line at $\Delta_{\mathrm{cutoff}} = 5 \times 10^{-3}t$ denotes the maximal deviation from E^*_{gs} we allow in this case. Data are computed for the hybrid-space model discussed in chapter 4, and parameters $L = 12$, $W = 6$, $U_d = 18t$, $U_o = 0$ and multiple values of the twist angle $\delta \in \{0, 0.1, 0.3, 0.5, 0.7, 0.9, 1\} \times \pi$. The result of the filtering procedure is shown in fig. 2.13.

to define a threshold to filter data, we think this is not an issue, as long as the cutoff is on similar order as the minimal deviation, $\Delta_{\mathrm{cutoff}} \approx -\min(E_{\mathrm{DMRG}} - E^*_{\mathrm{gs}})$. Given sufficient data quality and quantity, we can typically find a range of Δ_{cutoff} where the susceptibilities do not depend on the precise value of the cutoff.

The result of the fitting and filtering procedure is shown in fig. 2.13. Data are shown for a system with large circumference $W = 6$, such that convergence was more problematic. Therefore, we used multiple random initial states and different step sizes Δ_V, yielding this rather large, but inhomogeneous data set.

This filtering method is by no means crucial: For the smaller system widths, which we usually consider, only very few data points will be filtered out. However, these few outliers can effect the results quite drastically.

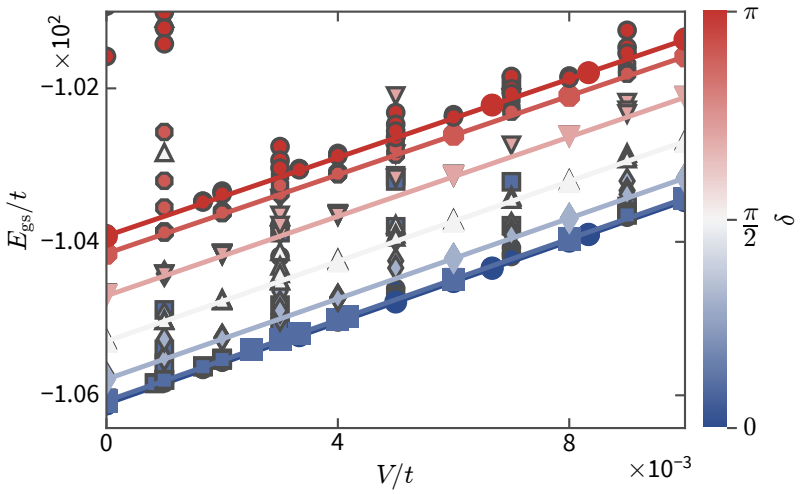

Figure 2.13: *Filtering DMRG results by comparing variational energies.* Data are shown for the hybrid-space Hofstadter-Hubbard model with parameters $W = 6$, $L = 12$, $U_d = 18t$, $U_o = 0$. Markers represent variational DMRG results, those with gray outline lay above the threshold $\Delta_{\mathrm{cutoff}} = 5 \times 10^{-3}t$ shown in fig. 2.12, and will be ignored in further analysis. Due to the strong dependence of E_{DMRG} on V and δ, only extreme outliers can be seen with the bare eye. The lines are the result of fitting eq. (2.34) using the lower envelope in eq. (2.35).

3 Interacting charge pumps

In this chapter, we will employ the analogy of 2D quantum Hall models and 1D charge pumps we have discussed in section 1.5.2, and study the interplay of interactions and topological properties in a family of 1D models. This chapter mostly follows our first publication [1].

The non-interacting Hofstadter model [11] can be mapped exactly to a family of 1D lattice models with an applied superlattice potential (bichromatic lattice), sketched in fig. 3.1. Varying the phase δ adiabatically, i.e., shifting the superlattice, this family of models corresponds directly to the charge pumps discovered by Thouless [55]. Such charge pumps have been studied in ultracold atoms, realizing superlattices realized by using standing-wave laser potentials, whose relative phase is varied slowly in order to drive the pump [58, 59, 100] (see [62, 102] for higher-dimensional versions).

These experiments with (commensurate) superlattices, as well as the theoretical interest in charge pumps, triggered theoretical investigations of 1D superlattice Hamiltonians, and the many-body physics of fermions and bosons in these systems (see, e.g., [154–158]). For a superlattice with a wavelength double the base lattice length, as studied previously [58, 59], one produces the Rice-Mele model [159], a paradigmatic model for topological charge pumps with spatially dependent potentials and tunneling strengths.

The topological quantization of charge transport in Thouless pumps requires that the system remains in its ground state as the Hamiltonian parameters are varied. This implies that the unique many-body ground state must remained gapped, such that an adiabatic limit is well defined. Therefore, there has been great interest in finding insulating quantum phases for both bosonic [157, 160–163] and fermionic [155, 160] systems.

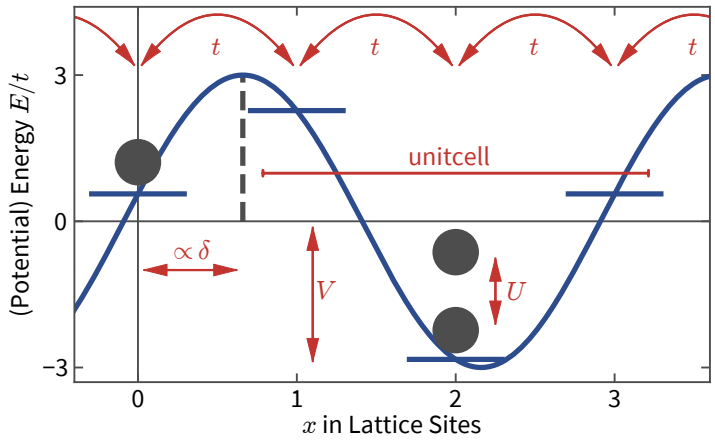

Figure 3.1: *Schematic representation of the superlattice model.* Fermions hop between adjacent sites with rate t and the onsite potential strength varies cosinusoidally with amplitude $V = 3t$. The superlattice potential is invariant under translations by $q = 3$ sites and shifted with the phase δ. If there are two particles on one lattice site, the energy is increased by U.

Furthermore, one can also establish an analogy to the quantum spin Hall effect by studying families of such 1D Hamiltonians with a spin-dependent optical potential [155, 160]. This requires that one works with two-component gases. Recently, anyons have also been studied: A variation of the statistical angle, i.e., exchange statistics, can also drive transitions between phases with different topological properties [164].

The Hubbard model in the presence of onsite potentials has been studied previously in the context of the ionic Hubbard model [165–184]. Most of this attention has been to the two-site periodic potential [165–167, 170–177, 179–182, 184], although some extensions to the three-site model have also been studied [168, 178, 183], which apply to our model at certain values of the superlattice phase. In the two-site version, it was found that at half filling, the system undergoes a sequence of transitions from a band-insulating state to a correlated insulator (CI) with increasing U, with an intermediate spontaneously-dimerized insulating (SDI) phase which breaks the lattice-inversion symmetry [165–167, 170–177, 179–182, 184].

We then use our knowledge of the phase diagram to study the topological properties of various families of adiabatically-connected 1D Hamiltonians, parameterized by δ and a twist angle θ (introduced via twisted boundary conditions). We classify these families by a many-body Chern number, an integer-quantized topological invariant. In the limit of large systems, the Chern number corresponds to the quantized charge transport in a Thouless charge pump [10], which could readily be observed in an experiment.

We find that the presence of quantum phase transitions in our model leads to interaction-induced changes in the Chern number. Along with numerical evidence, we provide an intuitive explanation for these topological transitions based on the atomic limit and properties of the band structure. An essential aspect is sketched in fig. 3.2: Depending on whether $U \ll V$ or $U \gg V$, the lowest site in the unit cell is doubly or singly occupied, respectively. This behavior survives away from the atomic limit, in the sense that one can think of the $U \ll V$ case as a (doubly) filled lowest band, while in the $U \gg V$ case, the two lowest bands are effectively filled with only one component. These situations translate into different total Chern numbers on finite systems.

Furthermore, we show that the topological structure can be understood in terms of degeneracies associated with the transition between symmetry-protected topological phases driven by the Hubbard interaction. We note that the interpretation as a topological charge pump may not be justified in the thermodynamic limit since there exist parameter regions without a global many-body gap, as required for adiabatic charge pumping. These regions occur for special values of the superlattice phase δ, as will be discussed later, and exhibit vanishing spin gaps resulting in globally gapless states. We remind the reader that in ultracold quantum-gas experiments, we are dealing with finite particle numbers that are comparable to what we reach in our numerical simulations.

Our results agree with previous literature wherever we overlap [154, 155, 157]. Furthermore, a similar transition from a band to a strongly-correlated insulator was observed in the spin-imbalanced case in the same model in [155], in this case leading to a change in the spin Chern number.

This chapter is structured as follows: In section 3.1, we start by introducing the Fermi-Hubbard-Harper Hamiltonian in detail and discuss symmetries of the model. In sec-

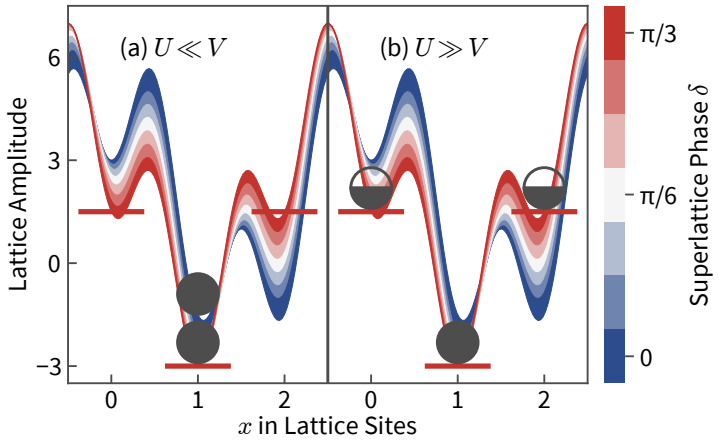

Figure 3.2: *Schematic representation of band-insulator and correlated-insulator phases in one superlattice cell.* These phases occur for $\alpha = 1/3$ and superlattice phase $\delta = \pi/3$ at density $\rho = 2/3$. For this configuration, the two "upper" lattice sites are energetically degenerate. (a) For weak repulsion $U \ll V$, both particles are localized at the lowest-potential site. (b) Double occupation is suppressed for strong interactions $U \gg V$.

tion 3.2, we present a grand-canonical phase diagram for the Fermi-Hubbard-Harper model, and we discuss physical properties of the insulating phases for single Hamiltonians $\hat{H}(\delta, \theta)$ of the family. Then, in section 3.3, we discuss topological properties of the family of ground states for $\{\hat{H}(\delta, \theta)\}_{\mathbb{T}^2}$. We conclude with a summary and an outlook contained in section 3.4.

3.1 1D Fermi-Hubbard-Harper model

We consider a one-dimensional tight-binding chain with spin-1/2 fermions. The model is expressed in terms of real-space fermionic annihilation (creation) operators $\hat{c}^{(\dagger)}_{x,\sigma}$ and particle-number operators $\hat{n}_x := \hat{n}_{x,\uparrow} + \hat{n}_{x,\downarrow}$, acting on site x, and on spin component σ,

$$\hat{H}(\delta) = -t \left[\sum_{x=0,\sigma}^{L-1} \hat{c}^\dagger_{x,\sigma} \hat{c}_{x+1,\sigma} + \text{H.c.} \right] + V \sum_x \cos(2\pi\alpha x + \delta) \hat{n}_x + U \sum_x \hat{n}_{x,\uparrow} \hat{n}_{x,\downarrow} \,. \quad (3.1)$$

where L is the number of sites. Here, t is the nearest-neighbor tunneling strength, and U is the onsite Hubbard interaction. Additionally, there is a commensurate superlattice potential with amplitude V, and wavenumber $\alpha \equiv p/q \in \mathbb{Q}$, p and q being coprime. Relative to section 1.5.2, we have changed the sign of the superlattice potential V and phase δ. As a consequence, the Chern numbers shown in fig. 3.3 have opposite sign compared to fig. 1.4. A schematic representation of the model is shown in fig. 3.1. This model corresponds to the Harper equation [94] on a lattice, with added Hubbard interactions [185].

We consider both open boundary conditions, $\hat{c}_{L,\sigma} = 0$ and twisted boundaries, $\hat{c}_{L,\sigma} = e^{i\theta}\,\hat{c}_{0,\sigma}$. The twist angle $\theta \in [0, 2\pi)$ corresponds to a flux piercing of the ring. Periodic boundary conditions are obtained for $\theta = 0$. Throughout this chapter, we are also interested in families of Hamiltonians parameterized by $\delta, \theta \in [0, 2\pi)$ defining a torus. We will refer to such families as $\{\hat{H}(\delta, \theta)\}_{\mathbb{T}^2}$. We define total particle density, $\rho = N/L$, which is twice the filling factor, owing to the spin degree of freedom. $N = \sum_x \langle \hat{n}_x \rangle$ is the total number of particles. The insulating states of interest appear at commensurate densities, i.e., $\rho = l/q$ for some integer $0 \leq l \leq 2q$, which corresponds to l total fermions per unit cell.

We will focus on the case $\alpha = 1/3$, which is the smallest-denominator case in the Harper-Hofstadter model that has band gaps. However, similar physics is expected to be found for higher values of q, as is the situation in the bosonic case [163]. The case of even q (e.g., $\alpha = 1/4$) potentially offers further interesting physics, due to the presence of a band touching around $E = 0$, although this touching is expected to be lifted in optical-superlattice experiments due to the induced modulated tunneling. However, we leave the study of these effects to later work.

3.1.1 Correspondence to Harper-Hofstadter model

As discussed in section 1.5.2, the 1D charge pump is a direct analog of 2D quantum Hall systems. Not taking interactions $\propto U$ into account, eq. (3.1) is a representation of the Hofstadter model in mixed real and momentum space: $\delta = a_y k_y$ is the position in k_y-momentum space, where a_y is the lattice spacing and $V = 2t_y$ corresponds to the hopping rate along that direction.

Expressing the onsite interaction term $\propto U$ in the original 2D Harper-Hofstadter picture, the interaction would be semi-'local' in hybrid space. That is, the repulsion is onsite in the x direction but infinite-range along the y direction. Such interactions are not found in traditional electronic materials, however, anisotropic interactions could possibly be implemented using synthetic lattice dimensions [36, 186, 187]. We will discuss the relation of this interacting 1D charge pump with the Hofstadter-Hubbard model in chapter 4. Furthermore, 1D superlattices have been realized with ultracold atoms [58, 59, 110, 111]. These 1D systems provide the main motivation for this research.

The family of 1D Hamiltonians thus inherits the topological properties of the Hofstadter model, cf. section 1.5.1. Following section 1.3, the Berry curvature is defined on a family of Hamiltonians [16, 188], which is generally the case for interacting models. For a many-body system, we can introduce twisted boundary conditions, such that the Chern number is defined with respect to the twist angle θ [113],

$$C\left(\{|\psi\rangle\}\right) = \frac{1}{\pi}\int_0^{2\pi} \mathrm{d}\theta \int_0^{2\pi} \mathrm{d}\delta\, \Im \left\langle \partial_\delta \psi(\delta,\theta) \,|\, \partial_\theta \psi(\delta,\theta) \right\rangle \,, \tag{3.2}$$

where $|\psi(\delta,\theta)\rangle$ is the unique many-body ground state.

For $L \to \infty$, twisted boundaries do not affect bulk properties [113–116], and the family $\{\hat{H}(\delta,\theta)\}_{\mathbb{T}^2}$ can realize a topological charge pump: As δ is changed adiabatically to $\delta + 2\pi$, a quantized amount of C charges is transported through a periodic system [55].

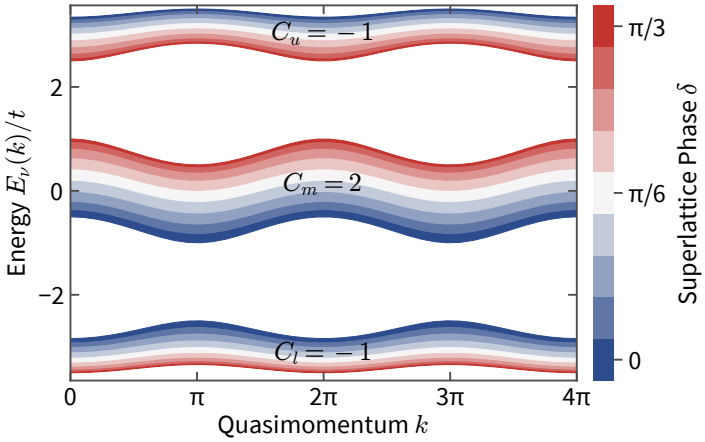

Figure 3.3: *Topological bandstructure for the noninteracting Fermi-Hubbard-Harper model for $\alpha = 1/3$, $V = 3t$, as a function of δ.* The bands correspond to the dispersion relation of the Harper-Hofstadter model, shown also in fig. 1.4, when identifying δ with the transversal momentum k_y. Thus the Chern numbers describing the topology associated with a each set of bands are the same as for the 2D Harper-Hofstadter model, where $C_{\{l,m,u\}} = \{-1, 2, -1\}$ for lower, middle and upper band respectively.

3.1.2 Symmetries

The Fermi-Hubbard-Harper model possesses several symmetries which can help understand ground-state and topological properties. In the gauge chosen for eq. (3.1), it is obvious that $\hat{H}(\delta, \theta)$ is invariant under shifts by 2π of both twist angle θ and superlattice phase δ. However, for periodic boundary conditions, there is a higher symmetry related to the superlattice phase: Shifting $\delta \to \delta + 2\pi/q$ merely corresponds to a translation of the superlattice with an additional gauge transformation. We exploit this symmetry to restrict the numerical effort for computing the Berry curvature, as described in section 2.1.4.

The q-fold symmetry of the superlattice phase δ is sometimes referred to as *fractional charge pumping* [189, 190]: When the number of charges which are transported per pump cycle $\delta \to \delta + 2\pi$ is quantized to C, this symmetry requires fractionally-quantized charge transport C/q as $\delta \to \delta + 2\pi/q$. This observation brings the fractional quantum Hall effect to mind, however, the mechanism is somehow reversed: Numerical simulations also show quantized charge transport in fractional quantum Hall systems as the twist angle of a infinite cylinder is varied adiabatically [141, 144, 191, 192]. However, in these systems, multiple pump cycles $\delta \to \delta + n \times 2\pi$ have to be completed in order to transport $C \in \mathbb{Z}$ particles, since the ground-state manifold is degenerate.

The 2D Harper-Hofstadter model is particle-hole symmetric around $E = 0$. For the Fermi-Hubbard-Harper model of eq. (3.1), this symmetry is not present at any individual value of δ. However, by simultaneously shifting $\delta \to \delta + \pi$, and $\theta \to -\theta$, the particle-hole symmetry is recovered.

The interaction term in eq. (3.1) also preserves the particle-hole symmetry: Exchanging $\hat{c}^\dagger_{x,\sigma} \leftrightarrow \hat{c}_{x,\sigma}$ in eq. (3.1), we find a shifted superlattice $\delta \to \delta + \pi$ and reversed flux $\theta \to -\theta$. Shifting θ does not change the Chern number as the curvature is integrated over the entire torus. But changing the direction of the flux θ flips the sign of the Berry curvature in eq. (3.2) and thus changes the many-body Chern number: $C(\rho, U) \to -C(2-\rho, U)$. Note that this implies $C(1, U) = -C(1, U) = 0$. Because of the particle-hole symmetry, it is sufficient to study phases and their topological properties for $\rho \leq 1$.

We further note that in the case of periodic boundary conditions, at values of $\delta = 2\pi n/3$ and $\delta = 2\pi(1/6 + n/3)$ for $n \in \mathbb{Z}$, the system also possesses an inversion symmetry. The presence of an inversion symmetry allows for the existence of one-dimensional symmetry-protected topological states [193, 194]. These special δ points are important for the understanding of possible topological properties of a family of Hamiltonians, $\{\hat{H}(\delta, \theta)\}_{\mathbb{T}^2}$. For $\delta = 0$, $2\pi/3$, and $4\pi/3$, there are no topological transitions at $\rho < 1$, yet they occur at $\rho' = 2 - \rho$ by particle-hole symmetry.

More specifically, a lattice-inversion symmetry constrains the many-body Zak phase which is defined as

$$\varphi = i \int_0^{2\pi} d\theta \, \langle \psi(\delta, \theta) | \partial_\theta \psi(\delta, \theta) \rangle \ . \tag{3.3}$$

The Zak phase can have only two values $\varphi = 0, \pi \bmod 2\pi$, differing by exactly π. These two values of the Zak phase are topological invariants that cannot change under symmetry-preserving perturbations of the Hamiltonian without closing the many-body gap.

For open boundary conditions, the choice of the unit cell can become important. This is typical of symmetry-protected topological states, where the choice of boundaries determines the presence or absence of gapless edge states [97]. In our case, a choice of $\delta = \pi/3$ leads to an intra-cell site-centered symmetry, meaning that the lattice will retain its inversion symmetry. For $\delta = \pi$ and $\delta = 5\pi/3$ the lattice loses its inversion symmetry with open boundary conditions. We refer to these situations as symmetric and asymmetric lattice configurations, respectively.

3.1.3 Strong-coupling limit

In order to understand the phases present in our model, we also use Schrieffer-Wolff (SW) perturbation theory to simplify the problem in certain limits. In particular, SW theory allows us to understand the effective spin-sector behavior typical of Mott insulators when there is a significant charge gap.

For the single-band one-dimensional Hubbard model at half-filling ($\rho = 1$), any nonzero Hubbard interaction induces a charge gap [195]. In the limit of $t \ll U$, the Hubbard interaction projects out doubly-occupied sites, as these sites have energy U. The ground state therefore lives in the manifold of singly-occupied sites.

One can then use Schrieffer-Wolff perturbation theory to derive an effective Hamiltonian which describes the low-energy physics in this manifold of states [195]:

$$\hat{H}_S^{\text{eff}} = J \sum_x \hat{\boldsymbol{S}}_x \cdot \hat{\boldsymbol{S}}_{x+1} + \mathcal{O}\left(t^2/U^2\right) \ . \tag{3.4}$$

Here, $\hat{\boldsymbol{S}}_x$ labels the spin-1/2 degree of freedom on site x and $J = t^2/U$ is the induced spin-spin interaction. The effective model is the well-known isotropic Heisenberg chain, which has gapless spin excitations [196]. Importantly, as the groundstate manifold and the original Hamiltonian have a global $SU(2)$ symmetry, the effective Hamiltonian will also contain only $SU(2)$ invariant terms.

In the present case of a model with a lower degree of translational symmetry and away from half filling, the effective model is more complicated. Following ref. [178], we can write the effective strong-coupling model as follows:

$$\begin{aligned}\hat{H} = & -t\sum_{x,\sigma}\hat{P}\left(\hat{c}^\dagger_{x+1,\sigma}\hat{c}_{x,\sigma} + \text{H.c.}\right)\hat{P} + \sum_x V\cos(2\pi x/3+\delta)\hat{n}_x \\ & + \sum_x\sum_{\eta=\pm1} t_i^{\text{ch}}\hat{P}\left[\hat{c}^\dagger_{x+\eta,\sigma}\hat{c}_{x-\eta,\sigma}\left(2\hat{\boldsymbol{S}}_x\cdot\hat{\boldsymbol{S}}_{x-\eta} - \frac{1}{2}\hat{n}_x\right)\right]\hat{P} \\ & + \sum_i J_x\left(\hat{\boldsymbol{S}}_x\cdot\hat{\boldsymbol{S}}_{x+1} - \frac{1}{4}\hat{n}_x\hat{n}_{x+1}\right).\end{aligned} \tag{3.5}$$

Here, $\hat{P} = \prod_x (1-\hat{n}_{x,\uparrow}\hat{n}_{x,\downarrow})$ projects out all double occupations, $\hat{\boldsymbol{S}}_x = \sum_{\alpha\beta}\hat{c}^\dagger_{x,\alpha}\boldsymbol{\sigma}_{\alpha\beta}\hat{c}_{x,\beta}$ are the spin operators, t_x^{ch} are the effective correlated tunneling strengths, and J_x are the effective spin couplings:

$$\begin{aligned}J_x &= \frac{4t^2U}{U^2-\Delta^2_{x,x+1}}, \\ t_x^{\text{ch}} &= \frac{1}{2}\left(\frac{t^2}{U+\Delta_{x,x+1}} + \frac{t^2}{U-\Delta_{x,x-1}}\right),\end{aligned} \tag{3.6}$$

where $\Delta_{x,x'} = V\cos(2\pi x'/3+\delta) - V\cos(2\pi x/3+\delta)$ is the potential difference between sites x and x'. Terms of higher order in t/U have been omitted. This model describes a generalized t-J model, which reduces to the homogeneous case when $V = 0$.

The strong-coupling limit ($U \gg \Delta,\, t$) can be studied by solving first for the distribution of the charge degrees of freedom, and then treating the terms proportional to J_x and t_x^{ch} perturbatively. This charge distribution can be determined by finding the ground state of a system of noninteracting spinless fermions $\hat{c}^\dagger_x$ on the lattice in question. The effective spin Hamiltonian is then obtained by projecting the Hamiltonian in eq. (3.5) onto the charge distribution.

3.2 Quantum phases of the 1D Fermi-Hubbard-Harper model

In this section, we discuss quantum phases of ground states for individual $\hat{H}(\delta,\theta)$ from the family of Hamiltonians $\{\hat{H}(\delta,\theta)\}_{\mathbb{T}^2}$. As the twist angle θ is a boundary effect, it does not affect bulk physics in the thermodynamic limit [115, 116]. However, the superlattice phase δ can affect quantum phases. For example, the SDI phase (to be discussed in section 3.2.3) appears only for certain values of δ, related to the lattice-inversion symmetry discussed in section 3.1.2.

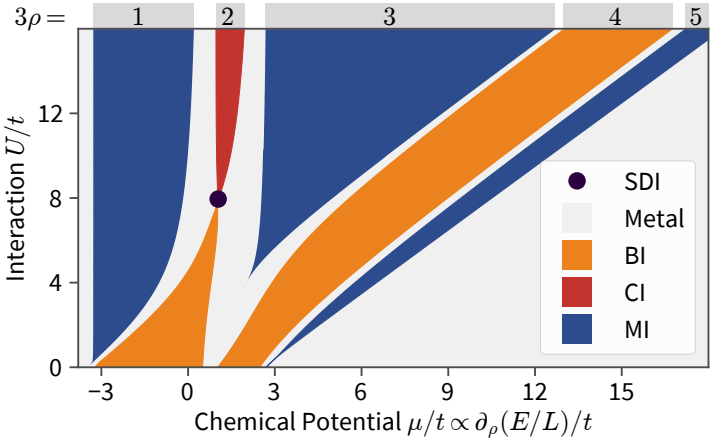

Figure 3.4: *Grand-canonical phase diagram.* Ground-state phases of the Fermi-Hubbard-Harper model with $\alpha = 1/3$, computed for $\delta = \pi/3$ and $V = 3t$ with open boundaries. For particle density $\rho \in \{2, 4\}/3$, there are band insulators (BI) for $U = 0$. At $U \approx 8t$, $\rho = 2/3$, there is a transition to a spontaneously dimerized insulator (SDI), and then to a strongly-interacting correlated insulator (CI). Mott insulators appear for half-filled bands, $\rho \in \{1, 3, 5\}/3$. The phase boundaries $\mu(U, \rho \pm 1/L)$ are extrapolated in $L \to \infty$.

Quantized charge transport in the family of Hamiltonians can only occur if the physical state is insulating for the entire pump cycle [55, 113]. Conversely, the Chern number of the manifold of ground states can only change when the many-body gap closes. Thus, we start by studying insulating phases.

In the following sections, we restrict ourselves to a three-site superlattice, $\alpha \equiv p/q = 1/3$. For this configuration, there are three separated energy bands, which are all topologically nontrivial, see fig. 3.3. Furthermore, we will choose $V = 3t$ as the strength of the potential unless stated otherwise. For this value of V/t, the band gaps are comparable to the hopping matrix elements t. We find that significantly stronger superlattice potentials do not change the physical behavior, qualitatively.

3.2.1 Grand-canonical phase diagram

In order to obtain the phase diagram for the Fermi-Hubbard-Harper model we compute ground states for various particle numbers and interaction strengths U. As mentioned in section 2.2.1, we can infer the chemical potential μ, and the $\{\mu, U\}$ phase diagram from ground-state energies for different particle numbers.

A phase diagram obtained from DMRG data for open boundaries is shown in fig. 3.4 for $\delta = \pi/3$. The analysis of the charge gap (as defined in eq. (2.13)) suggests the existence of insulating phases for five different fillings. At $\rho = 2/3$ and $4/3$, there are band insulators, already present without interactions at $U = 0$. Furthermore, for half-filled bands, $\rho \in \{1/3, 1, 5/3\}$, Mott-insulating phases emerge for $U > 0$.

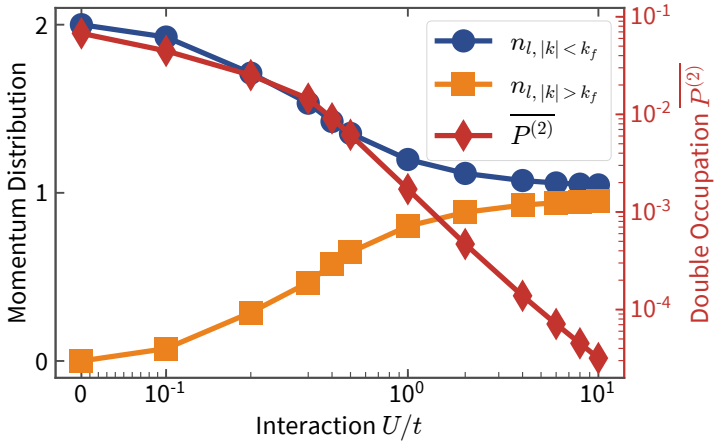

Figure 3.5: *Partially integrated momentum-distribution function and real-space double occupation for* $\rho = 1/3$. We show data for superlattice amplitude $V = 3t$ and phase $\delta = \pi/3$. $\overline{P^{(2)}}$ is the double occupation averaged over one superlattice cell. Increasing the interaction strength U suppresses double occupation for the MI phase. In momentum space, all particles remain in the lowest band, but, as U increases, states below and above the Fermi wave number k_F become evenly occupied. The lines are guides to the eye.

An interesting sequence of phases exists at filling $\rho = 2/3$: upon increasing U/t, the BI ultimately (via two transitions) turns into a correlated insulator at $U \gg t$. We use the term CI to distinguish this large U/t phase from MIs, which originate from half-filled bands at $U = 0$. The term CI is also used in parts of the literature in the same context [174]. We find evidence (see section 3.2.3) that the intermediate phase is a bond-ordered spontaneously-dimerized insulating (SDI) phase separating the BI and CI phases at density $\rho = 2/3$, indicated in fig. 3.4.

We also draw attention to the linear behavior of the phase transitions for large μ and large U. In this regime, the insulating phases have density $\rho \geq 1$, i.e., at least one Fermion per site. This makes the energy of adding a particle dominated by the interaction energy and therefore directly proportional to U.

3.2.2 Mott insulator at density $\rho = 1/3$

For particle density $\rho = 1/3$, and without interactions U, the lowest band is half-filled, and we are in a metallic phase for all δ, θ. As we saw in fig. 3.4, a charge gap opens for weak interactions and the phase appears to be a Mott insulator for all $U > 0$.

While the charge gap (cf. eq. (2.13)) is comparable to the size of the gaps for the band-insulating phases in fig. 3.4, there can be gapless spin excitations for the infinite system in this Mott insulator (see the discussion in section 3.2.2).

Increasing onsite repulsion U obviously suppresses the double occupation $P_x^{(2)}$ on all lattice sites x. In fig. 3.5, we illustrate that real-space double occupation decreases with

U. Moreover, also in momentum space, occupation numbers change as a function of increasing interaction strength. As shown in the same figure, for $U = 0$, the lower half of the lowest band is fully occupied by each spin species. When interactions increase, in the range considered in fig. 3.5, the particles mostly remain in the lowest band of the noninteracting model, but we approach a constant momentum-distribution function $\langle \hat{n}_{\nu=l,k} \rangle = 1$ for the entire lowest band.

Only considering single-particle observables $\hat{c}^\dagger_{x,\sigma}\hat{c}_{x',\sigma}$, such as particle number $P^{(1)}_x$ or the momentum-distribution function $\langle \hat{n}_{\nu,k} \rangle$, the system behaves much like free, spinless fermions at the same particle density: For a single species of fermions, double occupation is prohibited by Pauli's exclusion principle, and, without interactions, the lowest band would be singly filled at density $\rho = 1/3$.

Strong coupling limit for $\rho = 1/3$

For $\rho = 1/3$, the charge distribution is the same as that of a system with a filled lowest band of the noninteracting spinless model. One then recovers the effective model:

$$\hat{H}^{\text{eff}} = \frac{1}{2} \sum_j J^{\text{eff}} \left(\hat{\boldsymbol{S}}_j \cdot \hat{\boldsymbol{S}}_{j+1} - \frac{1}{4} \right), \tag{3.7}$$

where

$$J^{\text{eff}} \approx \frac{1}{N} \sum_{j=0}^{N-1} \left[J_j \langle \hat{n}_j \hat{n}_{j+1} \rangle' + 2t^{\text{ch}}_j \left\langle \hat{c}^\dagger_{j-1} \hat{c}_{j+1} \hat{n}_j \right\rangle' + 2t^{\text{ch}}_{j+1} \left\langle \hat{c}^\dagger_{j+2} \hat{c}_j \hat{n}_{j+1} \right\rangle' \right]. \tag{3.8}$$

The expectation values $\langle \cdot \rangle'$ are taken with respect to the spinless-fermion background [178]. This model is a "squeezed" Heisenberg chain, where the empty sites have been eliminated, and the $\hat{\boldsymbol{S}}_j$ refer to the spins attached to the jth fermion, which will be centered at the jth unit cell on average. This chain therefore has length $N = \rho L$.

The spin chain inherits symmetries from the underlying lattice and the charge distribution. For $\rho = 1/3$, this implies that the couplings are homogeneous, and we recover the standard Heisenberg model, with one spin per unit cell. The effective spin model therefore predicts that the system has gapless spin excitations in the strong-coupling limit, which is consistent with our numerical data. Note that this result is independent of δ and θ.

3.2.3 Insulators at density $\rho = 2/3$

The system at density $\rho = 2/3$ has a complicated phase diagram with several transitions. The basic structure of the phase diagram is illustrated in fig. 3.6. To give a brief overview, at $U = 0$ the system is a band insulator with a filled lower band. Apart from the symmetric lines along $\delta = \pi/3$, π, and $5\pi/3$, the BI survives at all U/t, and becomes strongly correlated as U/t increases.

Along the symmetric lines, there are two phase transitions, which are sketched in fig. 3.7. First, at U_{c_1} the system undergoes an Ising-like transition from the BI to a doubly-degenerate SDI [169, 171, 174, 178, 181]. At a larger interaction strength U_{c_2}, there is a second transition of the Berezinskii-Kosterlitz-Thouless (BKT) type to a CI with gapless spin excitations [167, 169, 171, 172, 174, 178, 181].

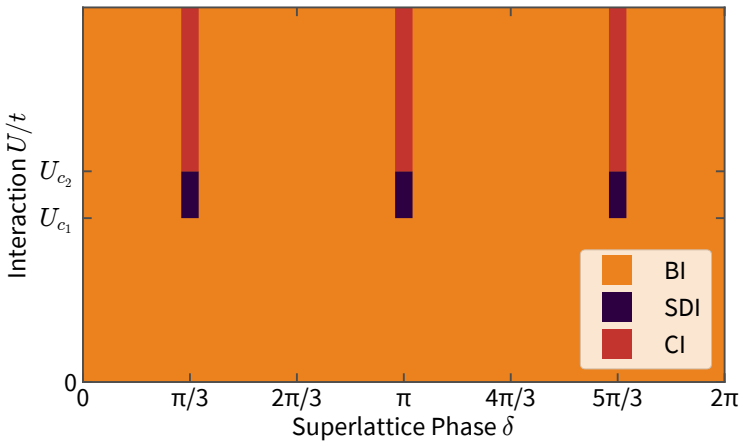

Figure 3.6: *Phase diagram for the $\rho = 2/3$ insulators.* Throughout the δ-U plane, the system is adiabatically connected to the band insulator at $U = 0$. However, along three lines at $\delta \in \{1, 3, 5\} \times \pi/3$, the lattice has a symmetry in the superlattice potential which leads to the phase structure sketched in fig. 3.7.

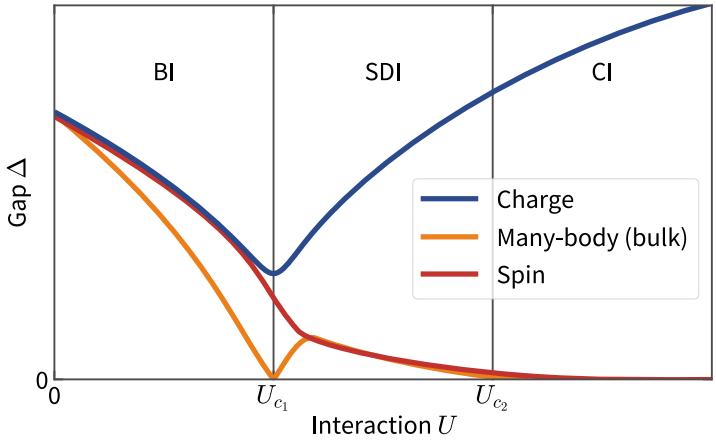

Figure 3.7: *Schematic representation of the energy-gap structure for $\delta = \pi/3$ at $\rho = 2/3$.* Along this line, there are two critical values of U, U_{c_1} and U_{c_2}. U_{c_1} marks an Ising-like transition between a band insulator (BI), and a spontaneously-dimerized insulator (SDI), as was demonstrated in previous works [171, 174, 178, 181]. The second critical value U_{c_2} is the point of a BKT-like transition between the SDI and a correlated insulator (CI). We also show the behavior of various energy gaps in these different phases for different types of excitations. The band insulator is completely gapped throughout. The global many-body gap is identical to the internal gap in the BI and closes at U_{c_1} when the ground state becomes doubly degenerate in the SDI, while the charge and spin excitations remain finite. The transition between SDI and CI at U_{c_2} occurs when the spin gap closes.

Band insulator

At fermion density $\rho = 2/3$ there is a charge gap at $U = 0$ (see fig. 3.4), corresponding to the band gap of the Hofstadter model, see fig. 3.3. We find that even strong interactions preserve the properties of the band-insulating phase for most parameters δ of the family defined in eq. (3.1). This band insulator is adiabatically connected to all points in the $\{U, \delta\}$ parameter space, except for the lines with the SDI and the gapless CI phases, as sketched in fig. 3.6. While there is no phase transition throughout this region (except at $\delta \in \{\pi/3, \pi, 5\pi/3\}$), there is a smooth change to a gapped strongly correlated state as U increases.

Spontaneously-dimerized insulating phase

At $\delta \in \{\pi/3, \pi, 5\pi/3\}$, between the CI phase and the BI phase, there is an intermediate bond-ordered phase, typical of ionic Hubbard models [165–184]. This phase has been studied by a mapping to an exactly solvable $SU(3)$ antiferromagnetic Heisenberg chain [173] where the state was found to have both spin and charge dimerization. The dimerization spontaneously breaks the lattice-inversion symmetry which occurs at these values of δ.

The situation is illustrated in fig. 3.8. The choice of boundary conditions is particularly relevant for the SDI phase, where the symmetric configuration at $\delta = \pi/3$ splits a dimer, leading directly to the existence of gapless edge modes, and the asymmetric configurations each support one of the two SDI ground states.

A numerical study of the two-site ionic Hubbard model [174] suggests that bulk many-body gap and spin gap close at different interaction strengths, indicating the two-step sequence of phase transitions, while the charge gap does not close at any point. The case of a three site unit-cell, relevant to the present case of $\alpha \equiv p/q = 1/3$ was studied in both ref. [178] and ref. [183], where the same situation was found.

To identify the spontaneously-dimerized phase, sketched in fig. 3.8, we compute the bond-order parameter:

$$\left\langle \hat{B} \right\rangle = \frac{1}{L/3} \sum_{j=0,\sigma}^{L/3-1} \left\langle \hat{c}^\dagger_{3j,\sigma} \hat{c}_{3j+1,\sigma} - \hat{c}^\dagger_{3j+1,\sigma} \hat{c}_{3j+2,\sigma} + \text{H.c.} \right\rangle . \tag{3.9}$$

For our case of a three-site superlattice ($q = 3$) with phase $\delta = \pi/3$ according to fig. 3.2, site 0 and 2 are energetically degenerate while site 1 is lower in energy.

For a system with periodic boundary conditions, the BI and CI phases preserve the lattice-inversion symmetry, implying that the bond-order parameter vanishes, i.e., $\langle \hat{B} \rangle = 0$. However, in the SDI, the lattice symmetry is spontaneously broken, leading to a doubly-degenerate ground state, and a finite value for $\langle \hat{B} \rangle$. In fig. 3.9, we show the bond-order parameter $\langle \hat{B} \rangle$ as a function of U for open boundary conditions. The finite length of the system leads to a nonzero $\langle \hat{B} \rangle$ in the BI and CI phases, but $\langle \hat{B} \rangle$ disappears in the thermodynamic limit [174, 178]. However, the appearance of the SDI phase is consistent with our data for large, but finite, system sizes.

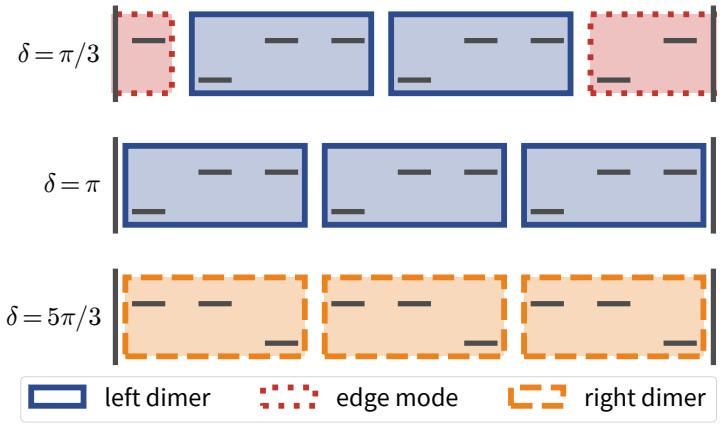

Figure 3.8: *Lattice configuration for open boundary conditions.* Different choices of δ change the boundary conditions. These boundary conditions determine edge-state properties of the ground state of the SDI phase: The two asymmetric lattice configurations $\delta = \pi$ and $\delta = 5\pi/3$, support left- and right-dimerized ground states, respectively. These dimers are combinations of the two configurations illustrated in fig. 3.2. However, for $\delta = \pi/3$, the symmetric lattice configurations support neither ground state, leading to the existence of gapless edge modes.

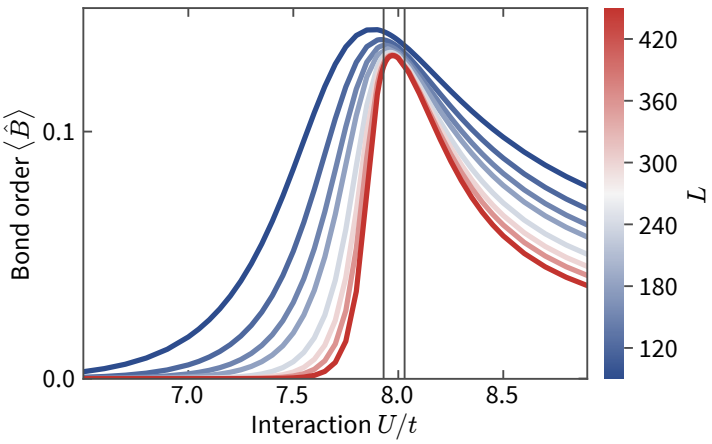

Figure 3.9: *Bond-order parameter across the BI-SDI-CI transition.* At $\delta = \pi/3$, the superlattice potential is degenerate for sites 0 and 2, and site 1 is lower in energy, as shown in fig. 3.2. Data are computed for open boundaries without inversion symmetry for $L \in \{90, 120, 150, 180, 240, 300, 360, 450\}$. The vertical lines indicate the two phase transition as determined from the gap data shown in fig. 3.10.

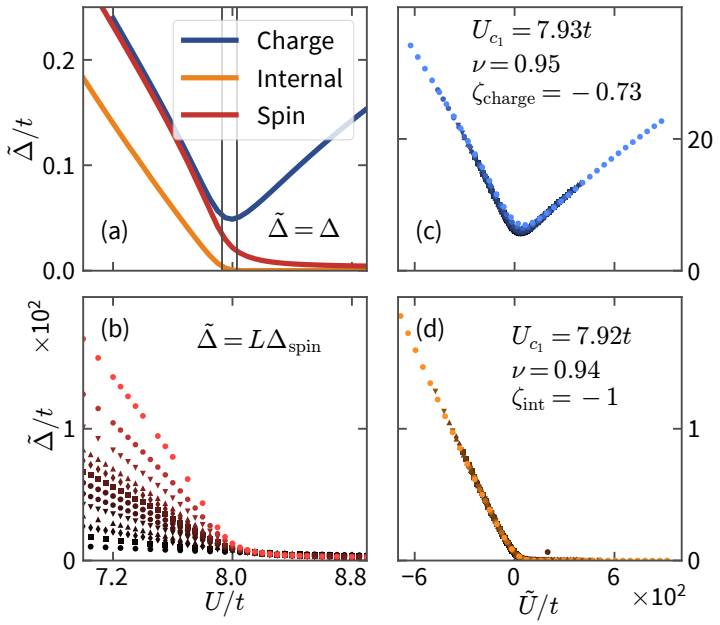

Figure 3.10: *Gaps at the phase transitions for $\delta = \pi/3$.* All data were computed with open boundaries. (a) Finite-size gaps Δ vs interaction strength U for $L = 600$. (b) Spin gap, divided by chain length L such that the data should collapse above the BKT transition. (c), (d) Rescaled data for (c) charge and (d) internal gap computed for $L \in \{30, 60, 90, 120, 150, 180, 210, 240, 270, 300, 360, 450, 600\}$, colored from dark to bright. In (c) and (d), we present a scaling collapse using $\tilde{U} = L^{1/\nu}(U - U_c)$ and $\tilde{\Delta} = L^{-\zeta/\nu}\Delta$ with different parameters ν, ζ and U_c estimated from the finite-size data.

We show finite-size data in fig. 3.10 (a) for all three gaps defined in eqs. (2.12), (2.13) and (2.15). Data were obtained with open boundary conditions and $L = 600$ for superlattice phase $\delta = \pi/3$. The charge gap exhibits a minimum at $U/t \approx 8$ while spin and internal gap decrease monotonously with U. This behavior is suggestive of a vanishing spin gap at large U/t and a zero of the internal gap at a lower critical value of U, which we will further substantiate below. The fact that the internal gap becomes very small for $U/t \gtrsim 8$ is due to degenerate edge modes.

Quantitatively, we determine exponents and critical values of the interaction strength for the first transition from a scaling collapse of the charge and internal gap in fig. 3.10 (c) and (d). We use the pyfssa package [197, 198] to estimate parameters to these scaling relations:

$$\tilde{U}_r = L^{1/\nu}(U - U_r)\,, \qquad \tilde{\Delta}_r = L^{-\zeta_r/\nu}\Delta_r\,. \tag{3.10}$$

Here, $r \in \{\text{int}, \text{charge}\}$ labels the gaps and the critical interaction, where $U_{\text{int}} = U_{\text{charge}} = U_{c_1}$. We find general agreement between the data for the excitation gaps shown in fig. 3.10 and the data for $\langle \hat{B} \rangle = 0$ shown in fig. 3.9 regarding the extent of the SDI phase.

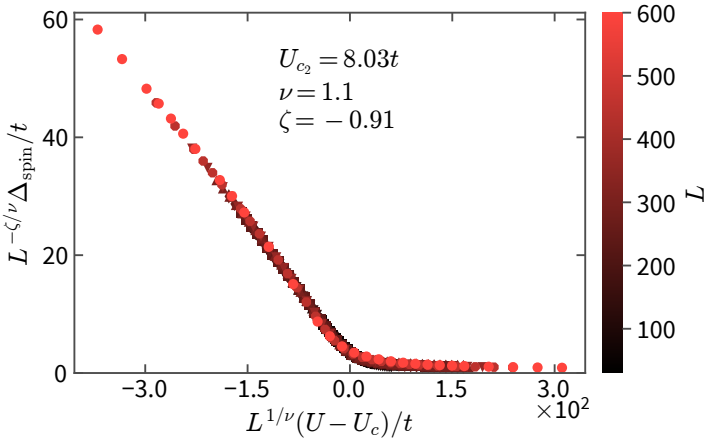

Figure 3.11: *Scaling collapse for the spin gap at $\delta = \pi/3$.* Data and colors are the same as for fig. 3.10 (b) and the parameters ν, ζ, U_{c_2} for the finite-size scaling collapse were determined numerically from eq. (3.10). The system sizes used in the scaling collapse are $L \in \{30, 60, 90, 120, 150, 180, 210, 240, 270, 300, 360, 450, 600\}$.

The scaling collapse of both gaps leads to the same value for critical interaction strength U_{c_1} related to the first transition and the exponent $\nu \approx 1$ matches an Ising transition (see, e.g., refs. [174, 181]).

The spin gap should scale according to the BKT universality class at the transition from SDI to CI and therefore, $L\Delta_{\mathrm{spin}}$ is expected to become independent of L at the phase transition. The data shown in fig. 3.10 (b) is consistent with a BKT transition at some $U_{c_2}/t \gtrsim 8$. We estimate the critical interaction strength U_{c_2} using a (conventional, non-BKT) scaling collapse shown in fig. 3.11 and obtain $U_{c_2}/t \approx 8.03$. Our system sizes are not large enough to reliably extract the critical value from a BKT scaling. Therefore, $U_{c_2}/t \approx 8.03$ has to be understood as a lower bound to the actual critical value.

Correlated insulator

Only for particular values of the superlattice phase $\delta \in \{1, 3, 5\} \times \pi/3$, we observe transitions to correlated insulating phases. For these values of δ, the model corresponds to the AB_2 ionic Hubbard chain [183]. This lattice configuration is sketched in fig. 3.2: Two lattice sites are energetically degenerate, while the third site is lower in energy. In an 'atomic picture' (i.e., $t \to 0$), for density $\rho = 2/3$, we would expect different states for small and large interaction strength U compared to the superlattice potential V: If U is weak, there are two particles localized in the site of the lowest energy. Strong repulsion $U \gg V$ prohibits double occupation, and therefore, there is only one particle in the potential minimum, while the other particle is delocalized over the remaining sites.

Assuming the atomic limit $t \ll V$, we can relate real-space and band occupations. When we choose a homogeneous gauge, total quasimomentum K is a conserved quantity for the noninteracting Hamiltonian eq. (3.1). Thus, we can express it in momentum

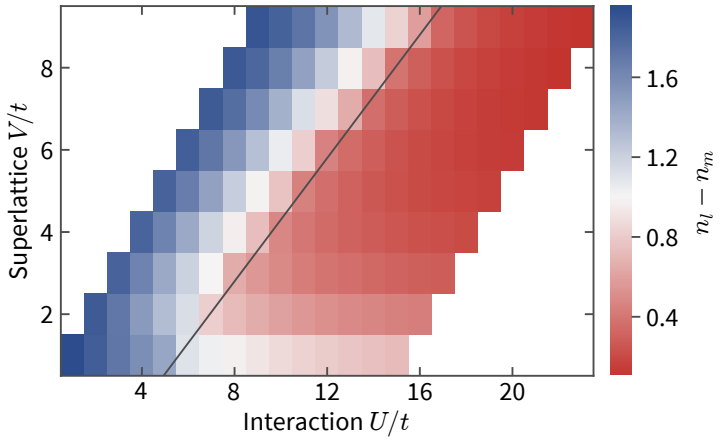

Figure 3.12: *Band occupation for $\rho = 2/3$.* We show the band insulator to correlated insulator transition with the lowest band filled, $\rho = 2/3$, for $\delta = \pi/3, \theta = 0$. For a given superlattice potential strength V, particles are transferred to the middle band as the interaction strength U increases. The occupation of the upper band remains small ($n_u \lesssim 0.1$) everywhere. The color bar encodes the difference of particle density in lower and middle band, i.e., $n_l - n_m = 0$ corresponds to equally filled bands. The gray, solid line indicates the topological phase transition where the Chern number changes, as shown in fig. 3.17. Calculations are performed for $L = 18$ and periodic boundary conditions.

space, using a vector of $q = 3$ creation operators $\hat{\boldsymbol{c}}^\dagger_{k,\sigma}$ for each spin σ and momentum k,

$$\hat{H} = \sum_{k,\sigma} \hat{\boldsymbol{c}}^\dagger_{k,\sigma} \begin{pmatrix} V\cos(\delta) & -t & -t\,\mathrm{e}^{i(k-3\theta/L)} \\ -t & V\cos\left(\frac{2\pi}{3}+\delta\right) & -t \\ -t\,\mathrm{e}^{-i(k-3\theta/L)} & -t & V\cos\left(\frac{4\pi}{3}+\delta\right) \end{pmatrix} \hat{\boldsymbol{c}}_{k,\sigma}\,, \tag{3.11}$$

This $q \times q$ matrix becomes diagonal for strong potentials $t/V \to 0$. In this limit, the states of each band are supported on only one lattice site in each superlattice cell. Therefore, we should expect that, given a strong potential V, the interaction does not only suppress double occupation in real space, but also in momentum space.

We show the density difference for the band occupation of the lower two bands for different U and V in fig. 3.12. For a sufficiently large potential strength $V/t \gtrsim 3$ our argument seems to hold and double occupation of bands is suppressed monotonically by increasing U/V. In the large U limit, we find that the two lowest bands are occupied evenly. This corresponds to the charge density of a spinless-fermion model with the same density. In the atomic limit, where $U, V \gg t$, we can estimate the location of the crossover to occur at $V = 3U/2$, where the double occupancy becomes energetically unfavorable for increasing U.

Strong coupling limit for $\rho = 2/3$

We can again study the spin sector in the strong-coupling limit by performing Schrieffer-Wolff perturbation theory, as in section 3.1.3 and section 3.2.2. For $\rho = 2/3$, we recover an effective spin chain of length $L_{\text{eff}} = L\rho = N$. This also implies that the effective spin model has a unit cell of two spins, which we label A and B. The spin physics is then governed by the effective Hamiltonian:

$$\hat{H}_S^{\text{eff}} = \sum_j \left[J\hat{\boldsymbol{S}}_{j,A} \cdot \hat{\boldsymbol{S}}_{j,B} + J'\hat{\boldsymbol{S}}_{j,B} \cdot \hat{\boldsymbol{S}}_{j+1,A} \right] . \tag{3.12}$$

Here, the $\hat{\mathbf{S}}_{j,A(B)}$ labels the $A(B)$ spin in the jth unit cell, and J and J' are the effective couplings derived from eq. (3.5) by averaging over the ground-state charge distribution. The intra- (J) and inter- (J') cell couplings are in general different. However, in certain symmetrical cases, which we discuss in more detail further on, the couplings can indeed become identical.

In the generic case of $J \neq J'$, this periodic variation in the spin coupling opens a gap and gives rise to a dimerized state in the spin-sector in the stron-coupling limit [196]. At the points $\delta \in \{\pi/3, \pi, 5\pi/3\}$, described by the ionic AB_2 Hubbard model [178], the system has a site-centered inversion symmetry resulting in $J = J'$ and the spin excitations again become gapless.

To help illustrate the nature of these states, we consider two specific cases of δ in the atomic limit $U \gg V \gg t$. For $\delta = 0$, the unit cell has two sites with energy $-3/4V$, coupled with inter-site tunneling t, and one site with onsite potential $+3/4V$. At density $\rho = 2/3$, the ground state has both lower sites occupied, and the energetically unfavorable site is unoccupied. This high-energy site can be adiabatically eliminated, resulting in an effective inter-cell tunneling $t' = 3t^2/2V$. The result is an intra-site spin coupling $J' = 4t^2/U$, and a much lower inter-cell coupling $J = \frac{9t^4}{UV^2}$. Thus, the spin-sector is gapped.

For $\delta = \pi/3$, the potential structure of the unit-cell is inverted, compared to the $\delta = 0$ case. This precise case has been studied in detail by Torio et al. [178]. Here, we have one occupied site with onsite potential $-3V/4$, and two sites with energy $+3V/4$ sharing a fermion. This state has an inversion symmetry around the lower occupied site. Combined with the lattice-translation symmetry, this implies:

$$J = J' \sim \frac{t^2 U}{U^2 - \left(\frac{3V}{2}\right)^2} . \tag{3.13}$$

Thus, at points where $\delta \in \{1, 3, 5\} \times \pi/3$, the spin-dimerization disappears and the spin sector becomes gapless [172].

The different phases in the strong- and weak-coupling limits can be understood in the context of symmetry-protected topological states. At the $\delta = \pi/3$ point, the model has a lattice-inversion symmetry around the first site in the unit cell. This lattice-inversion symmetry, combined with the $U(1)$ charge conservation, can give rise to a one-dimensional symmetry-protected topological phase. Such phases can be classified by

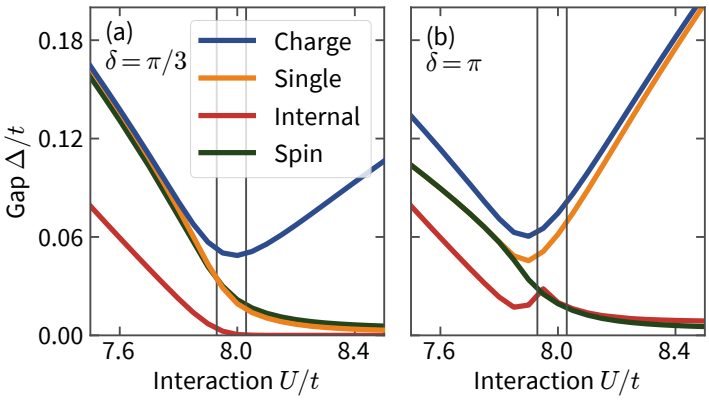

Figure 3.13: *Gaps at the phase transitions and inversion symmetry.* Data were computed for open boundaries at $L = 600$, and $\rho = 2/3$. We consider (a) $\delta = \pi/3$, which is inversion symmetric, and (b) $\delta = \pi$ which is not inversion symmetric. Edge states only exist for $\delta = \pi/3$, explaining the qualitatively different behavior of the single-particle gap in the large-U limit.

the many-body Zak phase φ (see eq. (3.3)), which can only take values of 0 and π when the inversion symmetry exists. We consider the atomic limit, where $U, V \gg t$: In this limit, when $U \ll V$, we have the lowest site occupied with a spin singlet. This state has $\varphi = 0$. Alternatively, in the $U \gg V$ limit, the lowest site is occupied with one fermion and one inter-site dimer occupied. This phase has $\varphi = \pi$. As these states are characterized by different values of a topological invariant (as long as the lattice-inversion symmetry is preserved), the many-body gap necessarily closes as the Hamiltonian is adiabatically transformed between the two limits.

In summary, for $U \gg t, V$, the $\rho = 2/3$ insulator has a gapped spin-dimerized ground state, except for the special, symmetric lines, where there is a gapless correlated-insulator phase.

Bulk and edge symmetry

As is well-known from DMRG studies [199], the particular choice of lattice termination can have important effects on the excitation spectrum. This is directly related to the presence of gapless edge modes in symmetry-protected topological states [200]. In our model, we have this situation in the $\rho = 2/3$ insulating phases, where the system has additional lattice symmetries along $\delta = 2\pi/6 + 2\pi n/3$.

When considering the three-site superlattice with open boundaries, a shift of the superlattice phase δ by $2\pi/3$ changes the properties of the edge: For the configuration sketched in fig. 3.2, a shift $\delta \to \delta + 2\pi/3$ removes the lattice-inversion symmetry, such that we have two energetically higher sites on one end. This explains why the discontinuities in fig. 3.15, related to edge states, do not have the same symmetry as the bulk.

Computing the single-particle gap, cf. section 2.2.1, we observe in fig. 3.13 that the degenerate edge states only appear for a 'symmetric' choice of boundaries. We observe in

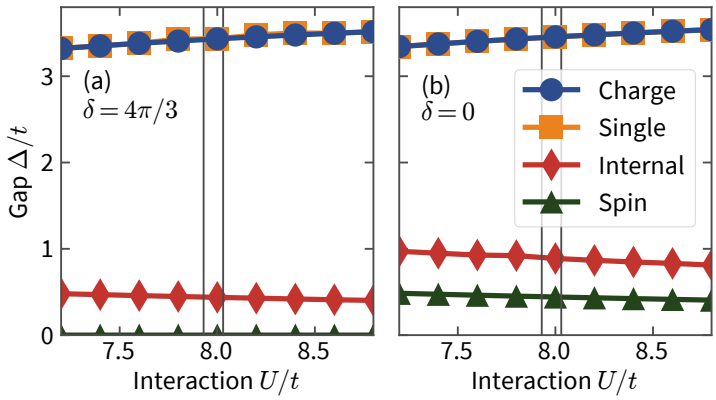

Figure 3.14: *Gaps at other values of δ.* Data were computed for open boundaries at $L = 600$ and $\rho = 2/3$, corresponding to fig. 3.13, however, the superlattice is shifted via $\delta \to \delta + \pi$ corresponding to $V \to -V$. We consider (a) $\delta = 4\pi/3$, which is inversion symmetric and (b) $\delta = 0$ which is not inversion symmetric. The inversion-symmetric lattice hosts a gapless spin mode at the boundaries, leading to the vanishing spin gap.

the same plot how the spontaneously dimerized phase (SDI) is prohibited by asymmetric boundaries: Only one dimerization is allowed and thus the internal energy gap has a local maximum for $U/t \approx 7.9$, when long-range dimer order appears.

In fig. 3.14, we show the four gaps (charge, single-particle, spin and internal gap) as a function of U/t for $\delta = 0$ and $4\pi/3$. At these values, there is no gap closing as U/t increases (compare fig. 3.6). We observe that the charge and single-particle gap are identical for the values of U/t considered in the figure. The spin gap is the smallest gap in both cases, while the internal gap exhibits a weak decrease with U/t. For $\delta = 4\pi/3$, which is inversion symmetric, there exist spin-edge modes and therefore, the spin gap vanishes. For systems with open boundary conditions, the band insulator has gapless edge states at $\delta = 4\pi/3$. The location of these edge states smoothly changes with increasing U.

3.3 Topological properties

The family $\{\hat{H}(\delta,\theta)\}_{\mathbb{T}^2}$ of 1D models in eq. (3.1) inherits topological properties from the 2D Harper-Hofstadter model for $U = 0$: At density $\rho \in \{2, 4\}/3$, the filled Hofstadter bands (see fig. 3.3) are topologically nontrivial. Thus, a quantized amount of charge is pumped during a cycle $\delta \to \delta + 2\pi$ in the infinite 1D model, cf. eq. (3.1).

When we include interactions and the ground-state manifold remains gapped, we can compute Chern numbers as described in section 2.2.3. In this section we study topological properties of the interacting insulating phases discussed previously.

In addition to the many-body Berry curvature, we also compute the center-of-mass coordinate $\overline{X}(\delta)$ for open boundary conditions. It can easily be evaluated using DMRG, and has also been measured in experiments [58, 59]. The definition of $\overline{X}(\delta)$ is:

$$\overline{X}(\delta) = \frac{1}{L}\sum_x x \,\langle\psi(\delta)|\,\hat{n}_x\,|\psi(\delta)\rangle \ . \tag{3.14}$$

Here, $|\psi(\delta)\rangle$ is the ground state at a given δ. Note that flux θ is merely a static gauge transformation for open boundaries, and thus does not matter here. As we compute ground states for each value of δ independently, there is no accumulation of charge at either end during a pump cycle: The center-of-mass coordinate returns to its initial value as $\delta \to \delta + 2\pi$. Instead, quantized charge transport can be observed as discontinuities of the center-of-mass coordinate. These discontinuities correspond to the shift of an occupied edge mode from one side of the system to the other [201].

As the Chern numbers are computed for a finite L with periodic boundary conditions there are some subtle points we must address. Firstly, for finite systems there are no gapless excitations in any insulating phase. We can therefore compute Chern numbers from unique ground states. However, spin excitation gaps in some Mott-insulating, and correlated-insulating phases close as $L \to \infty$. Therefore, the meaning of the Chern number in this limit, or equivalently, the stability of charge transport quantization in the related charge pump, is not guaranteed. We discuss this issue in more detail in section 3.3.4.

3.3.1 Mott insulator at density $\rho = 1/3$

At density $\rho = 1/3$, the lowest band is half-filled. As discussed in section 3.2.2, adding onsite interactions opens a charge gap for all δ, θ, and the phase becomes insulating. While this insulator has gapless spin excitations for $L \to \infty$, the ground-state manifold for finite systems is gapped already for $0 < U \ll t$. Thus, we compute Chern numbers for this phase as described in section 2.2.3.

For all systems sizes $12 \leq L \leq 42$ considered here we find a Chern number $C(\rho = 1/3, U > 0) = -1 = C_l$, which is equal to the Chern number C_l of the lowest band of the noninteracting Hofstadter model. We motivated this finding in section 3.2.2: Single-particle observables in the strongly-interacting phase approach the expectation values for spinless, free fermions in the charge sector. Therefore, we might expect to find the Chern number for a single species of free fermions, which would fill the lowest band, $C(\rho = 1/3) = C_l$.

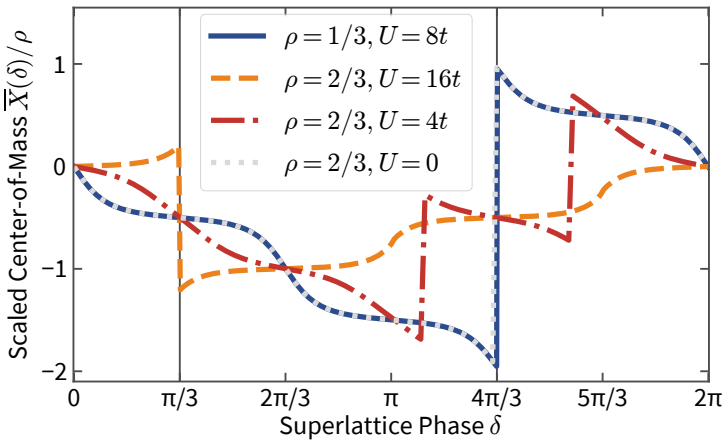

Figure 3.15: *Center-of-mass motion.* Scaled center of mass of an open system as a function of superlattice phase δ. For every cycle $\delta \to \delta + 2\pi$, there are discontinuities corresponding to -1 times the Chern number of the respective phase. The center-of-mass coordinate $\overline{X}$ [see eq. (3.14)] is divided by particle density ρ to show that the results for the Mott-insulating phase at $\rho = 1/3$ agree with the behavior of the noninteracting phase for $\rho = 2/3$. Data are obtained for length $L = 60$.

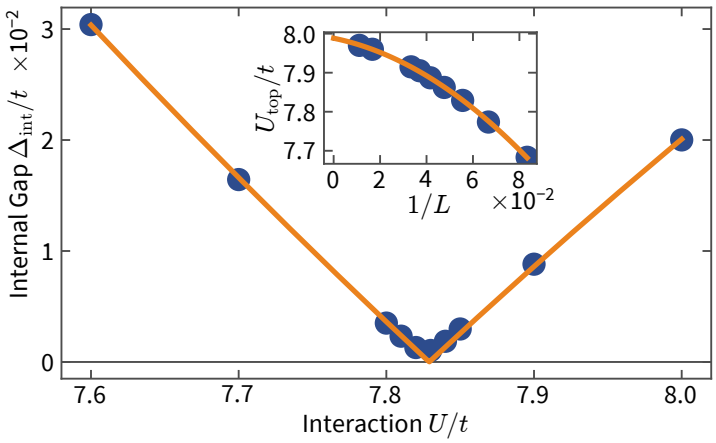

Figure 3.16: *Internal gap for the topological transition.* The Chern number of the ground-state manifold can only change when the many-body gap closes. Data are shown for density $\rho = 2/3$ and parameters $\delta = \pi/3,\ \theta = 0$, computed for length $L = 18$, and periodic boundary conditions. The line a fit using the absolute value of a second order polynomial. Inset: Critical interaction strength U_{top} extrapolated to infinite system size using a quadratic fit in $1/L$.

We also compute the center-of-mass coordinate $\overline{X}$ in the strongly interacting regime as a function of δ, shown in fig. 3.15. We observe a single jump of the center-of-mass coordinate eq. (3.14) by the negative value of the Chern number (solid line in the figure). The discontinuity is located at $\delta = 4\pi/3$, when the two 'lower' sites in the superlattice potential are energetically degenerate, see fig. 3.2.

Note that this center-of-mass curve perfectly lies on top of the one for the free model ($U = 0$) at density $\rho = 2/3$. This illustrates that the charge degrees of freedom in the strongly interacting phase behave much like a single component, free fermi gas, underlining our analogy with spinless fermions.

3.3.2 Topological transition at density $\rho = 2/3$

At density $\rho = 2/3$, we find that there are (at least) two different topological families, depending on the strength of the interaction U. In section 3.2.3, we saw that at density $\rho = 2/3$ there are a number of phases in the $\{\delta, U\}$ parameter space. We find that the first of these phase transitions closely coincides with a topological transition in the Chern number. This transition occurs when the many-body gap closes in the $\{\delta, \theta\}$ manifold, at a critical $U = U_{\text{top}}$, which, in general, is dependent on the system size, but should converge to U_{c_1} in the $L \to \infty$ limit [178]. Since the SDI phase is very narrow for our choice of parameters, we do not make any statement about the Chern number in the parameter regime that includes the SDI phase.

Weak interactions at density $\rho = 2/3$

Without interactions, the system is a band insulator that corresponds exactly to the ground state of the Harper-Hofstadter model with the lowest band filled. Thus, the Chern number for density $\rho = 2/3$ is given by two times the Chern number of the lowest Hofstadter band, $C(\rho = 2/3) = -2$. When we vary both interaction and superlattice potential strength, we consistently find a Chern number $C(\rho = 2/3, U < U_{\text{top}}) = -2$.

We find that for a finite lattice with periodic boundaries, the many-body gap closes only at one critical interaction strength U_{top}, and only at three points on the $\{\delta, \theta\}$ manifold: $\delta \in \{1, 3, 5\}\pi/3$, $\theta = 0$, as shown for $\delta = \pi/3$ in fig. 3.16. In the thermodynamic limit, we expect this transition to occur when the system undergoes a phase transition to the SDI phase at U_{c_1}.

The center-of-mass coordinate for the weakly-interacting system during the pump cycle is shown in fig. 3.15 (dot-dashed line). The amplitude of the discontinuities agrees with the negative Chern number, i.e., $-C = 2$. The values of δ where the jumps occur are not directly related to the symmetry of the lattice, but also depend on the interaction strength U.

Strong interactions at density $\rho = 2/3$

For strong interactions, $U > U_{\text{top}}$, the internal gap reopens for the entire ground-state manifold of $\{\hat{H}(\delta, \theta)\}_{\mathbb{T}^2}$ for finite system lengths (see fig. 3.16). As shown in fig. 3.17, we consistently find $C = +1$ in the presence of strong interactions. However, the global many-body gap closes at certain points due to the existence of gapless spin excitations.

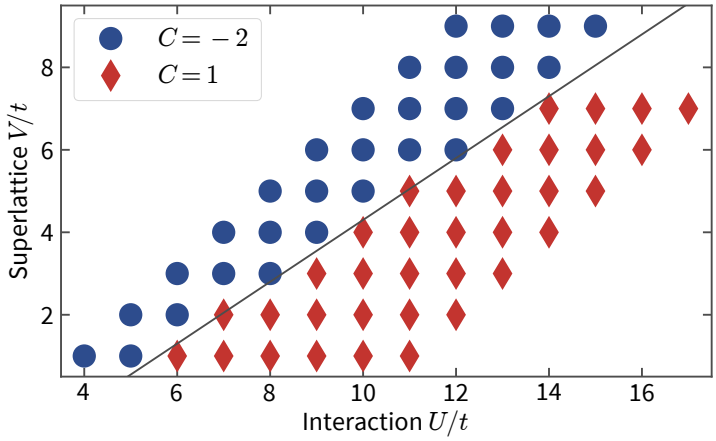

Figure 3.17: *Topological transition for* $\rho = 2/3$. The Chern number changes from $C(U < U_{\text{top}}) = -2 \to C(U > U_{\text{top}}) = 1$ for the insulators at density $\rho = 2/3$. Data are shown for length $L = 18$ with twisted boundary conditions. The solid line is a fit to the transition $V = V_{\text{top}}(U_{\text{top}})$.

Considering the center-of-mass coordinate for one cycle $\delta \to \delta + 2\pi$ in an open chain, we find that strong interactions change sign and amplitude of the jumps in fig. 3.15. For strong interactions $U/t = 16$ (dashed line in the figure), the discontinuity always occurs at $\delta = \pi/3$, the point of lattice-inversion symmetry, see section 3.1.2. Thus, the quantization of the pump cycle directly corresponds to the edge states of the SPT phase of the 1D chain at $\delta = \pi/3$.

Similar to the charge pump at density $\rho = 1/3$ discussed in subsection 3.3.1, we can understand the change of the Chern number from band occupations. We found in section 3.2.3 that interactions suppress double occupation of lattice sites as well as double occupation of bands. Expectation values of single-particle observables in the limit $U \gg V \gg t$ thus approach the values for spinless fermions. Indeed, for spinless fermions at density $\rho = 2/3$, we would expect the Chern number $C_l + C_m = -1 + 2 = 1$ which agrees with the numerically computed many-body Chern number.

Atomic limit

In fig. 3.17, we show a heuristically-determined line, which separates both topological phases. Here, we will show that the linear dependence does not hold for large $U, V \gg t$, and use the atomic limit to derive the correct slope.

Considering $\delta = \pi/3$, each superlattice unit cell consists of one site at potential $-V$ and two lattice sites at $V/2$. Thus, there are two possible ground-state configurations in the atomic limit, i.e., $t \to 0$, as sketched in fig. 3.2. We can simply compare their energies: The energy of the configuration with a single particle on the lowest-potential site, i.e., fig. 3.2 (b), is given by $E_{\text{single}} = -V/2 - t$. The competing state, i.e., fig. 3.2 (a), for weak interactions with a doubly occupied center site has energy $E_{\text{double}} = U - 2V$. Therefore, we expect the transition between both phases to occur when $E_{\text{single}} = E_{\text{double}}$, i.e., for $V_c = \frac{3}{2}U_c - t$.

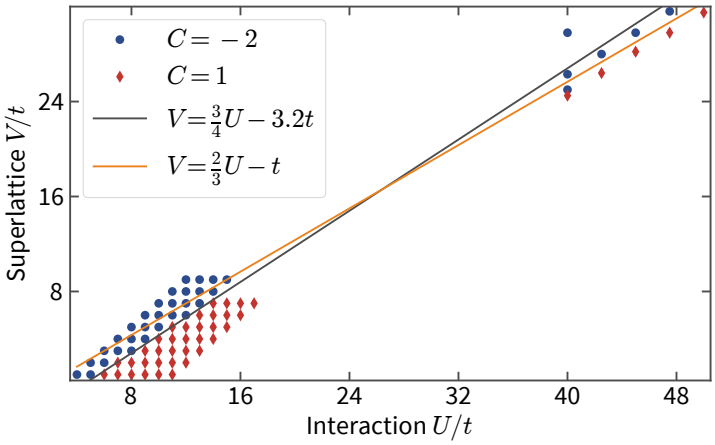

Figure 3.18: *Topological phase transition for $U, V \gg t$.* Numerical results shown in fig. 3.17 indicate a relation of critical parameters $V_c = \frac{3}{4}U_c - 3.2t$. Extending the parameter range, we find that $V_c(U_c \gg t)$ is actually smaller than this estimate: For $U_c > 40t$, the critical potential strength is rather given by $V_c = \frac{2}{3}U - t$, which we would expect in the atomic limit.

This estimate for the phase transition does not agree with data shown in fig. 3.17, where we have found $V_c = \frac{3}{4}U_c - 3.2t$. But the discrepancy is simply due to U and V being too small: As we consider superlattice strengths $V > 40t$ in fig. 3.18, we find that the approximation in the atomic limit seems to hold.

3.3.3 Interaction-induced degeneracies

The transition between the band- and correlated-insulating states at density $\rho = 2/3$ can be understood through certain interaction-induced degeneracies, as exemplified in fig. 3.16 for $\delta = \pi/3$.

The degeneracies exist as points in the two-dimensional $\{U, \delta\}$ parameter space, which has the topology of a cylinder. The situation is illustrated in fig. 3.19 (a). The entire $\{U, \delta\}$ parameter space is simply connected through adiabatic transport. However, it is not possible to deform the entire closed path with $C_{\mathrm{BI}} = -2$ (in the band-insulating region) into the $C_{\mathrm{CI}} = 1$ path (in the correlated region), as this would require crossing the degeneracies.

Each of these degeneracy points has a Chern number $C_d = -1$ associated with it, corresponding to the path encircling the point in the $\{U, \delta\}$ parameter space, as shown in fig. 3.19 (a). A pump cycle which encircles one of these points will transport a quantized charge of -1. This can be seen directly from the change in the center-of-mass value as one moves along this path in fig. 3.19 (a).

Finally, consider three paths each encircling one of these points in counter-clockwise direction, as shown in fig. 3.19 (b). These three paths can be composed to produce two paths, one for the band-insulating path, and one for the correlated-insulator path, but in the direction of $-\delta$. The Chern number of the band insulator at this density is

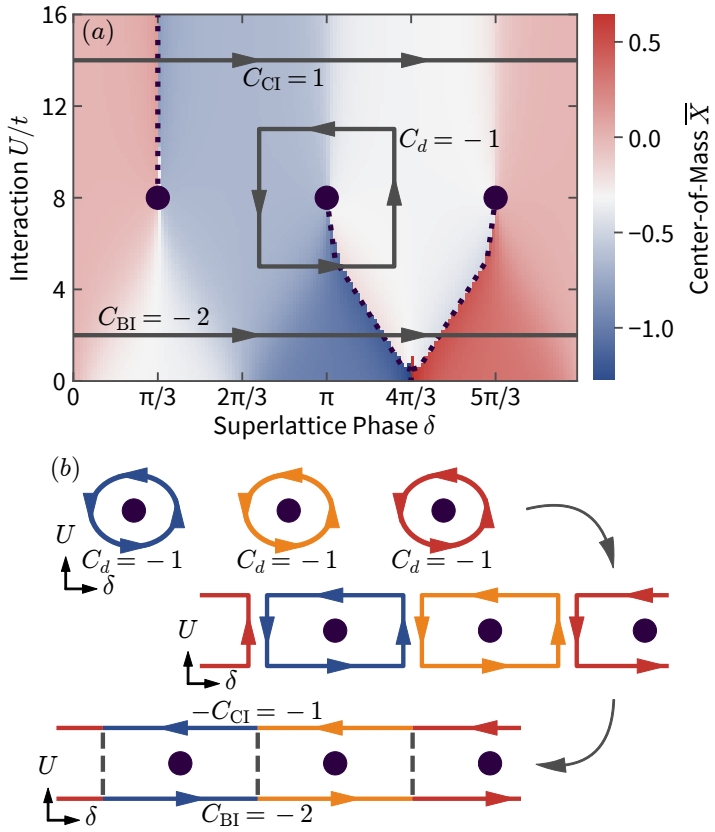

Figure 3.19: *Center-of-mass coordinate and topological structure for paths in the* $\{U, \delta\}$ *parameter space at* $\rho = 2/3$. (a) Quantized charge transport corresponds to discontinuities of $\overline{X}$ when computed from ground states with open boundary conditions. The purple circles at $\delta \in \{1, 3, 5\} \times \pi/3$ and $U = U_{\mathrm{top}} \approx 8t$ symbolize three topologically protected degeneracies in the case of $V/t = 3$. Any path encircling counterclockwise exactly one of these degeneracies has a Chern number $C_d = -1$, as it crosses exactly one jump changing $\overline{X}$ by $+1$ (indicated by the dotted lines). Data are obtained for $L = 60$ and open boundary conditions. (b) Three paths encircling one degeneracy each can be deformed and composed to form two separate paths: The $U < U_{\mathrm{top}}$ path and the $U > U_{\mathrm{top}}$ path. As this is a smooth deformation, the sum of all Chern number cannot change, and the difference in Chern numbers between the two paths must be $3 \times C_d = -3$.

$C_{\mathrm{BI}} = -2$, and we found $C_{\mathrm{CI}} = 1$ for the path in the large U/t phase that includes the CI phases. This implies that $C_{\mathrm{BI}} - C_{\mathrm{CI}} = 3C_d$, which is indeed the case.

3.3.4 Chern numbers on gapless systems

We must also address the question of the Chern number in the thermodynamic limit. For finite systems, there are no gapless spin excitations in any insulating phase, such that the Chern numbers computed in the previous sections are well-defined. However, in the case of Mott and correlated insulators, the spin excitations can become gapless as $L \to \infty$ (see the discussion in section 3.1.3, and section 3.2.3). This raises the question of the validity of such a topological classification in the thermodynamic limit: Do the gapless spin excitations preclude the possibility of adiabatic charge transport, or does the charge gap allow for quantized charge transport?

For the $\rho = 1/3$ Mott insulator, the system does not pass through any phase boundaries. This would suggest that adiabatic charge transport is well defined in this phase and remains quantized, reflecting the topology described in section 3.3.1.

For the $\rho = 2/3$ path in the strongly interacting regime, the system is gapped everywhere, except at the three points at $\delta \in \{\pi/3, \pi, 5\pi/3\}$ where there is a correlated insulator without spin-charge separation [178]. This state is also associated with a (weakly) divergent electric susceptibility [174, 181] which would suggest a possible breakdown of adiabatic transport when taking the system along this path. As our present results do not provide further insight into these issues we leave them for future work.

Next, we consider the consequence of these issues on the practical question of experimental observations. It is expected that the topological properties of our model will manifest themselves in a quantized charge transport for ultracold atoms in an optical lattice acting as a charge pump. This has been recently demonstrated in the case of bosons [58] and fermions [59]. In both these cases, the experiment was conducted with spinless particles, in a completely gapped phase. So far, there have been no such experiments with strongly-interacting systems. In these experiments, the charge transported was only approximately quantized, due to several factors: Finite-size effects, non adiabaticity from finite pump time, technical heating and the presence of an harmonic trap. As such, it is not clear that the fluctuations due to the spin degree of freedom would be discernible, particularly for very strong interactions, where the prefactor of the electric susceptibility is expected to be very small [174]. Moreover, quantum-gas experiments work with finite particle numbers of typically $N \sim 100$ atoms or less per one-dimensional system, and charge pumps are performed only for a limited number of cycles [58, 100]. Therefore, we expect that an experiment could show the predicted transition at $\rho = 2/3$ from $C = -2$ to $C = 1$ during the accessible first pump cycles.

We note that the optical superlattices considered in these cold-atom experiments induce modulated tunneling terms, in addition to the staggered potential considered in this chapter. For the Rice-Mele model, such modulated tunneling is necessary to open a gap at the inversion-symmetric points of the potential phase δ. In our case, the system is already gapped at these points, and the additional modulated tunneling is expected to only increase the size of gaps in the system. While the altered tunneling will change the

quantitative predictions of this chapter, for moderate modulations we suspect that this will not lead to a qualitatively different phase structure or topology to the one presented here.

3.4 Summary

In this chapter, we studied a one-dimensional fermionic lattice model with a superlattice potential and onsite repulsion. For a family of these systems defined on a torus of parameters, we can define a topological invariant. In the limit of large system sizes we can also interpret such families as topological charge pumps. Without interactions, the family of Hamiltonians maps directly to the 2D Harper-Hofstadter model and thus is in the same topological class.

A particularly interesting situation arises at certain values of the superlattice phase, where, as a function of U/t, a series of transitions exists, from a band insulator to a spontaneously-dimerized insulator to a correlated insulator. Theory and previous works [174, 178, 181] predict that these transitions are Ising and BKT, respectively, which is consistent with our numerical data. We argue that the first transition leads to a degeneracy in the full two-dimensional parameter space and a change of the Chern number from $C = -2$ to $C = 1$. The SDI phase is too narrow for the parameters considered here, and hence we don't make a statement about the Chern number there. This change of the Chern number can be understood from simple intuitive arguments in the atomic limit resulting from a competition of the superlattice potential strength V with the interaction strength U. The change of the Chern number is clearly seen in our finite-size data, and we expect that this U-driven transition should be detectable in a charge-pumping experiment. Different from the fermionic Rice-Mele model [157], we do not observe a breakdown of the charge pump when studying the same quantities as in [157] on finite system sizes. The presence of gapless spin excitations along special points of the pump cycle parameterized by δ may ultimately spoil the quantization of C at large U/t, but we expect that for the first pump cycles that can typically be accessed in a quantum-gas experiment the pumped charge should remain quantized. The clarification of this question, theoretically related to the degree of spin-charge separation, and its investigation in time-dependent simulations, including trapping potentials etc., is left for future research.

Alternatively, it might be possible to realize the same topological phases in a single 2D lattice, by substituting back $\delta \to k_y$. In this setting, one would get rid of the adiabatic pump cycle, and measure the topological invariant as a quantized susceptibility, i.e., the Hall conductivity. The next chapter will study this case, and discuss whether the quantization is robust under changes of the interaction terms.

4 2D interacting quantum Hall systems

In noninteracting models, spatial dimensionality is a question of interpretation. As discussed in section 1.5.2, we may formally treat the quasimomentum like any other parameter of the Hamiltonian. Therefore, the topological properties of infinite 2D lattices can be related to those of a one-parameter family of infinite 1D models [55], or to those of a two-parameter family of finite 1D lattices [112].

This analogy is at the basis of our numerical studies of the 1D charge pump in the previous chapter 3. We found that the inclusion of Hubbard interactions can change their topological properties: Without interactions, the Chern number of the family of pump models is $C = 2$, but strong repulsion changes it to $C = -1$. Note that we adapted the sign convention for C compared to chapter 3 such that it matches our choice in section 1.5.

We found in section 3.3.2 that the topological transition is related to a series of two 1D quantum phase transitions, which occur for certain values of the pump parameter. For these configurations, the 1D charge pump corresponds to the three-site ionic Hubbard model [165, 166, 168–175, 178, 183]. The interaction-driven change of topological properties in charge pumps with either fermions or bosons has also been studied in related, earlier papers [155, 157, 158].

The analytic one-to-one correspondence of charge pumps and 2D quantum Hall models breaks down when real-space interactions are introduced. In this chapter, we study numerically whether 1D charge pumps and 2D quantum Hall models with Hubbard interactions are adiabatically connected. In particular, we try to find a phase with Chern number $C = -1$ in the Hubbard-Hofstadter model, which is adiabatically connected to the $C = -1$ interacting charge pump. Most of the results discussed here have been published in ref. [2].

In order to connect 1D and 2D physics, we express the model in a mixed real- and momentum-space representation, called hybrid space [144, 146]. In hybrid space, we can tune the interactions in such a way that the 1D Hubbard charge pump and the 2D Hubbard-Hofstadter model become the limiting cases.

We compute the Hall conductivity by measuring persistent currents as a response to an adiabatically applied linear potential. We observe a finite Hall conductivity in insulating phases, which converges to integer values as we increase system size. We identify topological phases with two non-zero Chern numbers.

Several experiments with ultracold atoms and artificial gauge fields have already measured the response to an external, linear potential [35, 39–41]. There are different theoretical proposals to measure Chern numbers in such setups using bosonic wave packets [48, 202–204] or fermionic systems [205] under the action of a constant force. More recently, there are also proposals to measure fractionally quantized Hall drifts in setups inspired by ultracold-atom experiments [206, 207]. A method for measuring non-quantized Hall responses in interacting lattice models that is similar to ours has recently been proposed [208].

We find that the $C = -1$ phase exists in large regions in our space of interaction parameters. However, our results suggest that the Hofstadter-Hubbard model remains adiabatically connected to the band-insulating phase with a Chern number $C = 2$, even for large interactions. Thus, the 1D and 2D limits would be separated by a topological transition. Most results are obtained in the narrow-cylinder limit of width $W = 2$. We discuss the existence of the strongly interacting $C = -1$ phase for wider systems, up to $W = 6$.

Finally, we discuss the appearance of a ferromagnetic (FM) ground state for some interaction parameters inside the $C = -1$ phase. The FM phase exists for all system sizes we consider, but does not extend to the 2D or 1D limit. An FM state has the Chern number $C = -1$ since the system is then equivalent to free spinless fermions.

This chapter is structured in the following way: In section 4.1, we discuss the hybrid-space Hofstadter model with Hubbard interactions and its relation to the Hubbard-Harper model studied in chapter 3. Section 4.2 discusses the Hall conductivity depending on interaction parameters of the model. We reproduce the topological transition of the 1D charge pump in section 4.2.1, and study the extended parameter space in the numerically accessible regime of a small system width in section 4.2.2. In section 4.2.3, we show that both topological phases persist for wider systems. In section 4.3, we discuss the ferromagnetic ground state, which exists for some interaction parameters. Extending our analysis published in ref. [2], we show in section 4.4 that both the topological properties and the ferromagnetic ground state also exist in the isotropic model. We conclude with a summary in section 4.5.

4.1 Fermi-Hofstadter-Hubbard model

The Hofstadter-Hubbard Hamiltonian for spinful fermions, $\sigma \in \{\downarrow, \uparrow\}$, on a cylinder of length L and circumference W can be written as,

$$\begin{aligned}\hat{H} = \sum_{x=1}^{L}\sum_{y=1}^{W}\Bigg[\sum_{\sigma}\Big(&- t_y\, \mathrm{e}^{2\pi i\alpha x - i\delta/W}\, \hat{c}^{\dagger}_{x,y,\sigma}\hat{c}_{x,y+1,\sigma} \\ &- t\hat{c}^{\dagger}_{x,y,\sigma}\hat{c}_{x+1,y,\sigma} + \mathrm{H.c.}\Big) + U\hat{n}_{x,y,\uparrow}\hat{n}_{x,y,\downarrow}\Bigg].\end{aligned} \tag{4.1}$$

The boundary conditions are implemented via $\hat{c}_{L+1,y,\sigma} \equiv 0$ and $\hat{c}_{x,W+1,\sigma} \equiv \hat{c}_{x,1,\sigma}$. The onsite Hubbard repulsion is of strength U. The model is sketched in fig. 4.1 (a). The hopping term along the ring includes a complex phase: A particle hopping around one plaquette gains a phase α, corresponding to a magnetic flux piercing. In this chapter, we stick to the case of $\alpha = 1/3$, i.e., one flux quantum per three lattice sites. We choose this value of the flux because 3 is the smallest integer denominator for which the Hofstadter model exhibits fully-gapped, topologically nontrivial bands [10]. There is also a flux δ piercing the cylinder along its height, which we interpret as an angle twisting the boundaries. Twist angles may be used to define many-body topological invariants [113]. We will average over δ to reduce the effects of a finite width W.

In this chapter, we only study the phases at fixed particle density $\rho = 2/3$, i.e., two spin-1/2 fermions per every three sites. For $\alpha = 1/3$, and in the free case $U = 0$, this

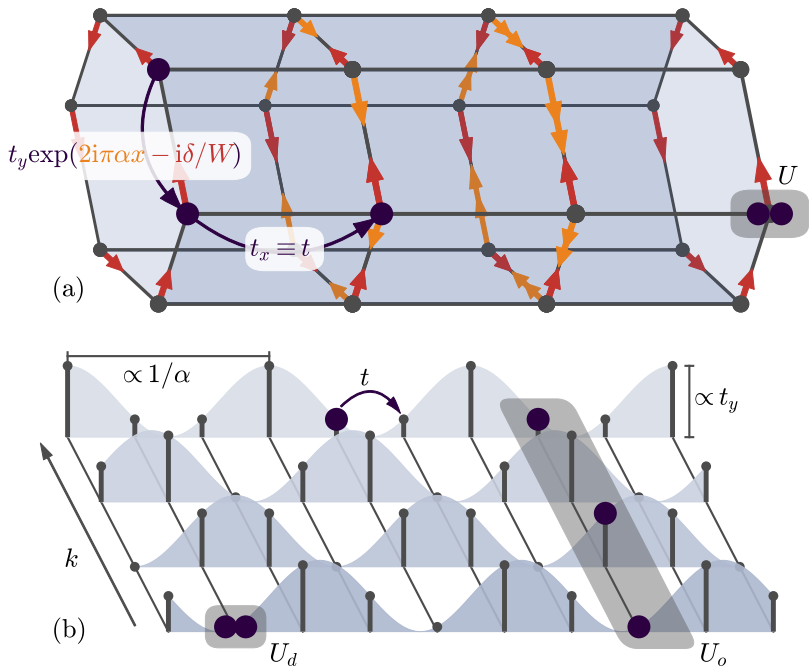

Figure 4.1: *Sketch of the Hofstadter-Hubbard model.* (a) Real-space representation on a cylindrical geometry, with a twist angle δ implemented via homogeneous, complex hopping rates along the y direction. The magnetic field is implemented via position-dependent complex phases, sketched here for flux $\alpha = 1/3$. The interaction is proportional to U, and is purely onsite. (b) Hybrid-space representation, obtained via a Fourier transformation along the axis with periodic boundary conditions (see also ref. [209]). The flux $\alpha = 1/3$ corresponds to a three-site periodic superlattice potential and its amplitude is shown in light blue. The interaction is now delocalized over each ring: We split the terms $\hat{H}_{\text{int}} = \hat{H}_{\text{int},o} + \hat{H}_{\text{int},d}$ according to eq. (4.3) into terms which are diagonal (onsite) in the hybrid-space basis, $\hat{H}_{\text{int},d}$, and the rest, which is off-diagonal (ring-wise) in hybrid space, $\hat{H}_{\text{int},o}$. The interaction terms have strengths U_d and U_o, respectively. The model sketched in (b) maps to (a) only when $U = U_d = U_o$. Note that the number of sites along each dimension is, of course, preserved when going from (a) $\rightarrow$ (b). A different number of sites was chosen in (a) and (b) for visualization purposes.

corresponds to a band insulator with Chern number $C = 2$, as the lowest band has $C_l = 1$ and is filled by both spin species. We choose anisotropic tunneling rates $t_y = 1.5t$ such that the parameters correspond to the charge pump considered in chapter 3.

4.1.1 Hybrid-space representation

By Fourier transforming eq. (4.1) along the periodic y-axis, we find a mixed real- and momentum-space representation, which we call hybrid space,

$$\hat{H} = \sum_{x,k,\sigma} \Big[-2t_y \cos(2\pi(\alpha x + k/W) - \delta/W)\hat{n}_{x,k,\sigma} - t\hat{c}^\dagger_{x,k,\sigma}\hat{c}_{x+1,k,\sigma} \Big] + \hat{H}_{\text{int}} \,. \tag{4.2}$$

The hybrid-space model is sketched in fig. 4.1 (b). Not taking $\hat{H}_{\text{int}}$ into account, eq. (4.2) can be understood as a set of uncoupled 1D chains, which are labeled by quasimomentum k. There is an additional cosinusoidal potential depending on k, i.e., a superlattice.

In hybrid space, the onsite Hubbard repulsion becomes delocalized over each ring,

$$\begin{aligned} \hat{H}_{\text{int}} &= \frac{U}{2} \sum_{x,y} \hat{\boldsymbol{c}}^\dagger_{x,y} \cdot \hat{\boldsymbol{c}}_{x,y} \left(\hat{\boldsymbol{c}}^\dagger_{x,y} \cdot \hat{\boldsymbol{c}}_{x,y} - 1 \right) \\ &= \frac{U}{2W} \sum_{x} \sum_{k,p,q} \left(\hat{\boldsymbol{c}}^\dagger_{x,k} \cdot \hat{\boldsymbol{c}}_{x,p} \right) \times \left(\hat{\boldsymbol{c}}^\dagger_{x,q} \cdot \hat{\boldsymbol{c}}_{x,k+q-p} \right) - \frac{U}{2} \sum_{x,k} \hat{n}_{x,k} \\ &=: U_d \hat{H}_{\text{int},d} + U_o \hat{H}_{\text{int},o} \,, \end{aligned} \tag{4.3}$$

where we use spinor operators, $\hat{\boldsymbol{c}} = (\hat{c}_\uparrow, \hat{c}_\downarrow)^T$ to simplify the notation, cf. section 2.2. In the last line, we split the interaction into two parts: $\hat{H}_{\text{int},d}$ contains contributions that are diagonal in the hybrid-space indices x, k. All remaining, (mostly) off-diagonal terms are grouped in $\hat{H}_{\text{int},o}$, which is delocalized over each ring. Note that terms proportional to the total particle number $\sum_{x,k} \hat{n}_{x,k}$ only shift the chemical potential and can be neglected when the particle number is fixed by the numerical method. Explicitly, the interaction terms take the following form,

$$\hat{H}_{\text{int},d} := \frac{1}{2W} \sum_{x,k} \hat{n}_{x,k}(\hat{n}_{x,k} - 1) \,, \tag{4.4}$$

$$\hat{H}_{\text{int},o} := \frac{1}{2W} \sum_{x,k} \left(\sum_{p,q} [1 - \delta_{k,p}\delta_{k,q}] \left(\hat{\boldsymbol{c}}^\dagger_{x,k} \cdot \hat{\boldsymbol{c}}_{x,p} \right) \times \left(\hat{\boldsymbol{c}}^\dagger_{x,q} \cdot \hat{\boldsymbol{c}}_{x,k+q-p} \right) - [W-1]\, \hat{n}_{x,k} \right) . \tag{4.5}$$

The term $\hat{H}_{\text{int},d}$ looks like the normal Hubbard interaction, scaled by W^{-1}. This term thus corresponds to the 1D interactions in a charge pump as $U_d = W\, U_{\text{1D}}$.

The parameterization of eq. (4.4) allows us to relate 1D charge pumps with interactions ($U_o = 0$, $U_d > 0$) to the interacting 2D Hofstadter model ($U_d = U_o > 0$), as sketched in fig. 4.2. In this figure, these limiting cases are represented by the blue and orange lines. Note that while both $\hat{H}_{\text{int}} = \hat{H}_{\text{int},d} + \hat{H}_{\text{int},o}$ and $\hat{H}_{\text{int},d}$ are positive semidefinite, $\hat{H}_{\text{int},o}$ is

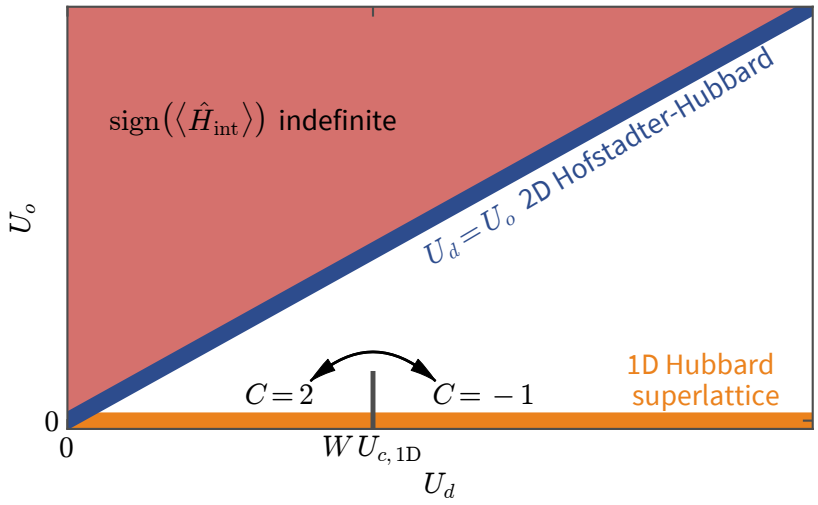

Figure 4.2: *Sketch of the parameter space created by splitting the interaction term according to eq. (4.3).* At $U_o = 0$, the interaction is onsite in the hybrid-space representation, such that the system consists of uncoupled Hubbard-Harper chains with a periodic potential. For the 1D model, there exists a critical interaction strength $U_{c,1\mathrm{D}}$, where the Chern number changes from $C = 2$ to $C = -1$, cf. section 3.3.2. Due to the prefactor in eq. (4.4), we obtain a factor of W for the critical value of U_d. When we fix $U = U_d = U_o$, we recover the original 2D Hubbard interaction. Note that both $\hat{H}_{\mathrm{int},d}$ and $\hat{H}_{\mathrm{int},d} + \hat{H}_{\mathrm{int},o}$ are positive semidefinite, however $\hat{H}_{\mathrm{int},o}$ is not. Therefore, the interaction can be attractive for $U_o > U_d$, which we do not consider.

not. Thus, for $U_o > U_d$, the interactions can become attractive, and we do not consider this case here.

As shown in fig. 4.2, there is a topological phase transition from Chern number $C = 2$ to $C = -1$ for $U_o = 0$ and a critical interaction strength $U_d = W\,U_{c,1\mathrm{D}}$, corresponding to uncoupled 1D superlattice chains, which we discussed in section 3.3.2. We expect weakly-interacting systems with parameters $U_d, U_o \ll W \times U_{c,1\mathrm{D}}$ to be adiabatically connected to the free model, and thus, to have Chern number $C = 2$.

For the strongly-interacting 1D charge pump with Chern number $C = -1$, both bulk and spin gaps vanish for certain values of the pump parameter, cf. section 3.2.3. This corresponds directly to the gap closing in the ionic Hubbard model [166, 174]. While the system remains insulating, i.e., the charge gap remains open, the topological quantization could, in principle, break down as perturbations are added. Here, we want to find out whether the $C = -1$ phase obtained in the strongly interacting 1D limit, $U_d > W\,U_{c,1\mathrm{D}}$, also exists with 2D interactions, $0 < U_o \leq U_d$.

4.1.2 Hall conductivity

In the first part of this section, we describe our setup for computing the Hall response, and define the observables. Then, we show how these measurements can be related to

topological quantization for simulations performed in finite-size systems.

We use a method to compute the Hall conductivity, which could very similarly be realized in experiments with cold atoms. In order to probe the Hall current, we add a weak ($V \ll t$) linear potential to the Hamiltonian. The potential is constant along the y (equivalently: k) direction and increases linearly along the x direction,

$$\hat{V} = V \sum_{x,k,\sigma} x\, \hat{n}_{x,k,\sigma} \,. \tag{4.6}$$

This corresponds to a constant electric field along the x-direction. We may then compute the current response to a weak field $\hat{V}$ as described in section 2.2.2. For the systems we study in this chapter, potential gradient strengths $0 \leq V \leq 10^{-3}t, \ldots, \times 10^{-2}t$ typically yield linear-response behavior.

The cylindrical geometry sketched in fig. 4.1 (a) allows for persistent ground-state currents along the rings. Taking the twist angle δ and anisotropic tunneling rates into account, we can express the intra-ring current as

$$\begin{aligned} \hat{j}_y(x) &:= \frac{it_y}{W} \sum_{y,\sigma} \mathrm{e}^{2\pi i\alpha x - i\delta/W}\, \hat{c}^\dagger_{x,y,\sigma} \hat{c}_{x,y+1,\sigma} + \mathrm{H.c.} \\ &= \frac{2t_y}{W} \sum_{k,\sigma} \sin(2\pi(\alpha x + k/W) - \delta/W) \hat{n}_{x,k,\sigma} \,. \end{aligned} \tag{4.7}$$

Note that in the hybrid-space representation, $\hat{j}_y$ is a sum of operators acting on a single site. This is related to the fact that the legs in the free hybrid-space Hamiltonian given in eq. (4.2) are not coupled. The Hall-current response to $V \neq 0$ is thus due to a polarization *along* the direction of the potential gradient, which depends on k and x. This is sketched in fig. 4.3: In response to a weak potential $\hat{V}$, which is switched on instantaneously, particles hop along the x direction in such a way that a Hall current $\langle \hat{j}_y \rangle$ as defined in eq. (4.7) is created. We choose a quench for fig. 4.3 because there are no currents along the x direction in the ground state of an open system. The relation of polarizability and Hall conductivity is also discussed in the context of hybrid Wannier orbitals [210] which is equivalent to our hybrid-space representation [98, 211].

We define the linear Hall response to a weak potential gradient as

$$\chi_{\mathrm{Hall}} := 2\pi\, \partial_V \left\langle \hat{j}_y(x) \right\rangle_{x \in \mathrm{bulk}} \Big|_{V \to 0} \,, \tag{4.8}$$

where we restrict the average to rings in the bulk of the cylinder. In most cases, we find it sufficient to ignore 3 or 6 (a multiple of q) rings on either end of the cylinder, in order to observe bulk behavior.

Quantized Hall response

The Hall response defined in eq. (4.8) can be computed in any interacting, finite-size system, but does not take integer values, which one would like to see for topologically quantized systems.

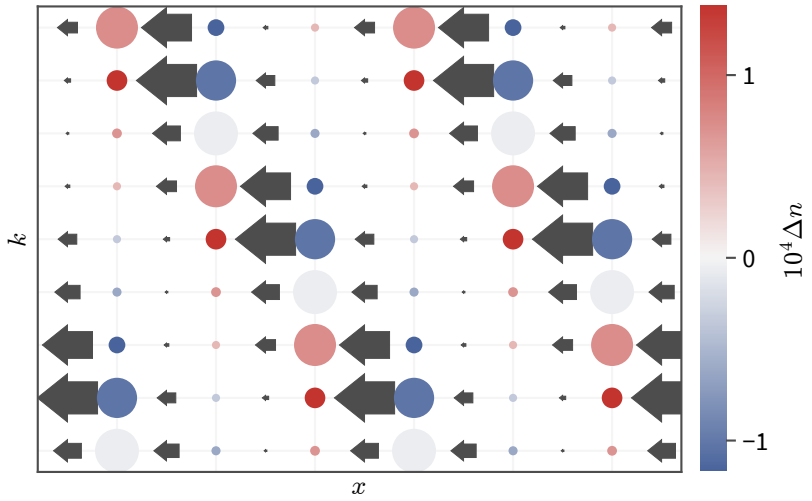

Figure 4.3: *Response to a potential gradient V in hybrid space.* We show the system at a short time $\tau\, t = 0.2$ after switching on a potential gradient of strength $V = 0.01t$: We use a time-dependent simulation for this illustration as there are no currents along the x direction in the ground state on a cylinder. Data are shown for the bulk of a noninteracting system of size $W = 9,\ L = 60$, with twist angle $\delta = 0.2\pi$. The size of an arrow indicates the amplitude of the particle current in the x direction, the size of the circles encodes the occupation number $\langle \hat{n}_{x,k} \rangle$ on a lattice site. Colors indicate the particle number difference compared to before the quench, $\Delta n = \langle \hat{n}(\tau) \rangle - \langle \hat{n}(0) \rangle$. Note that in the free model, the hybrid-space legs are uncoupled and the current $\langle \hat{j}_y(x,k) \rangle$ appears as a quasimomentum-dependent polarization along the x direction.

To define the Chern number for a finite, interacting model, one usually employs twisted boundaries for both spatial dimensions to define the Berry curvature on the parameter space of twist angles [113]. We have introduced the numerical approach by Fukui et al. [149] in section 2.2.3, and employed it to compute exactly integer-quantized Chern numbers from a finite number of finite-size ground states in section 3.3.

To recover the integer quantization of the linear Hall response χ_{Hall}, we need to average over the twist angle δ

$$\langle \chi_{\text{Hall}} \rangle_\delta = C \in \mathbb{Z}\,. \tag{4.9}$$

We show the dependence of the Hall response χ_{Hall} on the twist angle δ for different interaction strengths in fig. 4.4. The amplitude of χ_{Hall} depends strongly on δ for the narrow width $W = 3$ considered here. Computing the average over δ, we recover integer values for $\langle \chi_{\text{Hall}} \rangle_\delta$, up to a precision of 5×10^{-3}. This is consistent with the finite-size deviations of the free model, shown in fig. 1.6.

Compared to the method by Fukui et al. [149] to numerically integrate the Berry curvature, which we describe in section 2.2.3, the δ average does not give integer values *by*

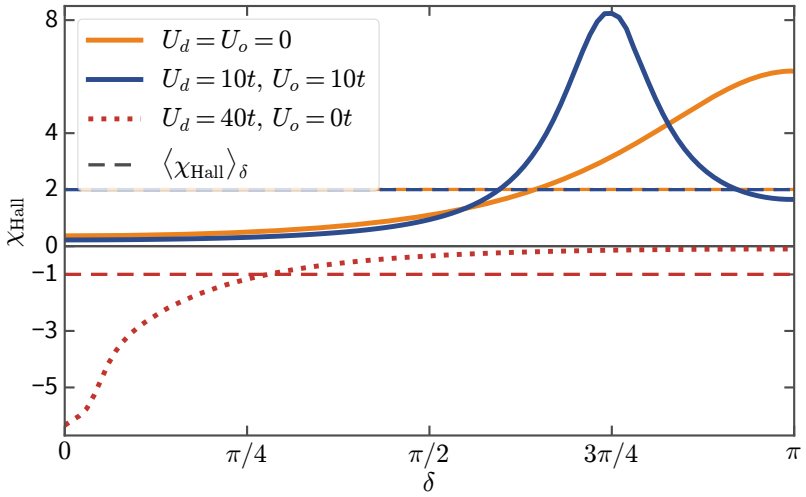

Figure 4.4: *Dependence of the Hall susceptibility on the twist angle δ.* Data are shown for a narrow cylinder of $W = 3$ and $L = 24$. χ_{Hall} is extracted from a linear fit to $\langle \hat{j}_y(V) \rangle$ as the potential V is applied adiabatically, cf. section 2.2.2. The Hall response χ_{Hall} depends strongly on the twist angle δ and interaction parameters. Only the δ average is integer quantized: The dashed lines indicate the corresponding averages, and take integer values up to finite-size effects, which are on the order of 10^{-3}. We observe that for each parameter combination of U_d and U_o, the response χ_{Hall} has the same sign for all values of δ.

design. Instead, we may converge to an integer as the number of samples and the system size increases. We expect this to happen if and only if the system is in a topologically nontrivial, insulating phase.

Response to a weak quench

In an experimental setup, it might not be realistic to prepare ground states for several strengths of the linear potential. Instead, it is probably easier to prepare the ground state for $V = 0$, and to measure the Hall current after switching on a weak field $V > 0$.

The Hall response to a quenched potential $V = 0.01t$ at time $\tau = 0$ in the free model is shown in fig. 4.5. We find that the Hall currents oscillate around the values we expect from the adiabatic calculations in fig. 4.4. I.e., the time-averaged Hall current takes the value $2\pi\overline{j_y}(\delta) = \chi_{\mathrm{Hall}}(\delta)V$. Therefore, twist-angle averaging is necessary in narrow systems.

In fig. 4.5 we find that the time evolution has to be performed over several inverse tunneling rates to find reliable results. This means that the time evolution will typically be numerically more expensive than the strictly adiabatic approach. More research would be needed for possible experimental implementations: An experiment in synthetic dimensions could realize the cylindric boundary conditions used here [42], and allow for persistent Hall currents. For a real-space setup with open boundaries, edge effects will surely become relevant on time scales $\tau\, t = \mathcal{O}(W)$.

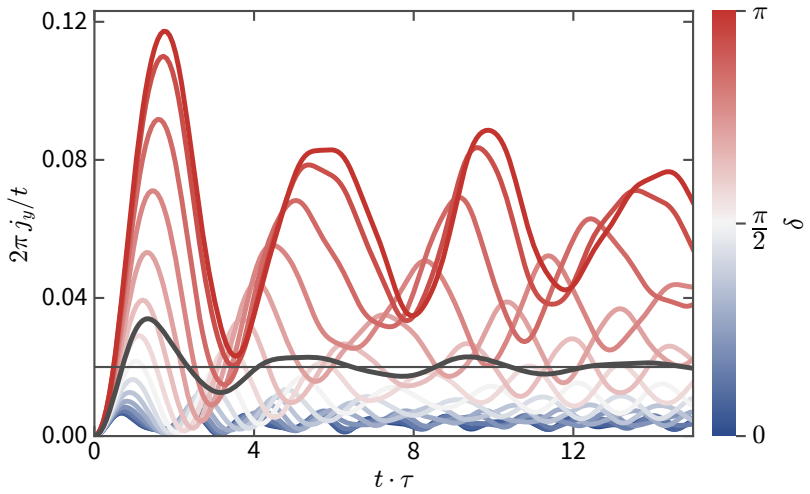

Figure 4.5: *Hall current j_y as response to a weak quench.* Data are shown for the free Hofstadter model of length $L = 60$ and width $W = 3$. The amplitude of the current j_y depends on the twist angle δ, as we expect from fig. 4.4, and the average (shown in gray) oscillates around $2\pi j_y = CV$.

4.2 Hall conductivity in the $S = 0$ ground state at $\rho = 2/3$

In this section, we study the adiabatic Hall response χ_{Hall} to a weak gradient, given in eq. (4.6), for different parameters of the model eq. (4.2). We restrict the DMRG ground-state search to the spin-singlet sector, $S = 0$.

This section is structured as follows: In section 4.2.1, we reproduce the 1D topological phase transition already discussed in section 3.3.2. Specifically, we run simulations for width $W > 1$, but fix the off-diagonal interaction strength to $U_o = 0$, and measure topological invariants via persistent Hall currents. In section 4.2.2, we extend the parameter space to $0 < U_o \leq U_d$, but restrict ourselves to width $W = 2$. Finally, in section 4.2.3, we present data for wider cylinders and $U_o > 0$, and discuss how critical interaction strengths scale with the width.

4.2.1 Quasi-1D limit $U_o = 0$

For $U_o = 0$, eq. (4.2) can be interpreted as a series of W uncoupled 1D superlattices with different superlattice phases δ. In this section, we verify that computing χ_{Hall} reproduces the topological transition of section 3.3.2. Unlike for chains, we do not keep particle numbers on each leg fixed individually, which could in principle yield a different behavior.

In fig. 4.6, the Hall conductivity for a cylinder of width $W = 2$ is shown for various interaction strengths U_d and twist angles δ. We find that the Hall conductivity depends both on the twist angle δ and the interaction strength U_d. The average $\langle \chi_{\text{Hall}} \rangle_\delta$, shown as dashed, black line, assumes the quantized values $C = 2$ ($C = -1$) for weak (strong)

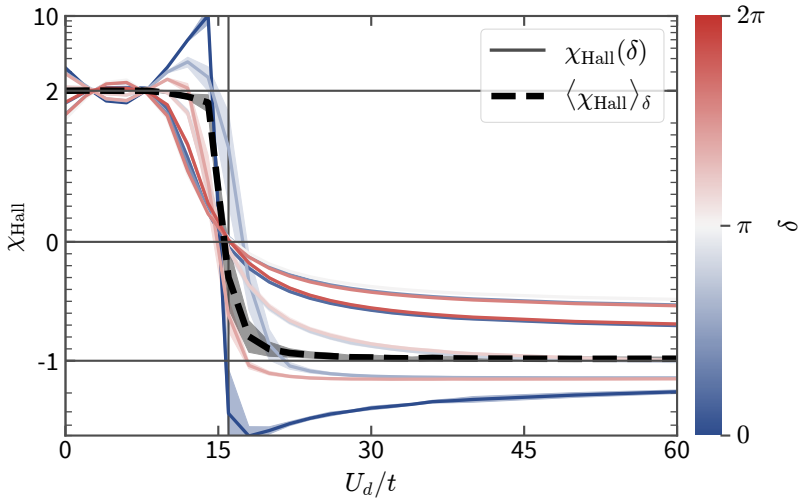

Figure 4.6: *Hall response for an adiabatically applied potential V for $W = 2$.* Data are shown without off-diagonal interaction terms, i.e., $U_o = 0$. Therefore, we expect to observe the topological transition known from 1D systems at $U_d \approx 8Wt$. The thin colored lines represent data for different twist angles $\delta \in \{0, 0.1, 0.2, 0.3, 0.4, 0.5, 0.6, 0.7, 0.8, 0.9, 1\} \times \pi$. The dashed, black line is the average over these δ values. Close to the 1D quantum phase transition for $\delta = 0$ at $U_d \approx 16t$, the conductivity diverges, such that an extrapolation in L is necessary, see fig. 4.8. The χ_{Hall} axis is logarithmic for $|\chi_{\mathrm{Hall}}| > 1$ in order to emphasize the values between $\chi_{\mathrm{Hall}} = C \in \{-1, 0, 2\}$.

interactions. We cannot resolve the topological transition accurately due to the short length of the simulated systems.

For most values of δ, the Hall response crosses $\chi_{\mathrm{Hall}}(U_d) = 0$ continuously at the topological transition. Even though the susceptibility is not quantized in a single, finite-size system, we can observe the change of sign and amplitude of χ_{Hall} associated with the topological transition from a single twist angle δ. The exception are values close to $\delta = 0$, for which χ_{Hall} diverges. We discuss this case in the next section.

We also show a plot for the Hall response in a wider cylinder, $W = 3$, in fig. 4.7. This width is commensurate with the magnetic unit cell at $\alpha = 1/3$. As expected, we observe the transition from $C = 2$ to $C = -1$ at $U_d \approx 8Wt$. We cannot resolve the behavior of χ_{Hall} at the phase transition for $\delta \approx 0$. For other values of δ, the error of χ_{Hall} is small, and the curves are smooth, even at the point where χ_{Hall} changes sign. In the quasi-1D case, the Hall response for systems of different widths can be related via

$$\chi_{\mathrm{Hall}}(2W, \delta, 2U_d, U_o = 0) = \left[\chi_{\mathrm{Hall}}(W, \delta, U_d, U_o = 0) + \chi_{\mathrm{Hall}}(W, \delta + \pi, U_d, U_o = 0)\right]/2\,. \quad (4.10)$$

We verified this relation numerically with simulations for width $W = 6$ (not shown).

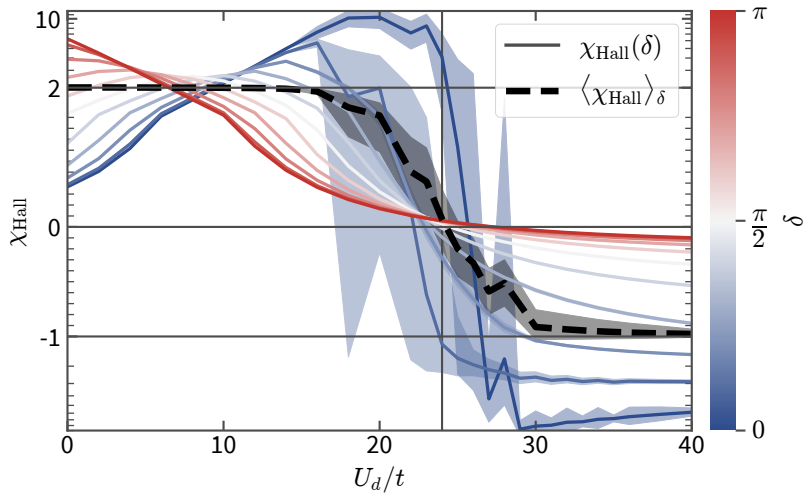

Figure 4.7: *Hall conductivity across the quasi-1D phase transition, when $U_o = 0$, for $W = 3$, $L = 24$.* The thin colored lines are data for different twist angles $\delta \in \{0, 0.1, 0.2, 0.3, 0.4, 0.5, 0.6, 0.7, 0.8, 0.9, 1\} \times \pi$. The dashed, black line is the average over these values of δ. Close to the 1D quantum phase transition for $\delta = 0$ at $U_d \approx 8t\,W$, the conductivity diverges such that an extrapolation in L is necessary, see fig. 4.8. The χ_{Hall} axis is logarithmic for $|\chi_{\text{Hall}}| > 1$, in order to suppress outliers for $\delta = 0$, and to focus on the topological transition.

Divergence at the phase transition

Without twist angle, $\delta = 0$,[1] and for $U_o = 0$, the $k = 0$ leg corresponds to the AB_2 ionic Hubbard model [168, 178, 183]. This 1D model exhibits two phase transitions as a function of the interaction strength, which we discussed in section 3.2.3: From a band insulator, to a spontaneously dimerized insulator, to a correlated insulator [166]. For the parameters chosen in here, we cannot resolve both transitions because the critical values of the interaction strength U_d are very close to each other and much longer systems would be required, cf. section 3.2.3, and refs. [171, 174, 181].

In the intermediate SDI phase, different dimer orientations create a two-fold ground-state degeneracy [166], see also fig. 3.8. For the ionic Hubbard model, this causes a diverging electric susceptibility [174, 181], due to the different center-of-mass (COM) positions of both dimer configurations. In the hybrid-space representation, the different COM positions along the x direction for fixed quasimomentum $k = 0$ correspond to different currents $\langle\hat{j}_y\rangle$, as defined in eq. (4.7).

In fig. 4.8, Hall currents close to the topological transition are shown for different system lengths. To reduce the numerical cost, results are computed for $W = 2$. However, since the divergence of $\langle\hat{j}_y\rangle$ is only due to the $k = 0$ leg, increasing W should not make a qualitative difference when the legs are uncoupled at $U_o = 0$.

[1] Keep in mind that the sign of the intra-ring kinetic term $\propto t_y$ redefines δ compared to section 3.2.3.

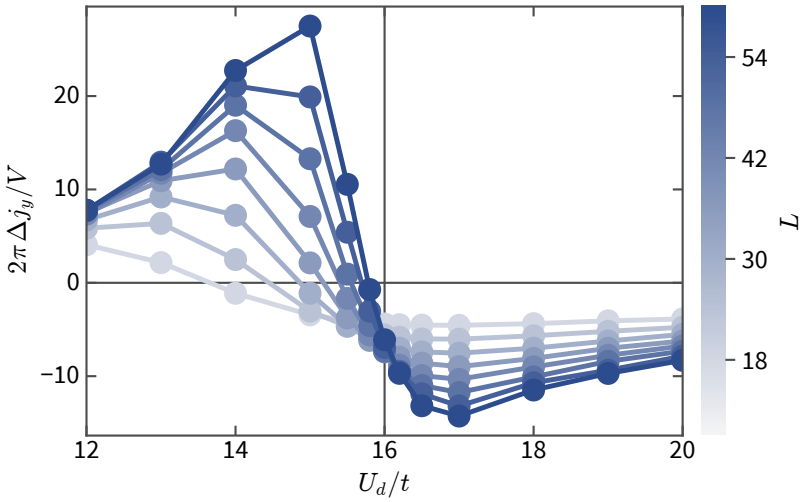

Figure 4.8: *Finite-length dependence of the Hall current close to the topological phase transition.* Data are shown for $W = 2$ at $U_o = 0$ and $\delta = 0$ for $L \in \{18, 24, 30, 36, 42, 48, 54, 60\}$. Unlike for other plots, we do not perform a linear fit of χ_{Hall} because the response can be nonlinear close to the transition. Here, we compute the Hall current as $\Delta j_y := j_y(V) - j_y(0)$, where $j_y = \langle \hat{j}_y \rangle$ is computed for ground states, and $V = 2.8 \times 10^{-3} t$. For $L \to \infty$, the Hall current diverges, and changes its sign at the phase transition $U_d \approx 16t$, where the 1D superlattice model exhibits a spontaneously dimerized phase. For other twist angles δ, the response χ_{Hall} does not diverge, but crosses through zero continuously, as shown in fig. 4.6.

We find that for longer cylinders, the interaction strength U_d at which $\Delta j_y 5 = 0$ approaches the critical value $W \times U_{c,1\text{D}} \approx 16t$ from below. The diverging Hall response indicates a discontinuity in $\langle \hat{j}_y \rangle$ for $L \to \infty$.

4.2.2 Thin-cylinder limit

In order to study a broad range of interaction strengths U_d, U_o, we choose a width of $W = 2$, which is the easiest to study numerically. In the real-space representation, the case of $W = 2$ seems to be special: If there are only two legs, a particle cannot move around the "cylinder", and thus all complex tunneling rates vanish, and there is no flux, cf. [212],

$$\begin{aligned} \hat{H}_{W=2} = \sum_x \sum_{y=0}^{1} \Big(& - t_y \cos(2\pi\alpha x - \delta/2) \hat{\boldsymbol{c}}^\dagger_{x,y} \cdot \hat{\boldsymbol{c}}_{x,y+1} \\ & - t \hat{\boldsymbol{c}}^\dagger_{x,y} \cdot \hat{\boldsymbol{c}}_{x+1,y} + \text{H.c.} \Big) + \hat{H}_{\text{int}} \,. \end{aligned} \tag{4.11}$$

However, we argue that this is rather due to the chosen basis: In the hybrid-space representation in eq. (4.2), there are no complex phases, anyway. We discuss the effect of a larger width in the following section 4.2.3.

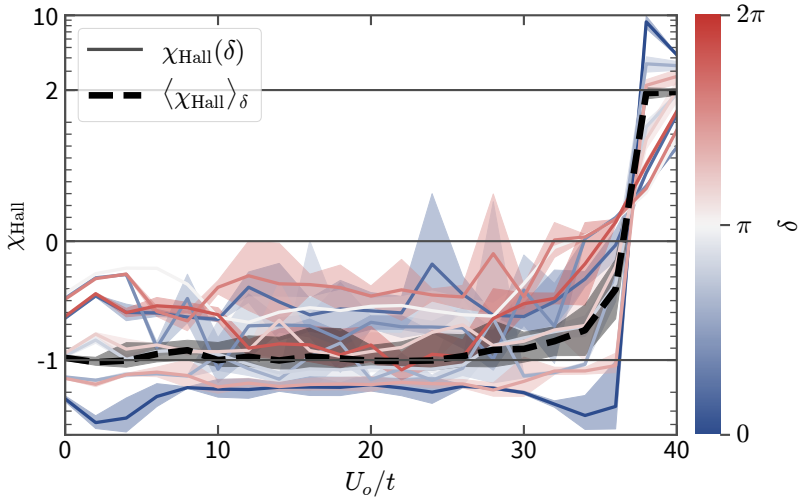

Figure 4.9: *Hall response for a cut through fig. 4.10 at* $U_d = 40t$. Thin, colored lines show the fitted value of χ_{Hall}, the corresponding shaded regions indicate the uncertainty as measured by the cost of the fit: Higher cost corresponds to less linear behavior of $\langle\hat{j}_y\rangle(V)$, due to numerical errors and finite-size effects. Errors are larger than in fig. 4.6, because the terms of $\hat{H}_{\text{int},o}$ greatly increase the numerical complexity. The average over all δ values is shown as dashed, black line. It takes the value $\chi_{\text{Hall}} = -1$ up to $U_o = 30t$ and $\chi_{\text{Hall}} = 2$ for $U_o \gtrsim 37t$. Data are show for $W = 2$, $L = 30$, $\delta \in \{0, 0.2, 0.4, 0.6, 0.8, 1, 1.2, 1.4, 1.6, 1.8\} \times \pi$. Greater numerical precision and more samples would be required to show integer quantization. The χ_{Hall} axis is logarithmic for $|\chi_{\text{Hall}}| > 1$, in order to suppress the outliers for $\delta = 0$, see section 4.2.1, and to focus on the topological transition.

We show a plot for the Hall conductivity χ_{Hall} for finite $U_o \geq 0$, and fixed $U_d = 40t$ in fig. 4.9. We find that the $C = -1$ phase also exists for $36t \gtrsim U_o \geq 0$, but does not extend to the Hofstadter-Hubbard model, for $U_d = U_o$. The sign of the response χ_{Hall} does not depend on the twist angle δ, except close to the transition, where a finite-size extrapolation would be required, cf. section 4.2.1. The errors of the fits are larger than for $U_o = 0$ as in fig. 4.6, because the increased number of terms in $\hat{H}_{\text{int},o}$ makes the problem numerically harder.

Figure 4.10 shows the Hall conductivity for various interaction strengths U_d and U_o. We find that the $C = -1$ phase extends to the region $U_o > 0$ for strong interactions $U_d > 16t$, depicted by the blue region. As we further increase U_d, the $C = -1$ region becomes larger, such that it approaches the Hubbard-Hofstadter limit on the diagonal, at $U_d = U_o$.

The data in fig. 4.10 are averaged over 10 values of the twist angle δ. This is not necessarily sufficient to verify integer quantization, as one can see by the slight variations in color. However, as the quantization is topological, it suffices to verify integer values for single combinations of interaction strengths U_d and U_o, as shown in fig. 4.4.

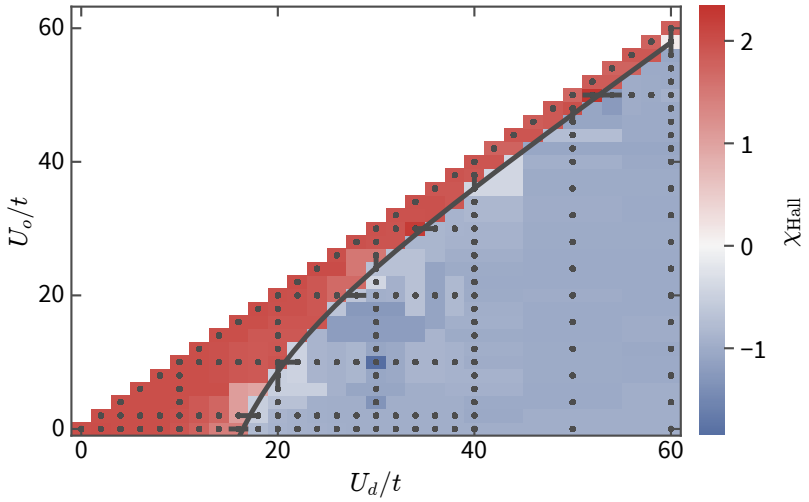

Figure 4.10: *Topological phase diagram as a function of interaction strengths for* $W = 2$. A horizontal cut at $U_o = 0$, corresponding to the quasi-1D model, is shown in fig. 4.6. We find that the $C = -1$ phase extends to finite values of the ring-wise interactions U_o. For large U_d, the topological transition approaches the diagonal $U_d = U_o$. However, the Hofstadter-Hubbard model ($U_d = U_o$) remains in the $C = 2$ phase, which is adiabatically connected to the band insulator, for all interaction strengths considered. A cut of this plot at $U_d = 40t$ is shown in fig. 4.9. The gray line indicates the topological phase transition, and it is estimated from the shown data set. Data are shown for $L = 30$, $W = 2$ and averaged over $\delta \in \{0, 0.2, 0.4, 0.6, 0.8, 1, 1.2, 1.4, 1.6, 1.8\} \times \pi$. We have computed χ_{Hall} for the parameters indicated by gray dots. In between those points, we use an interpolation for visualization purposes.

The gray line in fig. 4.10 shows our estimate of the phase boundary between $C = -1$ and $C = 2$ phases. Up to $U = U_d = U_o = 60t$, the Hofstadter-Hubbard model seems to remain in the $C = 2$ phase, which is adiabatically connected to the free model. This result indicates that there is a topological phase transition between interacting 1D charge pumps and the interacting 2D Hofstadter-Hubbard model.

4.2.3 Transition in wider cylinders

As stated in the previous subsection, the case of $W = 2$ seems to be different from wider cylinders. While we expect the $C = -1$ phase to exist in the quasi-1D limit ($U_o = 0$) for any system size, the required interaction strength U_d is proportional to the width W due to the prefactor in eq. (4.4). Thus, the $C = -1$ phase might not exist in the 2D thermodynamic limit.

In order to answer this question, we have to simulate wider systems, which is in general exponentially hard, cf. the discussion in section 2.1.3. Therefore, we can only perform

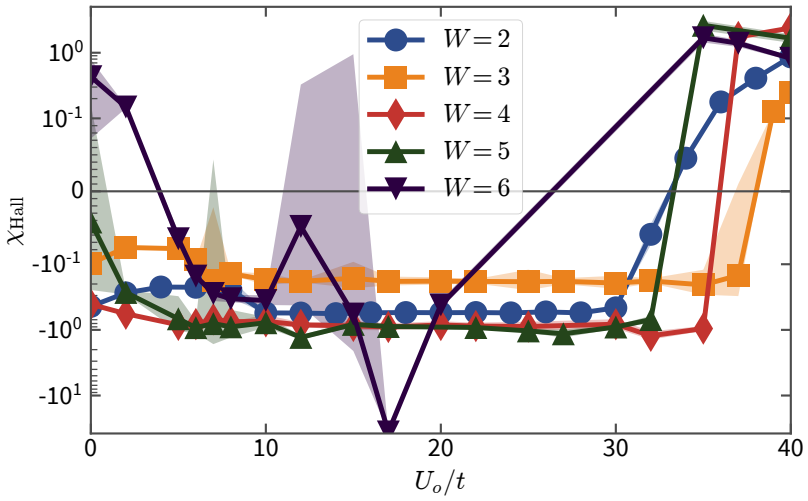

Figure 4.11: *Hall response for systems of different widths W at interaction strength $U_d = 40t$.* All systems exhibit $C = -1$ and $C = 2$ topological phases, even though $40t \leq 8Wt$ for the widest cylinders shown. Data are computed for the single twist angle $\delta = \pi$. Therefore, we can only infer the sign, but not the magnitude of $\langle \chi_{\mathrm{Hall}} \rangle_\delta$. Data are obtained for $L = 30$.

simulation for select cuts through the topological phase diagram shown in fig. 4.10. In addition, we will only consider a single value of δ: We cannot verify integer quantization of χ_{Hall}, but we will only consider the sign of $\chi_{\mathrm{Hall}}(\delta)$. The assumption that the sign of $\chi_{\mathrm{Hall}}(\delta)$ is based on our observations for $W = 2$. For wider systems, we expect the dependence on twist angle δ to decrease.

Results for interaction $U_d = 40t$ and widths $W \in \{2, 3, 4, 5, 6\}$ are shown in fig. 4.11. We use DMRG bond-dimensions up to $m_{SU(2)} = 10^4$, which might still be insufficient for systems of width $W = 5, 6$. While the error bars are larger for these system sizes, and there are fewer data points due to convergence issues, the behavior is qualitatively consistent: For $W = 5$ and $U_d = 40t \approx U_{c,1\mathrm{D}}\, W$, the topological transition occurs for $U_o = 0$, i.e., in the quasi-1D model. Surprisingly, the Hall response is negative for $0 < U_o \leq 30t$. This indicates the existence of the $C = -1$ phase for a larger parameter space than we had expected from fig. 4.10. The data for $W = 6$ are more noisy, but consistent with this observation: Even though $U_d = 40t < 6 \times U_{c,1\mathrm{D}}$, the $C = -1$ phase seems to exist for $U_o > 0$.

In fig. 4.12, we show the boundary of the $C = -1$ phase for $U_o \leq U_d$ at widths $W \in \{2, 3, 4, 5, 6\}$. We observe that the shape of the phase boundary changes with width: For $W \geq 4$, there exist regions of $C = -1$ at smaller U_d than what we would expect from scaling up $W = 2$ data, i.e., $U_{d,\mathrm{crit}}(U_o > 0) < W\, U_{c,1\mathrm{D}}$.

The data in fig. 4.12 might indicate that parts of the phase boundary do not change with W. Close to $U_d = 25t$, $U_o = 15t$, there might be a point where the phase boundaries for $W \in \{2, 3, 4\}$ coincide. However, we could not obtain reliable data for $W = 5, 6$ to confirm this observation. If any part of the phase boundary is independent of the

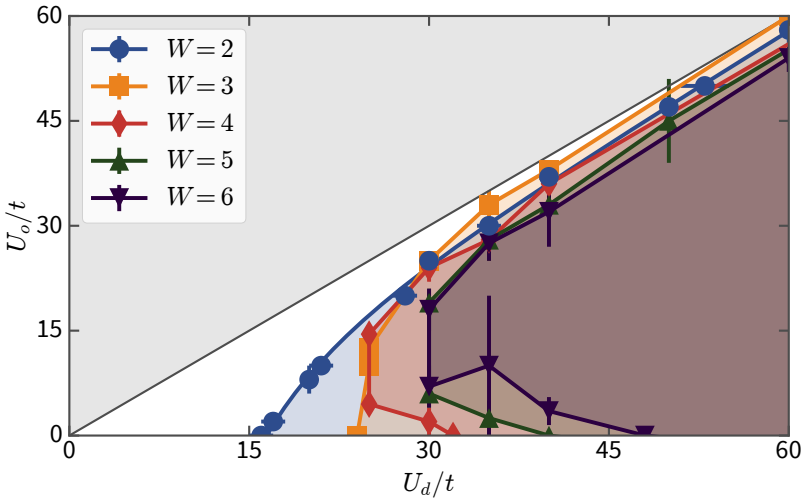

Figure 4.12: *Topological transition for different widths.* The colored regions indicate the $C = -1$ phase, the lines are guides to the eye. Parameters in the gray region, $U_o > U_d$ have not been considered for this plot. For $U_o = 0$ the critical interaction strength $U_{d,\mathrm{crit}}$ scales proportional to W. For finite U_o, the dependence on width decreases. Data were obtained for length $L = 30$. For $W = 2$, we use data from fig. 4.10, averaging over ten twist angles δ. Results for wider cylinders were computed only for fewer values of δ.

width, the $C = -1$ phase will also exist in the 2D thermodynamic limit for finite U_d and U_o.

4.2.4 Interacting quench dynamics

So far, we have computed the Hall response χ_{Hall} strictly adiabatically, meaning that we perform DMRG sweeps for each value of the potential strength V. As described in section 4.1.2 for the free model, weak quenches should generally yield the same results. In fig. 4.13, we show that the change of the Chern number can also be measured in such quench experiments. While the system size shown in fig. 4.13 is too small to observe quantization, both the sign and the amplitude of χ_{Hall} change as the interaction strength crosses the critical value $U_d \approx 24t$. We show data for a single twist angle δ, since averaging over twist angles might not be possible in experiments, either.

In order to probe the regime of linear response, we switch on a weak potential $0 < V \ll t$, such that the state remains "close" to the ground state. Therefore, the entanglement entropy does not increase strongly with τ, and rather long times $\tau\, t > 10$ can be reached at small bond dimensions.

The data in fig. 4.13 are obtained using a single-site variant of the TDVP algorithm [151, 213]. We use a step size of $\Delta_\tau t = 0.1$ and fix the bond dimensions at $m_{SU(2)} = 3000$. We verify the results up to $\tau t = 10$ by comparing with other simulations in fig. 4.14. There is very good agreement with the two-site TDVP method, and with the result of

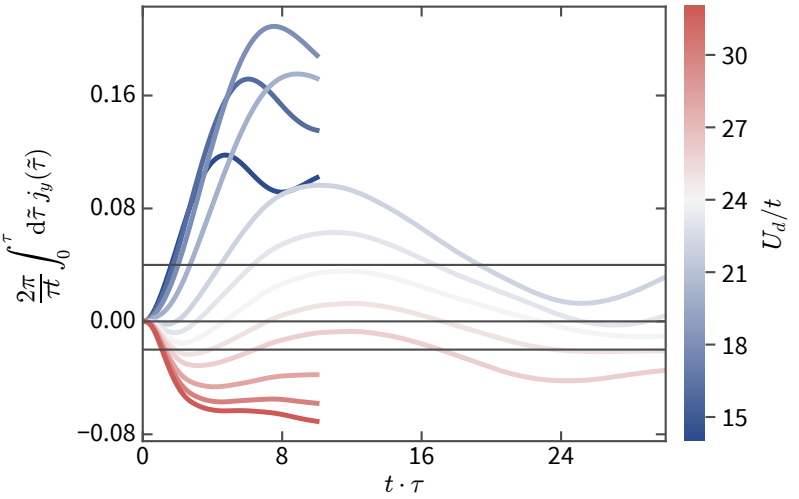

Figure 4.13: *Time-dependent response of the Hall current $\langle \hat{j}_y \rangle$ after quenching a linear potential from $V = 0$ to $V = 0.02t$.* The data are shown for $L = 18$, $W = 3$, $\delta = 0$, $U_o = 0$ for different interaction strengths U_d. We average the current over time τ to suppress oscillations. The gray, horizontal lines indicate values for $C \in \{-1, 0, 2\}$. For a finite system size, we would have to average over several twist angles δ in order to observe quantization and the topological transition at $U_d \approx 24t$. We restrict the simulation time to $\tau\, t \leq 10$ for small and large U_d, because there was no ambiguity in the sign of $\langle \hat{j}_y \rangle$.

simulations performed with $\Delta_\tau t = 0.05$, as well as $m_{SU(2)} = 5000$. Here, we have chosen the interaction strengths to be very close to the quantum phase transition for $\delta = 0$, which we expect to be the numerically most challenging case. The states compared in fig. 4.13 themselves are different, i.e., the entanglement entropy is larger for greater bond dimensions or two-site methods (not shown), but that seems to be irrelevant for the observable of interest, j_y. Comparing time-evolution methods for other, non-critical parameters yields similar agreement (not shown).

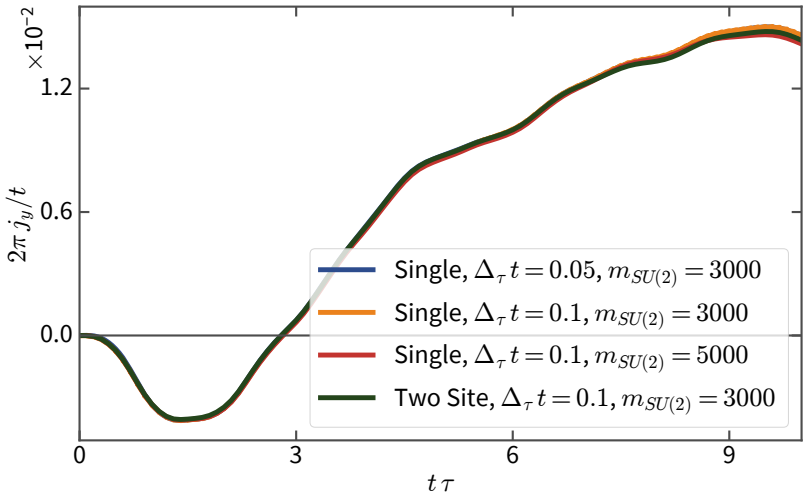

Figure 4.14: *Comparing variants of the TDVP method for time evolution.* Data are shown for single-site and two-site algorithms for different step sizes Δ_τ and maximal bond dimension $m_{SU(2)}$. We choose parameters $U_d = 24t$, $U_o = 0$, $\delta = 0$ at size $L = 18$ and $W = 3$, corresponding to one curve in fig. 4.13. Up to $\tau\, t = 10$, all results agree very well, comparisons for longer times have not been performed.

4.3 Ferromagnetic ground state

In the previous section 4.2, we have restricted the DMRG ground-state search to the spin-singlet, $S = 0$, symmetry sector. We find the singlet to be the lowest-energy state, both for 1D superlattices, see section 3.2.3, and for the 2D Hofstadter-Hubbard model. However, for some parameters in the $C = -1$ phase, spin sectors with $S > 0$ exhibit lower energies. In particular, the true ground state can be in the ferromagnetic (FM) sector with $S = N/2$.

In our model, eq. (4.2), the charge degrees of freedom of any ferromagnetic ground state behave exactly as a system of spinless fermions would. This brings us back to the argument from section 3.3.2, that topological properties of a strongly-interacting spin-singlet state could be deduced from a spinless model with the same particle density.

4.3.1 Ferromagnetism for Width $W = 2$

In fig. 4.15, we show the energy difference between the ground-state energy in the ferromagnetic sector E_{FM} and the lowest energy spin-singlet state $E_{S=0}$. Depicted by the blue region, there exists an FM region for strong interactions $U_d \gtrsim 40t$, and finite, but smaller, interaction strength $0 < U_o < U_d$.

Note that we define the FM region by the energy difference $E_{\mathrm{FM}} - E_{S=0}$, but do not take other spin sectors into account. Spin sectors with $0 < S < N/2$ can be energetically favorable, but we only observe finite-S ground states at the phase boundary. Deep

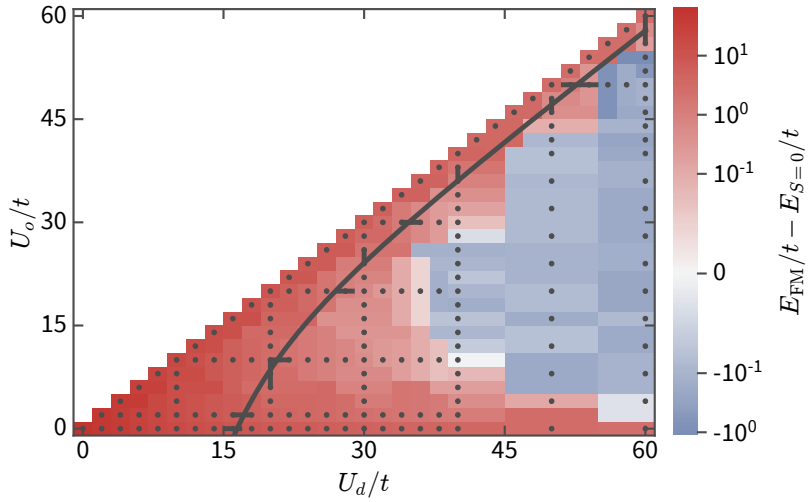

Figure 4.15: *Energy difference between the lowest-energy ferromagnetic state, and the ground state in the spin-singlet sector.* The spin singlet is the true ground state both for the 1D superlattice model and the 2D Hofstadter model. Data correspond to the systems shown in fig. 4.10, the gray line indicates the topological transition that we show in that plot. The gap is averaged over twist angles δ, and computed for $L = 30$ and $W = 2$ for the interaction parameters indicated by the gray dots. The shading is interpolated for visualization purposes.

inside the red, spin-singlet (blue, FM) region, the energy increases (decreases) monotonically as a function of total spin S. Therefore, taking all spins S into account would not change the phase diagram qualitatively. The precise position of $E_{\mathrm{FM}} = E_{S=0}$ also depends on the twist angle δ.

In fig. 4.15, we also show the gray line depicting the topological phase boundary from fig. 4.10. We find that the FM ground state lies entirely inside the $C = -1$ phase.

4.3.2 The FM ground state for wider cylinders

In fig. 4.16, we show how the extent of the FM ground state changes for wider cylinders. The boundary does not seem to change significantly as the system gets wider. Some fluctuations have to be expected, because the position of the boundary also depends on the twist angle δ, and going to larger W effectively changes δ.

This result seems to indicate that the FM phase also exists for large systems at finite U_d and U_o. If the appearance of the FM phase is related to the fact that we observe $C = -1$ in the spin-singlet state, this would suggest that the $C = -1$ phase also exists for larger systems at finite U_d when $U_o > 0$.

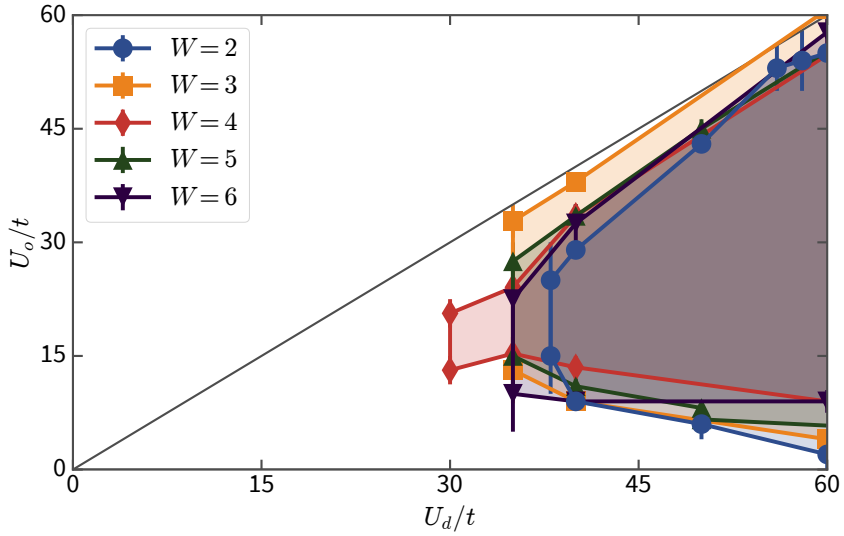

Figure 4.16: *Region with a ferromagnetic ground state for different widths.* The shaded region indicates where the ferromagnetic state is lower in energy than the spin singlet, i.e., the blue area in fig. 4.15. The lines are only guides to the eye. Error bars indicate the step size used for the interaction strength U_o. Data are shown for $L = 30$, $\delta = \pi$, except for $W = 2$, which is averaged over 10 values of δ as in fig. 4.15. The boundaries do not seem to change strongly when going to wider systems. We expect the dependence on W to be smaller, when a twist-angle average is performed.

4.3.3 Hall response in different spin-S symmetry sectors

For an FM state, we would indeed expect a Chern number $C = -1$: Double occupation is prohibited by Pauli's principle, both in real space, and in hybrid space. Therefore, both $\langle \hat{H}_{\text{int},d} \rangle$ and $\langle \hat{H}_{\text{int}} \rangle = \langle \hat{H}_{\text{int},o} + \hat{H}_{\text{int},d} \rangle$ vanish, and the spatial component of the wave function equals that of free, spinless fermions. As we had already argued in section 3.3.2, a single species of fermions at particle density $\rho = 2/3$ would occupy the lowest two bands of the Hofstadter model, such that the total Chern number would be the sum of the lowest two bands, $C = 1 - 2 = -1$.

At this point, enforcing the spin-$SU(2)$ symmetry, rather than the Abelian S^z symmetry is more than a technicality: Had we fixed $S^z = 0$ we would expect DMRG to converge a state in the $S > 0$ sector, whenever we are in the FM region. In that case, it would be easy to understand why DMRG results exhibit spinless-like behavior. However, fixing $S = 0$, as we did in section 4.2, does not allow DMRG to find a representant of the FM state.

To elucidate the dependence of the ground-state energy and Hall response on total spin S, we show numerical data for two interaction strengths in fig. 4.17. For the parameters $U_d = 40t$ and $U_o = 20t$, the spin singlet yields $C = -1$ and $E_{\text{FM}} < E_{S=0}$ such that we are in the FM phase as discussed in section 4.3. Computing ground states for all other possible spin multiplets, we find that the state for $S = 18$ is actually the true

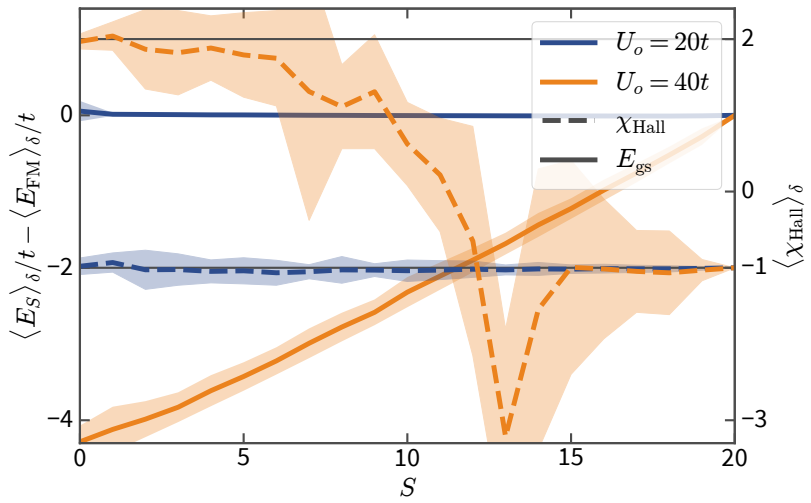

Figure 4.17: *Ground-state energy and Hall response in different symmetry sectors of the total spin S.* Data are displayed for $L = 30$, $W = 2$ and $U_d = 40t$ and are averaged over $\delta \in \{0, 0.2, 0.4, 0.6, 0.8, 1, 1.2, 1.4, 1.6, 1.8\} \times \pi$. We show data for different values for U_0: For $U_o = 20t$, we are in the $C = -1$ phase. In this case, the Hall response agrees with $C = -1$ for all values of S, and the FM state ($S = 20$) is slightly lower in energy than the spin singlet. For $U_o = 40t$, we find $\langle \chi_{\mathrm{Hall}} \rangle_\delta = C = 2$ in the spin-singlet ground state. Increasing S leads to an increase of the ground-state energy, but the Hall response remains consistent with $C = 2$ up to $S = 10$. For larger S, we recover the $C = -1$ phase since all interaction terms vanish for an FM state. We show the standard deviation of the ground-state energy with respect to δ by the shaded region.

ground state at this interaction strength. However, the states are nearly degenerate with $E_{\mathrm{FM}} - E_{S=18}$ being on the order of $10^{-4}t$. For stronger interaction U_d, the FM state is the true ground state, but the sectors remain nearly degenerate. Our results for the Hall response $\langle \chi_{\mathrm{Hall}} \rangle_\delta$, which we average over ten values for δ, do not depend on spin. They agree with the Chern number $C = -1$ for all values of S.

For $U_d = U_o = 40t$, the energy increases monotonically in S and the spin singlet is the true ground state. Since the singlet state is in the $C = 2$ phase, and the FM state has $C = -1$, the Chern number can, in general, not be independent of S. Our data suggest that the Hall response $\langle \chi_{\mathrm{Hall}} \rangle_\delta$ deviates from $C = -1$ and $C = 2$ for $N/8 < S < 3N/8$. The breakdown of quantization is plausible because in the free model, the topological invariant is only well defined when either $S = 0$ or $S = N/2$.

4.4 Isotropic model $t_y = t$

In the previous sections, and in our paper [2], we have considered the case of an anisotropic model with tunneling rates $t_y = 1.5t$. The value was chosen to match the

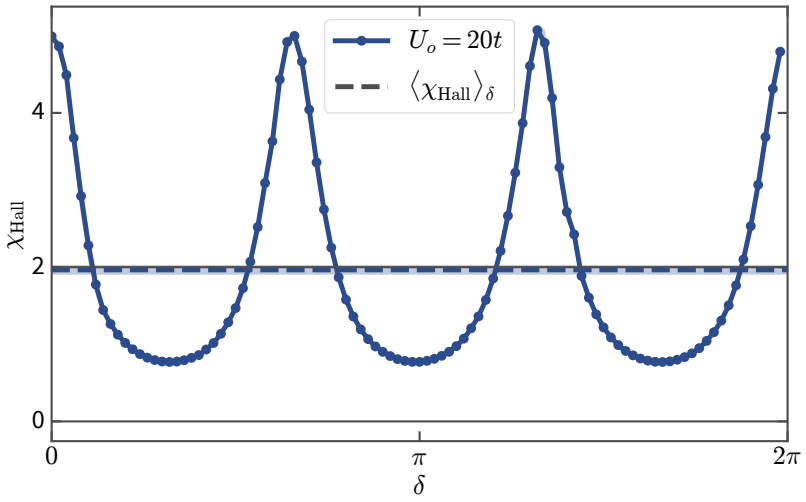

Figure 4.18: *Hall response χ_{Hall} in the isotropic model for $U_d = 22t$, $U_o = 20t$.* As for the anisotropic model, $t_y = 1.5t$, shown in fig. 4.4, the sign of $\chi_{\text{Hall}}(\delta)$ is constant, but the magnitude varies with the twist angle. The average over all $\delta \in [0, 2\pi)$ agrees with $\langle \chi_{\text{Hall}} \rangle_\delta = C = 2$ within error, as shown by the horizontal, blue line. Data are computed for $L = 30$, $W = 2$ to match fig. 4.20.

superlattice potential from the previous chapter 3. This raises the question whether an anisotropy is required for the appearance of $C = -1$ phases, and the ferromagnetic ground state. While we did not find the value of $V \sim 2t_y$ to be relevant in the 1D charge pump in section 3.3.2, the role of anisotropic tunneling rates in the Hofstadter model is generally an interesting question [214–216].

4.4.1 Topological phases

Simulating the isotropic Fermi-Hofstadter-Hubbard model in hybrid space, we find that both the $C = 2$ and the $C = -1$ topological phase exist in the narrow-cylinder limit. In fig. 4.18, we show the Hall response $\chi_{\text{Hall}}(\delta)$ for strong interactions $U_d \gtrsim U_o \gg t$. The errors for each value of δ are small, however, $\chi_{\text{Hall}}(\delta)$ exhibits sharp peaks, such that we slightly underestimate the average $\langle \chi_{\text{Hall}} \rangle_\delta$. Regardless, the average agrees well with Chern number $C = 2$.

The existence of a $C = -1$ phase, which cannot be adiabatically connected to the free Hofstadter model, is of greater interest. Figure 4.19 shows the Hall response for two strongly-interacting systems in the $C = -1$ phase. We find that the sign of $\chi_{\text{Hall}}(\delta)$ changes relative to fig. 4.18 for all values of δ, which is consistent with our observations for $t_y = 1.5$ in section 4.2. Using the same DMRG setup as for fig. 4.18, the errors in fig. 4.19 are significantly larger, and the results are less consistent, i.e., less symmetric under $\delta \to -\delta$.

In fig. 4.20, we show the topological phase diagram for the isotropic model. Qualitatively, it is identical to the one of the anisotropic model shown in fig. 4.10. As we had

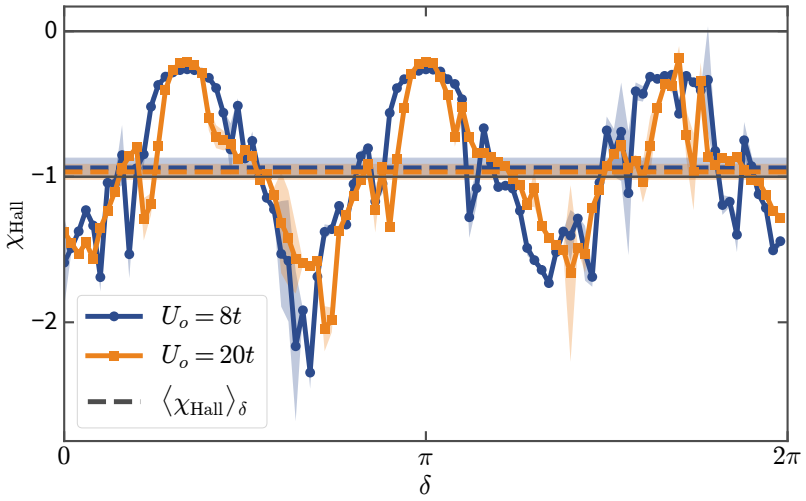

Figure 4.19: *Hall response χ_{Hall} in the isotropic model in the $C = -1$ phase.* Numerically, we observe more noise than for the $C = 2$ phase shown in fig. 4.18. The sign of $\chi_{\mathrm{Hall}}(\delta)$ remains constant, and the average $\langle \chi_{\mathrm{Hall}} \rangle_\delta$ agrees with $C = -1$ within the error. Data are computed for $L = 30$, $W = 2$ and interaction strength $U_d = 30t$.

expected from the 1D results shown in fig. 3.17, the topological transition occurs for smaller values of U_d. Here, the number of samples of δ is insufficient to show integer quantization in the $C = -1$ phase, in particular close to the phase transition, where $\chi_{\mathrm{Hall}}(\delta)$ diverges for some values of δ, cf. section 4.2.1.

4.4.2 Ferromagnetic ground state

The ferromagnet phase for $U_d \approx U_o/2 \gg t$ also exists in the isotropic model. Figure 4.21 shows the FM-singlet energy gap for $U_d = 30t$. The data are taken from the simulations for fig. 4.20. The singlet is lower in energy than the FM state for all smaller values of U_d which are shown there. $U_d = 30t$ seems to be right at the onset of the FM phase, as the spin singlet is still energetically favorable for some twist angles δ. Similar to the topological transition, the FM transition occurs for weaker interactions U_d when $t_y = t$, compared to $t_y = 1.5t$, considered in section 4.3.

4.5 Summary

We studied the fermionic Hofstadter model numerically on a cylinder, in a hybrid-space representation. We considered tunable interactions such that onsite repulsion in hybrid space (1D superlattice limit) and onsite repulsion in real space (2D Hubbard-Hofstadter limit) are the limiting cases. This parameterization allows us to connect interacting 1D charge pumps to interacting 2D Chern insulators.

For weak interactions, the 1D and 2D models are adiabatically connected to the same free model, thus, they exhibit the same topological properties. The 1D model undergoes

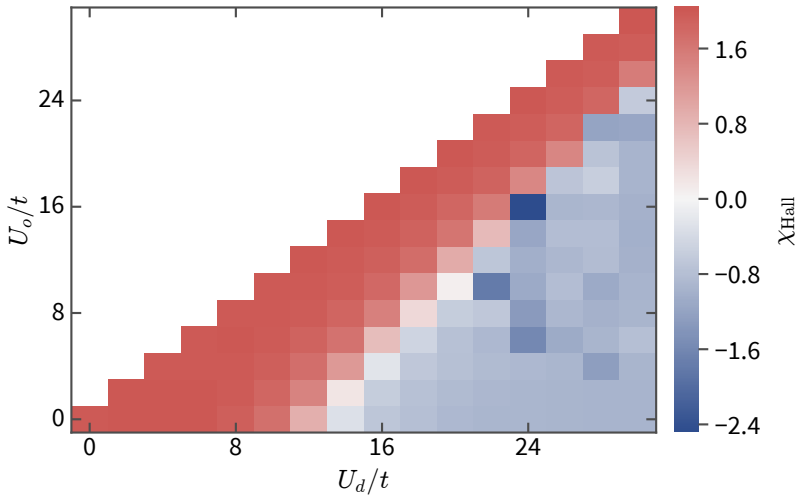

Figure 4.20: *Topological phase diagram for the isotropic, hybrid-space Hofstadter-Hubbard model.* Corresponding to fig. 4.10, data for $L = 30$ and $W = 2$ are shown for the isotropic model, $t = t_y$. Data are averaged over $\delta \in \{0, 0.2, 0.4, 0.6, 0.8, 1, 1.2, 1.4, 1.6, 1.8\} \times \pi$, allowing for some deviations from the quantized values $\chi_{\mathrm{Hall}} \in \{-1, 2\}$. We show agreement with integer-quantization for some parameters U_d, U_o in figs. 4.18 and 4.19.

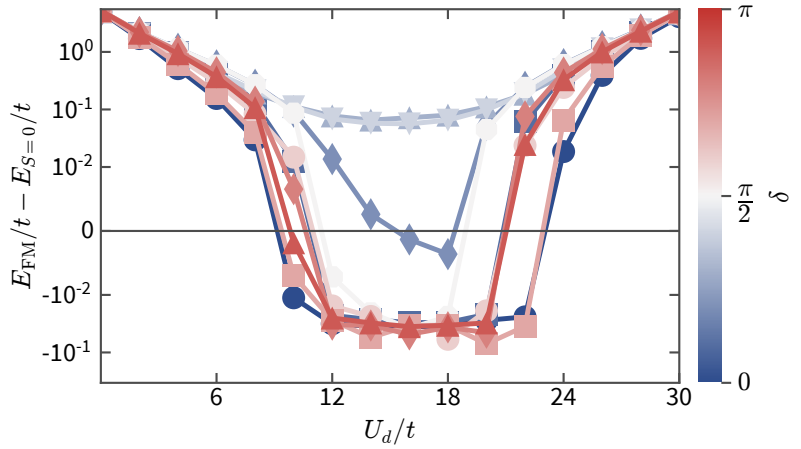

Figure 4.21: *Ferromagnetic energy gap in the isotropic model.* For strong interactions, $U_d \gg t$ and $U_o \approx U_d/2$, the FM ground state is lower in energy than the spin-singlet. We show data for $U_d = 30t$ on the onset of the FM phase, such that the singlet remains the true ground state for some values of δ. The system size is $L = 30$ and $W = 2$.

quantum phase transitions for strong interactions [165, 166, 168–175, 178, 183], which we discussed in section 3.2.3. In section 3.3.2, we found that the topological properties change as a result [1, 155].

In the quasi-1D case, where the hybrid-space legs are uncoupled, we reproduced the interaction-driven topological transition from a $C = 2$ topological insulator to one with Chern number $C = -1$. Depending on system size, averaging the Hall currents over twisted boundaries may be necessary to show topological quantization.

The interacting $C = -1$ insulator is robust under changes of the interaction terms. In our parameterization, it almost reaches the 2D Hubbard-Hofstadter limit. We verified the existence of the interacting $C = -1$ phase for numerically accessible cylinder widths $W \in \{2, 3, 4, 5, 6\}$, and found that it extends to larger parameter regions than we would expect from scaling up data for $W = 2$.

We computed the Hall response directly by applying a weak potential gradient adiabatically. Similar setups have already been realized in experiments with ultracold atoms [35, 39, 40]. We showed that we can measure an integer-quantized Hall response even for strongly-interacting systems. Our approach relies on periodic boundaries along the width of the system, which may be realizable in synthetic dimensional lattices [36]. However, weak quenches in open systems should yield similar results.

We also observed a region between 1D and 2D Hubbard interaction, where a ferromagnetic (FM) state is lower in energy than the spin-singlet sector. This region lies entirely inside the $C = -1$ phase. We showed that the FM phase exists for all widths considered. The phase boundary does not seem to depend strongly on the width W, indicating that the FM phase is robust for larger systems. An FM ground state necessarily has Chern number $C = -1$, due to the bandstructure of the Hofstadter model. This may indicate that the $C = -1$ phase in the spin-singlet symmetry sector is related to the FM ground state. Most of the simulations were performed for the anisotropic Hofstadter model, $t_y = 1.5t$, in order to relate our results to chapter 3. However, we found qualitatively the same physical effects when $t_y = t$, as we would have expected from section 3.3.2.

The family of models studied in this chapter is clearly motivated from theoretical considerations. However, tunable onsite and leg-wise interactions can be realized in synthetic-dimensional lattices [217]. While our results show that two-leg ladders suffice to observe a topological transitions, further research on more readily realizable models is necessary.

5 Outlook

In this thesis, we studied one- and two-dimensional interacting Hamiltonians with topological properties using numerical methods. Our goal was to predict quantum phases and their properties in rather small systems, akin to possible realization with ultracold atoms in optical lattices. There are different ways to continue this research:

- Studying experimental realizations. We chose parameters like the flux density $\alpha = 1/3$, or the interaction terms in section 4.1 for theoretical considerations. The Hamiltonians realized in (synthetic-dimensional) experiments will certainly differ, and require further numerical research. In addition, the simulations will become more challenging when finite temperatures are taken into account. Currently, most cold-atom experiments use bosonic particles, and we would generally expect that they exhibit qualitatively different behavior.
- Understanding the ferromagnetic ground state. The FM ground state, discussed in section 4.3, was a surprising discovery for us. Whether this phase persists in the thermodynamic limit, or in related physical models, is an open question. We will elaborate in section 5.1.
- Studying fractional quantum Hall insulators. The long-term goal of realizing interacting topological phases in ultracold atoms is to observe fractional quantum Hall systems, and their anyonic excitations. In principle, we believe that the settings used in section 4.1.2 should also work for fractionally-quantized Hall conductivity in small lattice models. However, we have not been able to produce conclusive results, yet. We discuss our preliminary findings in section 5.2.

5.1 Understanding ferromagnetic phases

In our simulations of the Hofstadter model with hybrid-space interactions, we found a parameter space, where the energy of the ferromagnetic state E_{FM} is lower than the ground state in the spin-singlet sector $E_{S=0}$. This property is rather interesting, because an FM state behaves like spinless fermions, meaning that:

- An FM state puts strong constraints on the degrees of freedom of the system, greatly increasing the kinetic energy. Naively, one might think that a singlet state should be able to mimic the properties of the charge degrees of freedom of an FM state. However, this is prohibited by the different exchange symmetries of charge and spin sector.
- An FM state exhibits exactly the same topological properties we found for strongly interacting $S = 0$ systems.

So far, we were able to show that the FM phase is robust when going to wider cylinders in section 4.3.2, and that it does not depend on anisotropic tunneling rates in section 4.4.2. But there are important, unanswered questions:

- Can we relate the topological properties of the ferromagnetic state to those of the spin singlet?
- Can we find an effective description, i.e., in terms of spin-spin interactions?
- Is this mechanism for ferromagnetism particular to our Hamiltonian, or is it more general to magnetic models with interactions, which are not onsite?

The latter could put our research in the context of ferromagnetism in the Hofstadter t-j model [218], or possibly in the context of itinerant ferromagnetism, which has also been studied using ultracold atomic gases [219].

5.1.1 Interactions in the FM region

We want to briefly discuss the derivation of an effective model to explain the ferromagnetic phase. Since the interactions in chapter 4 are inspired by the Hubbard model, it seems reasonable to follow the derivation for the t-J model [220, 221], which is an effective description of the strongly-repulsive 2D Hubbard model.

First, we have to "choose" the large energy scale. In section 4.3 we found the FM state for $U_d > U_o \gtrsim 40t$. Our numerical results suggest that a parameterization $U_d = 2U_o$ should capture the relevant physics. In that case, the interaction terms can be expressed in a suggestive form, using both real- and hybrid-space operators,

$$\hat{H}_{\text{int}} = U_d \hat{H}_{\text{int},d} + \frac{U_d}{2} \hat{H}_{\text{int},o} = \frac{U_d}{4} \sum_{x,k} \hat{n}_{x,k} \left(\hat{n}_{x,k} - 1 \right) + \frac{U_d}{4} \sum_{x,y} \hat{n}_{x,y} \left(\hat{n}_{x,y} - 1 \right) . \tag{5.1}$$

Here, the strength of interactions which are onsite in hybrid space, and those onsite in real space is the same. Therefore, our approximation should treat them equally.

Following the t-J derivation [220, 221], this would mean performing a Gutzwiller projection onto singly-occupied sites in both bases. We have not computed this projector explicitly, but given that the bases are related via a Fourier transform, it seems plausible, that only Pauli's exclusion principle can fulfill these constraints. In that case, deriving the J term, an effective spin-spin interaction, would be pointless, and ferromagnetism would just be a consequence of onsite repulsion in orthogonal bases.

5.1.2 Particle & hole doping

As numerical approach to understanding the ferromagnetic ground state, one may ask whether it depends on precise preparation. As an example, we study the robustness with respect to particle and hole doping into the singlet ground states for interactions $U_d = 2U_o$, as discussed in the previous subsection.

In fig. 5.1, we show that the FM state also exists when one or two holes are doped into a width $W = 2$ cylinder. Here, we compare the FM ground state with the lowest-energy spin singlet or doublet, depending on particle number. The low-S states become more favorable as more holes or particles are introduced. However, the general trend of $E(\text{FM}) - E(S \leq 1/2)$ over U_d is the same for all curves, and we expect that the FM

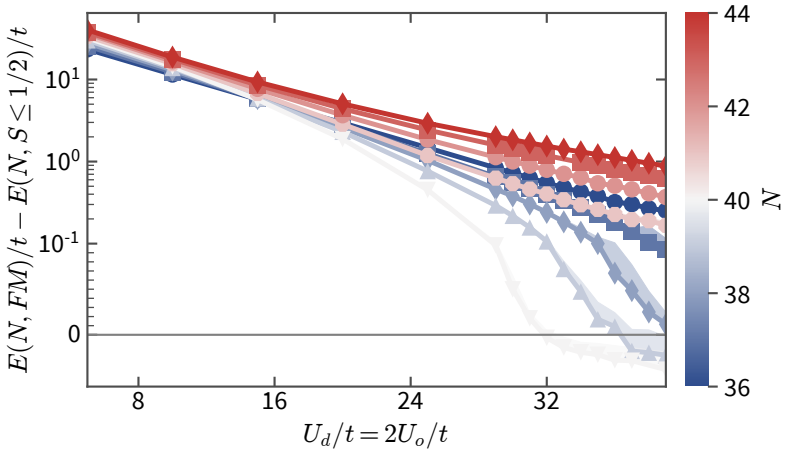

Figure 5.1: *Ferromagnetic energy gap for particle and hole doping at* $W = 2$. Data are show for interaction strengths $U_d = 2U_o$, which we discussed in section 5.1.1. We consider a system of length $L = 30$ and particle density $\rho = 2/3$, and dope $n \in \{-4, 3, 2, 1, 0, 1, 2, 3, 4\}$ particles. We perform DMRG in the lowest total spin multiplet $S \in \{0, 1/2\}$, and compare with the ferromagnetic state for the same particle number. The shaded regions indicate $\mathrm{var}_2(\hat{H})^{1/2}$, which is typically larger than the numerical error, cf. section 2.3.1.

state becomes the true ground state for all particle numbers when the interaction is further increased. We find an asymmetry for particle or hole doping, i.e., the energy difference $E(\mathrm{FM}) - E(S \leq 1/2)$ is always larger for particle-doped states than for hole doping. This is simply a consequence of choosing particle density $\rho = 2/3$, which is a band insulator in the ferromagnetic state, i.e., additional particles have to overcome the band gap.

We have performed simulations for cylinders of width $W = 3, 4$, and found qualitatively similar results: The FM state becomes less favorable when either particles or holes are doped. However, for sufficiently strong interactions, the FM state seems to be the true ground state. We believe that these findings support our argumentation of the previous subsection, i.e., for this model, ferromagnetism is a consequence of onsite repulsion in orthogonal bases.

5.2 Fractional quantum Hall effect

A primary goal to studying topological phases in ultracold atomic systems, is the realization of states with intrinsic topological order. The primary examples are fractional quantum Hall (FQH) states [222], which typically exist in strongly interacting systems. This field of research is fueled by the theoretical prediction of non-Abelian, anyonic excitations [75, 223] with possible applications, e.g. to topological quantum computing [224]. So far, there is little experimental evidence for the existence of anyons in conventional condensed-matter systems. Ultracold atomic gases hold out the prospect of more conclusive results, because of the possibilities to engineer Hamiltonians, and to perform advanced measurements.

Over the last ten years, various numerical studies on models which may be realizable with optical lattices have been performed. From a theoretical perspective, the question of how to unambiguously identify fractional Chern insulators in small lattice systems is particularly relevant. In principle, the definition of the Berry curvature with respect to twist angles [113] can also work in that case [225, 226], however, the ground-state degeneracy needs to be taken into account [149]. Similarly, one can directly probe the topological ground-state degeneracy in a typical numerical setup: By adiabatic flux-insertion, i.e., varying the angle of twisted boundaries, the degenerate states can be transformed into each other [226–232]. Other approaches to detecting topological order rely on the entanglement entropy [141, 192, 230, 233, 234], or the entanglement spectrum [141, 144, 229, 235].

These quantities can easily be computed, and are of theoretical interest, but are generally difficult to access in an experiment. Bridging the gap to ultracold-atom experiments, FQH states in (synthetic) flux-ladder systems [236–238], and in Floquet-engineered topological bands [231, 239, 240] have been studied. The realization of fractional Chern insulators in quasi-1D systems, as studied in this thesis, can be probed by measuring either edge currents in open ladders [236, 237], or the polarization as function of flux insertion, which is directly related to the Hall conductivity [144, 191, 192, 232, 238, 241] in a cylindrical geometry. Recently, it was shown that the displacement of an atomic cloud as response to an electric field can also be related to fractionalized conductivity [206, 207].

We expect that a fractional Hall conductivity can also be measured as a current response to a weak linear potential, i.e., a static electric field. As described in section 4.1.2, this requires a cylindrical geometry to facilitate persistent currents j_y, and to allow for the external potential. Generally, averaging over a twist angle will be necessary to verify quantization, cf. section 4.1.2. Therefore, this approach is not necessarily easier to realize, experimentally, than adiabatic flux insertion [144, 191, 192, 232, 238, 241]. However, the dependence on the twist angle should decrease for larger cylinder circumferences, such that "almost" quantized conductivies could be measured in a single, sufficiently large experimental setup.

As a first test of our approach, we follow the numerical study by Schoonderwoerd et al. [192] who found a Chern-insulator to fractional-Chern-insulator transition in a spinless Fermi-Hofstadter system by means of adiabatic flux insertion in an infinite-DMRG setup.

We will thus study the spinless Hofstadter model with nearest-neighbor interactions,

$$\hat{H} = \sum_{x=1}^{L} \sum_{y=1}^{W} \Bigg[\Big(- t_y \, \mathrm{e}^{2\pi i \alpha x - i\delta/W} \, \hat{c}^\dagger_{x,y} \hat{c}_{x,y+1} - t \hat{c}^\dagger_{x,y} \hat{c}_{x+1,y} + \mathrm{H.c.} \Big) + U \left(\hat{n}_{x,y} \hat{n}_{x,y+1} + \hat{n}_{x,y} \hat{n}_{x+1,y} \right) \Bigg] . \tag{5.2}$$

We choose the same parameters as ref. [192]: Isotropic tunneling rates $t_y = t$, $\alpha = 3/11$ flux quanta per plaquette, and the lowest band fully occupied at $\rho = 1/11$. For these parameters, the band gap is only about $0.04t$, and we have to reduce the strength of the applied linear potential V accordingly, cf. section 4.1.2.

As in chapter 4, we perform the DMRG ground-state search in hybrid space. The kinetic part of the Hamiltonian looks exactly like its spinful counterpart,

$$\hat{H} = \sum_{x,k} \Big[- 2t_y \cos(2\pi(\alpha x + k/W) - \delta/W) \hat{n}_{x,k} - t \hat{c}^\dagger_{x,k} \hat{c}_{x+1,k} \Big] + \hat{H}_{\mathrm{int}} \, . \tag{5.3}$$

Both interaction terms become three-fold sums, the term for neighbors along the system's width also acquires a complex phase,

$$\sum_{x,y} \hat{n}_{x,y} \hat{n}_{x,y+1} = \frac{1}{W} \sum_{x} \sum_{k,p,q} \mathrm{e}^{2i\pi(k-p)/W} \, \hat{c}^\dagger_{x,k} \hat{c}_{x,p} \hat{c}^\dagger_{x,q} \hat{c}_{x,q+k-p} \, , \tag{5.4}$$

$$\sum_{x,y} \hat{n}_{x,y} \hat{n}_{x+1,y} = \frac{1}{W} \sum_{x} \sum_{k,p,q} \hat{c}^\dagger_{x,k} \hat{c}_{x,p} \hat{c}^\dagger_{x+1,q} \hat{c}_{x+1,q+k-p} \, . \tag{5.5}$$

The sum of terms acting on different rings in eq. (5.5) might yield complicated MPOs as the system's width increases. However, the terms preserve total quasimomentum K, such that we can restrict DMRG to states which preserve the $\mathbb{Z}_W$ symmetry [144]. This is probably not necessary for performance improvements, but it will allow us to study the competition between different K sectors.

Numerically, this model is much simpler than the 2D systems studied in chapter 4: Without the spin degree of freedom, the local dimensionality is only 2, and the small particle density greatly reduces the number of possible states. Furthermore, at the relevant interaction strengths, the particles typically remain in the lowest energy bands, such that much larger systems can be simulated when the Hamiltonian is projected onto the relevant space [227, 229, 233]. However, the topological ground-state degeneracy could create numerical difficulties: Resolving the entire ground-state manifold might require sequential DMRG runs with orthogonalization. In section 5.2.2, we show how it may be possible to label the different ground states with quantum numbers.

5.2.1 Narrow-cylinder limit $W = 2$

As a starting point, we consider the limit of width $W = 2$, and restrict ourselves to a single length $L = 33$. As the interactions are not onsite, we do not expect that the case $W = 2$ directly corresponds to wider cylinders.

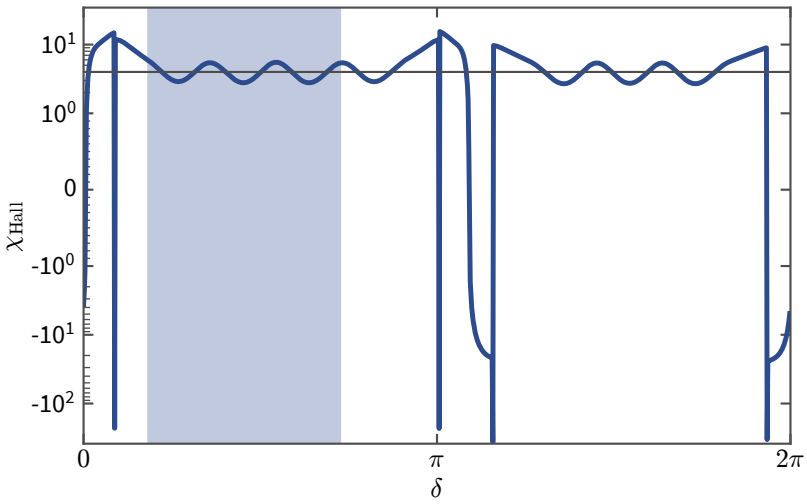

Figure 5.2: *Hall response for the free Hofstadter model for* $\alpha = 3/11$, $\rho = 1/11$, $L = 33$, $W = 2$. Data are shown for an applied linear potential $V = 10^{-4}t$. Even in the free model, averaging χ_{Hall} over twist angles δ is pointless, because there are severe outliers. However, there are regions of the parameter δ, where χ_{Hall} oscillates around the expected, quantized value $\chi_{\mathrm{Hall}} = 4$ (indicated by the horizontal line). We will restrict our simulations to the shaded region, where χ_{Hall} is well behaved.

Unfortunately, computing the Hall response is more difficult than in chapter 4, even for the noninteracting model. We show data for the narrow, free model in fig. 5.2, obtained by applying $V \in \{0, 10^{-4}t\}$ as described section 4.1.2. The Hall response χ_{Hall} exhibits strong dependence on twist angle δ, and also its sign changes—unlike for all simulations in chapter 4. Since the outliers can be orders of magnitude larger than the expected, quantized value, averaging over the twist angle is pointless in the interacting model.

We try to circumvent the difficulties of the twist-angle average by restricting the range of δ considered for the interacting DMRG simulations. While this approach lacks theoretical motivation, both numerical studies, and experiments are often restricted to a single twist angle, such that this approach might suffice to gain first insights. For $W = 2$, we only perform DMRG for twist angles δ in the shaded region in fig. 5.2, where $\chi_{\mathrm{Hall}}(\delta)$ oscillates smoothly around the Chern number of the lowest band, $C = 4$.

By this choice of twist angles, one should assume that $\chi_{\mathrm{Hall}}(\delta)$ for the weakly interacting system is also smooth. This is indeed the case, as shown in fig. 5.3. However, we have to take into account, that the true ground state is in the quasimomentum $K = 1$ sector. We find a qualitatively different behavior for the lowest-energy state in the $K = 0$ sector. However, the $K = 0$ states might not be insulators for weak interactions, such that our method to compute χ_{Hall} would be ill defined.

In fig. 5.4, we show data for the Hall response with strong interactions $U = 2t$. Here, data for both quasimomentum sectors deviate significantly from the Chern number in the free model $C = 4$—but also from the expected, fractional result $\chi_{\mathrm{Hall}} = 1/3$.

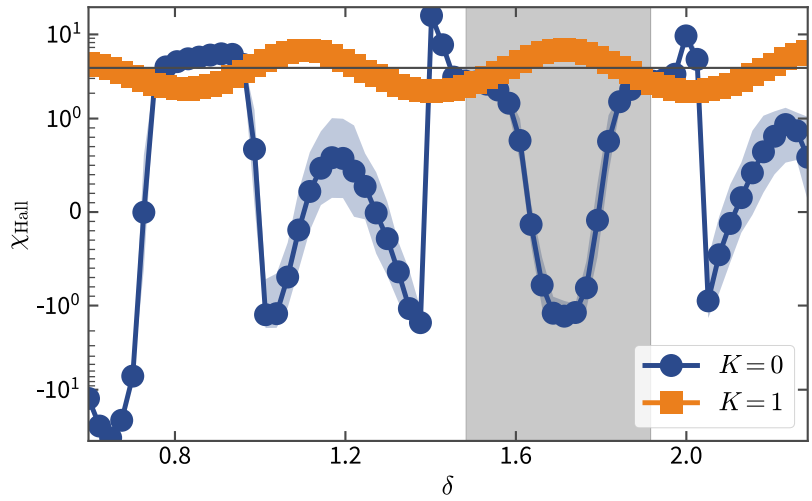

Figure 5.3: *Hall response for the spinless Hofstadter model for weak interactions* $U = 0.4t$. The ground state is in the $K = 1$ quasimomentum sector, and exhibits a response oscillating around $\chi_{\mathrm{Hall}} = 4$ (gray horizontal line), as expected from the free model shown in fig. 5.2. In contrast, sign and amplitude of χ_{Hall} depend strongly on δ for the lowest-energy state in the $K = 0$ sector. Data are simulated for $L = 33$, $W = 2$.

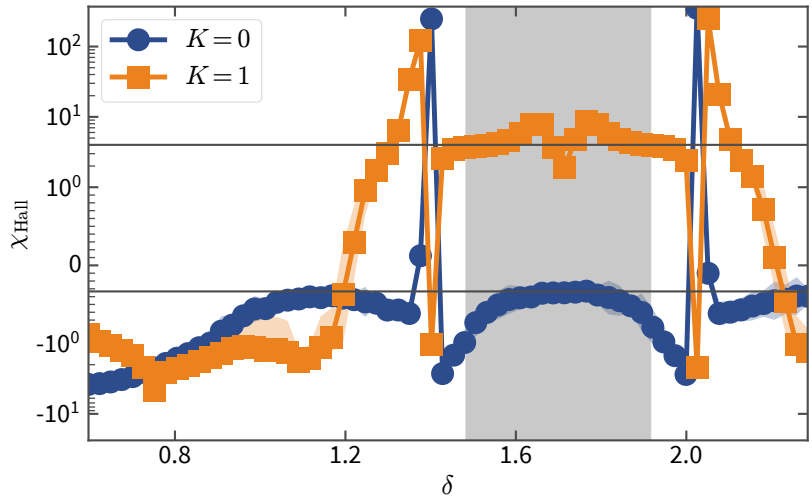

Figure 5.4: *Hall response for the spinless Hofstadter model for strong interactions* $U = 2t$. For strong interactions, the ground state lies in the $K = 0$ sector. The following analysis will be restricted to the shaded region where the $K = 0$ curve approaches and touches the value $\chi_{\mathrm{Hall}} = -1/3$. The horizontal lines indicate $\chi_{\mathrm{Hall}} \in \{-1/3, 4\}$. Data are simulated for $L = 33$, $W = 2$.

Instead, the Hall response for $K = 0$, which is the true ground state, is negative for most values of δ, and touches $\chi_{\text{Hall}} = -1/3$. In order to improve our data quality, but without theoretical motivation, we further restrict the range of twist angles δ to the shaded region in fig. 5.4 for the following numerical analysis.

While we cannot observe fractional quantization, it appears that the change of the Hall response and the transition between both quasimomentum K sectors coincide. In fig. 5.5 we compare the energy in the $K = 0$ and $K = 1$ sectors, and find that their energy difference crosses zero close to $U = 0.9t$. This is significantly smaller than the critical interaction strength $U_c \approx 1.6t$ found by Schoonderwoerd et al. [192], but that might be due to the special case of $W = 2$.

We can understand the energy difference between both sectors by looking at the occupation imbalance of hybrid-space legs: For the free model, we expect both legs to be occupied by the same number of particles, thus,

$$|\langle N(k=1) - N(k=0)\rangle_\delta| = 0\,. \tag{5.6}$$

This is true, as shown by the orange line in fig. 5.5. This configuration is only possible for $K = 1$, which contains the true ground state. However, for strong interactions $U \gtrsim t$, it turns out to be energetically favorable to put all particles on the same leg. This configuration is only allowed in the $K = 0$ symmetry sector.

So does this change of quasimomentum K actually coincide with the change of χ_{Hall}? Our preliminary data show that it might. In fig. 5.6, we show the Hall response χ_{Hall} for select values of the twist angle δ and different interaction strengths U. We choose quasimomentum K depending on U, such that data are only shown for the true ground state. While we cannot verify (fractional) quantization, the data for each K ground state are remarkably independent of interaction strength.

In order to make the point that the consistency of the curves in fig. 5.6 is notable, we also show data for the excited K sectors in fig. 5.7. We find that the response χ_{Hall} is only constant w.r.t. U in the true ground state.

We are surprised to find that $\chi_{\text{Hall}}(\delta) \leq 0$ in the strongly-interacting case for most values of δ. It is tempting to say that the sign of the Hall current is ill defined on a $W = 2$ "cylinder", as there is no sense of direction along y. Then, one could try to relate $\chi_{\text{Hall}} = -1/3$ plateaus to the expected $C = 1/3$ topological index [192]. But there are two shortcomings in this line of argumentation: Even though width $W = 2$ cylinders are a particular case, we found consistent results with larger W in section 4.2. In addition, the results discussed here are limited by the choice of twist angles.

It is rather peculiar that the change of ground-state quasimomentum appears to coincide with the changing Hall response χ_{Hall}:

- The change of K labels of the lowest-energy sector is probably an effect of finite size and small filling. Had we chosen a configuration with an even number of particles on each leg, e.g. $L = 44$, we would expect $K = 0$ to be the ground state for all interaction strengths U: In that case, the $K = 0$ sector would comprise both the state with equal occupation on both legs, and the maximally imbalanced one.

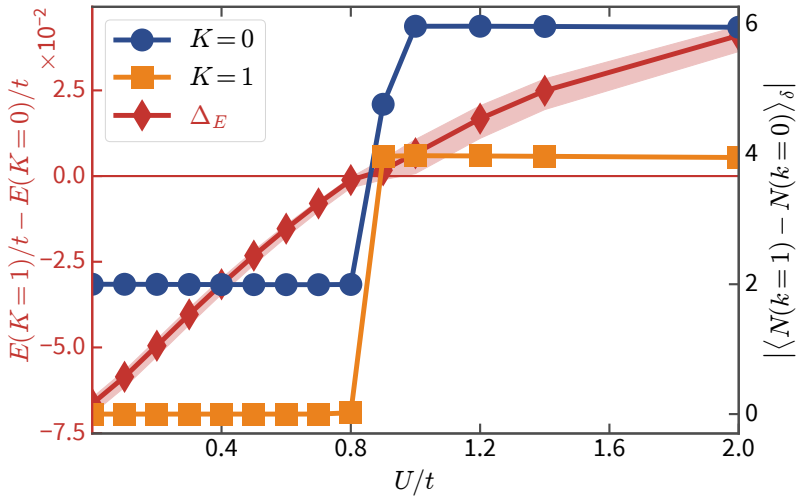

Figure 5.5: *Energy difference and leg-occupation imbalance for both quasimomentum K sectors.* The red diamonds show the energy difference between states in the $K = 0$ and $K = 1$ sector. Blue and orange lines show the occupation difference between $k = 0$ and $k = 1$ leg of each of those states. For $U = 0$, the lowest energy is achieved when both legs are occupied by the same number of particles. This is only possible in the $K = 1$ state, which is the true ground state. For strong interactions, the lowest energy is achieved when all particles are located on the same leg. Thus, the $K = 0$ sector contains the true ground state. Data are averaged over the values of δ in the shaded region of fig. 5.4. Here, the shaded region of the energy difference indicates the minimal (maximal) values with respect to δ. Data are simulated for $L = 33$, and $W = 2$.

- A topological transition requires some many-body gap to close, cf. section 1.3.2. So far, we only encountered closing of the gap within one symmetry sector in section 3.3.2. The ferromagnetic ground state, discussed in section 4.3, is another example, where the ground-state symmetry sector changes. However, in that case, the topological transition and the change of symmetry labels occur for different parameters, and the change of ground-state symmetry labels did not affect topological properties.

In the end, this preliminary discussion is limited by the fact that the "topological transition" is ill defined. A proper definition of a topological index would also require periodic boundaries along the system's length, including a second twist angle, or at least a careful finite-L analysis.

5.2.2 Wider cylinders

Increasing the cylinder's width should generally suppress the effect of twist angles [114–116], but the behavior need not be monotonous for the narrow systems accessible with

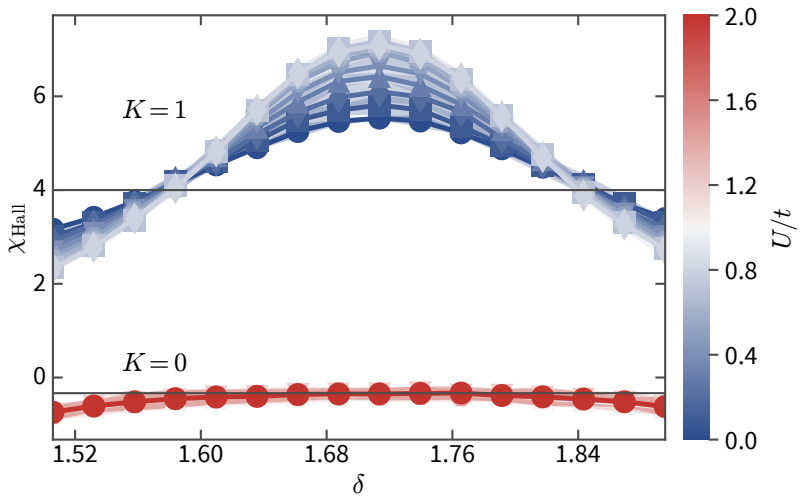

Figure 5.6: *Hall response χ_{Hall} only considering select values of δ, and the appropriate ground-state sector.* For weak interactions $U \in \{0, 0.1, 0.2, 0.3, 0.4, 0.5, 0.6, 0.7, 0.8\} \times t$, the $K = 1$ sector comprises the true ground state. Conversely, for strong interactions $U \in \{1, 1.2, 1.4, 2\} \times t$, we show data for the $K = 0$ sector. The horizontal lines indicate $\chi_{\mathrm{Hall}} \in \{-1/3, 4\}$. Data are simulated for $L = 33$, and $W = 2$.

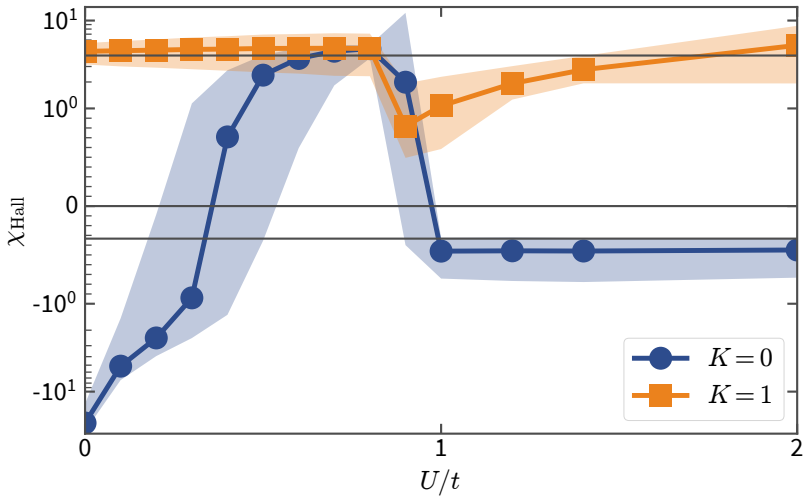

Figure 5.7: *Hall response χ_{Hall} over interaction strength.* Data are averaged over the values of δ used in fig. 5.6. The shaded region indicates minimal and maximal χ_{Hall} for those values of the twist angle. We find that χ_{Hall} is independent of U only when the respective K sector comprises the true ground state. Data are computed for $L = 33$ and $W = 2$.

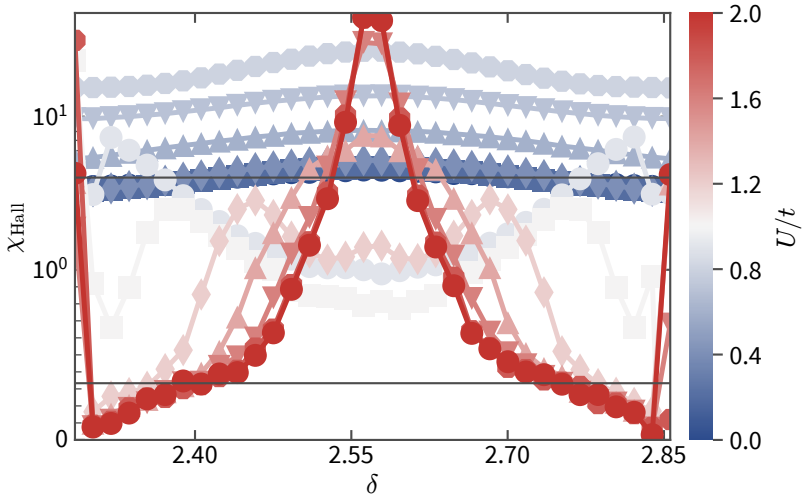

Figure 5.8: *Hall response for $W = 3$, and various interaction strengths.* Data are shown for the ground state for each δ. Curves for $U \in [0, 0.8t]$ seem qualitatively similar, though strongly vary in amplitude. Data for $U \in [0.9t, 1.4t]$ are somewhat inconsistent, and only for $U \in [1.6t, 2t]$, the dependence on U seems to decrease. The horizontal lines indicate $\chi_{\mathrm{Hall}} \in \{1/3, 4\}$ Data are obtained for $L = 33$.

DMRG. We find that the range of twist angles δ where χ_{Hall} is smooth in the free model can be smaller for $W > 2$ than shown in fig. 5.2. The following numerical simulations have only been performed for twist angles where $\chi_{\mathrm{Hall}}(\delta)$ is well behaved in the free model.

Unfortunately, the quality of the results for wider cylinders is not as good as the data for $W = 2$. This may be due to our restriction of twist angles δ, but could also be caused by more general limitations of our approach. Either way, we leave these issues for future research.

Width $W = 3$

For $W = 3$, we again find a transition of ground-state symmetry labels K: This time, $K = 0$ is the ground-state sector for $U = 0$, and $K = 1, 2$ become the lowest-energy states for large U. With strong interactions, the sign of $E(K = 1) - E(K = 2)$ depends on twist angle δ: For the parameters studied here, the states of these symmetry sectors can be related by relabeling $\delta \to 9\pi/11 - \delta$.

Choosing the lowest-energy K sector for each value of δ, we produce the analog of fig. 5.6 for width $W = 3$. In fig. 5.8 we find $\chi_{\mathrm{Hall}}(\delta)$ strongly varies with the interactions U, but we are unable to find a clear transition. This time, we find $\chi_{\mathrm{Hall}} > 0$ with strong interactions, and there are points close to $\chi_{\mathrm{Hall}} = 1/3$ where $\chi_{\mathrm{Hall}}(\delta)$ becomes independent of U. But χ_{Hall} strongly depends on δ for all interactions U, such that a twist-angle average does not make much sense.

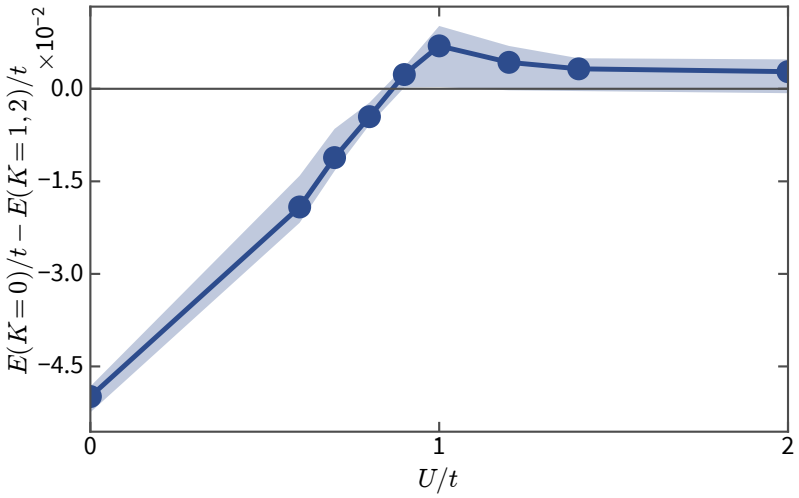

Figure 5.9: *Transition of K ground-state symmetry labels for $W = 3$.* For weak interactions $K = 0$ contains the lowest energy state, at large U, $K = 1$ or $K = 2$ comprise the ground state for different values of δ. Data are computed for $L = 33$, and averaged over the twist angles shown in fig. 5.8. The shaded region indicates minimal and maximal energy difference over those values of δ.

In fig. 5.9 we compare ground-state energies in different quasimomentum K sectors. We find that the critical interaction strength $U \approx 0.9t$ for the transition of ground-state symmetry sectors is consistent with results for $W = 2$. However, at this point we cannot say whether this transition is related to a change of topological invariants.

Width $W = 4$

Going to wider cylinders, we will not discuss the competition of different quasimomentum symmetry sectors in detail: For a range of intermediate interaction strengths, there is close competition between states of different K labels, and we are not entirely sure whether we resolve them accurately. Instead, we will focus on interaction strengths U, where a single K sector is the unique ground state—at least for the twist angles we study.

In fig. 5.10, $K = 2$ comprises the true ground state (for all δ) only for weak, or very strong interactions. In the gray shaded region, $0.8t \leq U \leq 4t$, states of different K labels become energetically degenerate, and we are not yet sure how to deal with this case.

Only studying $K = 2$, we find decent agreement with $\chi_{\text{Hall}} = 4$ for weak interactions. We are unable to establish integer quantization, but this may be attributed to the small range of twist angles, $\delta \in [13, 17] \times \pi/11$. Finally, we seem to observe the expected Hall response $\chi_{\text{Hall}} = 1/3$, albeit only for very strong interactions $U \geq 4t$.

The error in fig. 5.10 corresponds to minimal and maximal $\chi_{\text{Hall}}(\delta)$ observed. It seems intriguing that for $U \geq 4t$, we observe only a weak dependence on the twist angle,

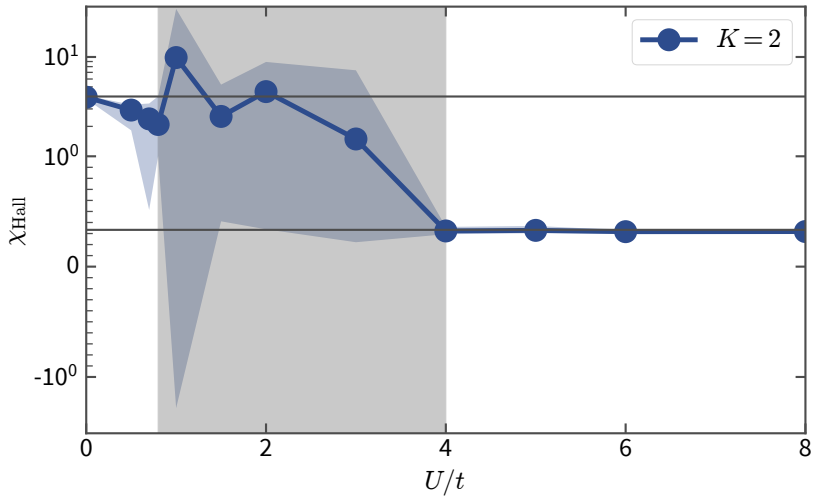

Figure 5.10: *Hall response over interaction U for $W = 4$, $L = 33$.* Data are averaged over twist angles $\delta \in [13, 17] \times \pi/11$. The quasimomentum $K = 2$ sector comprises the ground state for weak and strong interactions at these twist angles. However, in the gray region states for other values of K become degenerate. The "error" is determined from minimal and maximal χ_{Hall} in this range of twist angle δ.

$0.3 \leq \chi_{\text{Hall}}(\delta) \leq 0.35$. This might just be for a lucky choice of δ values, or that could mean that the twist-angle average is not necessary for these parameters and system dimensions.

Width $W = 6$

For $W = 6$, we find a unique ground state only for weak or strong interactions, similar to our observation for $W = 4$. This time, we find the energies for states in $K \in \{1, 3, 5\}$ to be energetically degenerate at intermediate interaction strengths.

We show the ground-state energies of all momentum sectors for an intermediate interaction strength $U = 3t$ in fig. 5.11. At this point, we have to wonder whether the degeneracy is actually related to the topological degeneracy of a fractional Chern insulator. In the setup of pumping via adiabatic flux insertion, cf. [141, 144, 191, 192], there need to be three degenerate ground states to allow for a $C/3$ quantization. However, we would have expected that the entire ground-state manifold lies in a single quasimomentum sector, and we are unsure how the different K sectors are adiabatically connected.

Putting the question of degenerate ground state at intermediate interaction strengths aside, we find agreement with $\chi_{\text{Hall}} = 4$ for weak, and $\chi_{\text{Hall}} = 1/3$ for strong interactions in fig. 5.12. In this plot we show data for all competing states $K \in \{1, 3, 5\}$, however $K = 3$ is the unique ground state in both limiting cases.

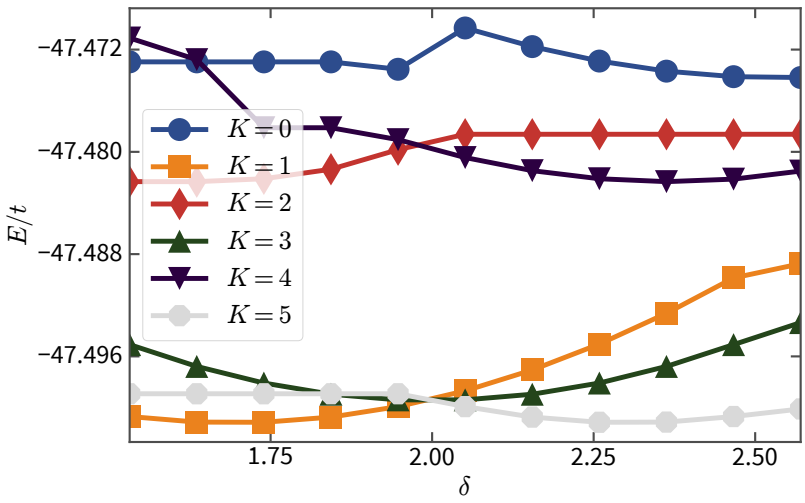

Figure 5.11: *Ground-state energies in different quasimomentum sectors for* $W = 6$ *and* $U = 3t$. For the range of twist angles δ shown here, the ground-state manifold seems to comprise states with quasimomentum symmetry labels $K \in \{1, 3, 5\}$. Data are computed for $L = 33$.

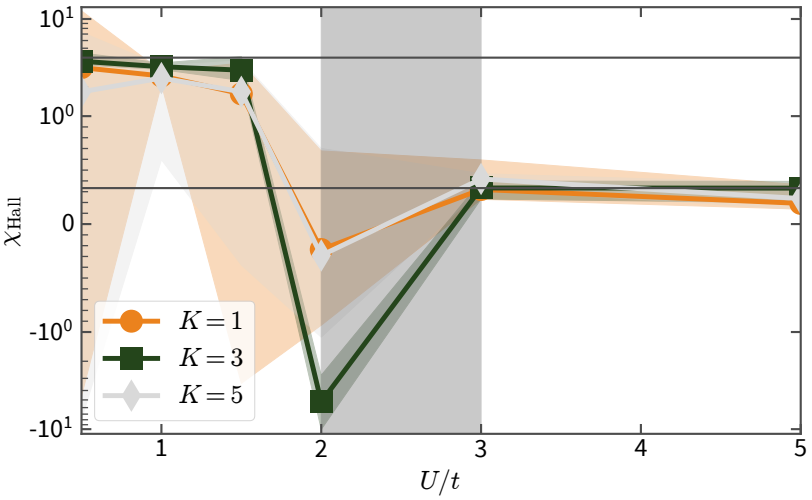

Figure 5.12: *Change of Hall response* χ_{Hall} *with interaction* U *for* $W = 6$. We only show data for $K \in \{1, 3, 5\}$, which are energetically degenerate for U in the gray shaded region, see fig. 5.11. The horizontal lines indicate $\chi_{\text{Hall}} \in \{1/3, 4\}$. Data for $K = 3$, which appears to be the unique ground state for both weak ($U \leq 1.5$) and strong interactions ($U > 3t$), agrees well with these (fractionally-) quantized values of the Hall response. The "error" is determined from minimal and maximal χ_{Hall} in this range of twist angle δ.

List of Figures

Bibliography

[1] L. Stenzel, A. L. C. Hayward, C. Hubig, U. Schollwöck, and F. Heidrich-Meisner. *Quantum phases and topological properties of interacting fermions in one-dimensional superlattices*. Phys. Rev. A **99**, 053614 (2019).

[2] L. Stenzel, A. L. C. Hayward, U. Schollwöck, and F. Heidrich-Meisner. *Topological phases in the Fermi-Hofstadter-Hubbard model on hybrid-space ladders*. Phys. Rev. A **102**, 023315 (2020).

[3] F. Duncan M. Haldane. *Nobel Lecture: Topological quantum matter*. Rev. Mod. Phys. **89**, 040502 (2017).

[4] K. v. Klitzing, G. Dorda, and M. Pepper. *New Method for High-Accuracy Determination of the Fine-Structure Constant Based on Quantized Hall Resistance*. Phys. Rev. Lett. **45**, 494–497 (1980).

[5] Nobel Media AB. *Scientific background: Topological phase transitions and topological phases of matter*. URL `www.nobelprize.org/prizes/physics/2016/advanced-information`.

[6] D. C. Tsui, H. L. Stormer, and A. C. Gossard. *Two-Dimensional Magnetotransport in the Extreme Quantum Limit*. Phys. Rev. Lett. **48**, 1559–1562 (1982).

[7] R. B. Laughlin. *Quantized Hall conductivity in two dimensions*. Phys. Rev. B **23**, 5632(R) (1981).

[8] B. I. Halperin. *Quantized Hall conductance, current-carrying edge states, and the existence of extended states in a two-dimensional disordered potential*. Phys. Rev. B **25**, 2185–2190 (1982).

[9] Yasuhiro Hatsugai. *Chern number and edge states in the integer quantum Hall effect*. Phys. Rev. Lett. **71**, 3697–3700 (1993).

[10] D. J. Thouless, M. Kohmoto, M. P. Nightingale, and M. den Nijs. *Quantized Hall Conductance in a Two-Dimensional Periodic Potential*. Phys. Rev. Lett. **49**, 405–408 (1982).

[11] Douglas R. Hofstadter. *Energy levels and wave functions of Bloch electrons in rational and irrational magnetic fields*. Phys. Rev. B **14**, 2239–2249 (1976).

[12] M. Aidelsburger, M. Atala, M. Lohse, J. T. Barreiro, B. Paredes, and I. Bloch. *Realization of the Hofstadter Hamiltonian with Ultracold Atoms in Optical Lattices*. Phys. Rev. Lett. **111**, 185301 (2013).

[13] Hirokazu Miyake, Georgios A. Siviloglou, Colin J. Kennedy, William Cody Burton, and Wolfgang Ketterle. *Realizing the Harper Hamiltonian with Laser-Assisted Tunneling in Optical Lattices*. Phys. Rev. Lett. **111**, 185302 (2013).

[14] P. Roushan, C. Neill, J. Tangpanitanon, V. M. Bastidas, A. Megrant, R. Barends, Y. Chen, Z. Chen, B. Chiaro, A. Dunsworth, A. Fowler, B. Foxen, M. Giustina, E. Jeffrey, J. Kelly, E. Lucero, J. Mutus, M. Neeley, C. Quintana, D. Sank, A. Vainsencher, J. Wenner, T. White, H. Neven, D. G. Angelakis, and J. Martinis. *Spectroscopic signatures of localization with interacting photons in superconducting qubits*. Science **358**, 1175–1179 (2017).

[15] Michael Victor Berry. *Quantal phase factors accompanying adiabatic changes*. Proc. R. Soc. Lond. A **392**, 45–57 (1984).

[16] Barry Simon. *Holonomy, the Quantum Adiabatic Theorem, and Berry's Phase*. Phys. Rev. Lett. **51**, 2167–2170 (1983).

[17] Michael V Berry. *The quantum phase, five years after*. Geometric phases in physics pages 7–28 (1989).

[18] F. D. M. Haldane. *Model for a Quantum Hall Effect without Landau Levels: Condensed-Matter Realization of the "Parity Anomaly"*. Phys. Rev. Lett. **61**, 2015–2018 (1988).

[19] Gregor Jotzu, Michael Messer, Rémi Desbuquois, Martin Lebrat, Thomas Uehlinger, Daniel Greif, and Tilman Esslinger. *Experimental realization of the topological Haldane model with ultracold fermions*. Nature **515**, 237–240 (2014).

[20] P Roushan, C Neill, Yu Chen, M Kolodrubetz, C Quintana, N Leung, M Fang, R Barends, B Campbell, Z Chen, B Chiaro, A Dunsworth, E Jeffrey, J Kelly, A Megrant, J Mutus, P. J. J. O'Malley, D Sank, A Vainsencher, J Wenner, T White, A Polkovnikov, A N Cleland, and J M Martinis. *Observation of topological transitions in interacting quantum circuits*. Nature **515**, 241–244 (2014).

[21] C. L. Kane and E. J. Mele. $\mathbb{Z}_2$ *Topological Order and the Quantum Spin Hall Effect*. Phys. Rev. Lett. **95**, 146802 (2005).

[22] B. Andrei Bernevig and Shou-Cheng Zhang. *Quantum Spin Hall Effect*. Phys. Rev. Lett. **96**, 106802 (2006).

[23] Markus König, Steffen Wiedmann, Christoph Brüne, Andreas Roth, Hartmut Buhmann, Laurens W. Molenkamp, Xiao-Liang Qi, and Shou-Cheng Zhang. *Quantum spin Hall insulator state in HgTe quantum wells*. Science **318**, 766 (2007).

[24] Joseph Maciejko, Taylor L. Hughes, and Shou-Cheng Zhang. *The Quantum Spin Hall Effect*. Annu. Rev. Condens. Matter Phys. **2**, 31 (2011).

[25] Xie Chen, Zheng-Cheng Gu, Zheng-Xin Liu, and Xiao-Gang Wen. *Symmetry protected topological orders and the group cohomology of their symmetry group*. Phys. Rev. B **87**, 155114 (2013).

[26] D. Jaksch and P. Zoller. *The cold atom Hubbard toolbox*. Annals of Physics **315**, 52 – 79 (2005). Special Issue.

[27] Immanuel Bloch, Jean Dalibard, and Wilhelm Zwerger. *Many-body physics with ultracold gases*. Rev. Mod. Phys. **80**, 885–964 (2008).

[28] Tomoki Ozawa, Hannah M. Price, Alberto Amo, Nathan Goldman, Mohammad Hafezi, Ling Lu, Mikael C. Rechtsman, David Schuster, Jonathan Simon, Oded Zilberberg, and Iacopo Carusotto. *Topological photonics*. Rev. Mod. Phys. **91**, 015006 (2019).

[29] P Roushan, C Neill, A Megrant, Y. Chen, R Babbush, R Barends, B Campbell, Z Chen, B Chiaro, A Dunsworth, A Fowler, E. Jeffrey, J Kelly, E Lucero, J Mutus, P. J. J. O'Malley, M Neeley, C Quintana, D Sank, A Vainsencher, J Wenner, T White, E Kapit, H Neven, and J Martinis. *Chiral ground-state currents of interacting photons in a synthetic magnetic field*. Nat. Phys. **13**, 146–151 (2017).

[30] N. R. Cooper, J. Dalibard, and I. B. Spielman. *Topological bands for ultracold atoms*. Rev. Mod. Phys. **91**, 015005 (2019).

[31] Jean Dalibard, Fabrice Gerbier, Gediminas Juzeliūnas, and Patrik Öhberg. *Colloquium: Artificial gauge potentials for neutral atoms*. Rev. Mod. Phys. **83**, 1523–1543 (2011).

[32] N Goldman, G Juzeliūnas, P Öhberg, and I B Spielman. *Light-induced gauge fields for ultracold atoms*. Reports on Progress in Physics **77**, 126401 (2014).
[33] Monika Aidelsburger, Sylvain Nascimbene, and Nathan Goldman. *Artificial gauge fields in materials and engineered systems*. Comp. Rend. Phys. **19**, 394–432 (2018).
[34] M. Aidelsburger, M. Atala, S. Nascimbène, S. Trotzky, Y.-A. Chen, and I. Bloch. *Experimental Realization of Strong Effective Magnetic Fields in an Optical Lattice*. Phys. Rev. Lett. **107**, 255301 (2011).
[35] M. Aidelsburger, M. Lohse, C. Schweizer, M. Atala, J. T. Barreiro, S. Nascimbene, N. R. Cooper, I. Bloch, and N. Goldman. *Measuring the Chern number of Hofstadter bands with ultracold bosonic atoms*. Nat. Phys. **11**, 162–166 (2015).
[36] A. Celi, P. Massignan, J. Ruseckas, N. Goldman, I. B. Spielman, G. Juzeliūnas, and M. Lewenstein. *Synthetic Gauge Fields in Synthetic Dimensions*. Phys. Rev. Lett. **112**, 043001 (2014).
[37] Fangzhao Alex An, Eric J. Meier, and Bryce Gadway. *Direct observation of chiral currents and magnetic reflection in atomic flux lattices*. Sci. Adv **3**, e1602685 (2017).
[38] Dario Hügel and Belén Paredes. *Chiral ladders and the edges of quantum Hall insulators*. Phys. Rev. A **89**, 023619 (2014).
[39] M. Mancini, G. Pagano, G. Cappellini, L. Livi, M. Rider, J. Catani, C. Sias, P. Zoller, M. Inguscio, M. Dalmonte, and L. Fallani. *Observation of chiral edge states with neutral fermions in synthetic Hall ribbons*. Science **349**, 1510–1513 (2015).
[40] B. K. Stuhl, H.-I. Lu, L. M. Aycock, D. Genkina, and I. B. Spielman. *Visualizing edge states with an atomic Bose gas in the quantum Hall regime*. Science **349**, 1514–1518 (2015).
[41] Dina Genkina, Lauren M Aycock, Hsin-I Lu, Mingwu Lu, Alina M Pineiro, and I B Spielman. *Imaging topology of Hofstadter ribbons*. New J. Phys. **21**, 053021 (2019).
[42] Jeong Ho Han, Jin Hyoun Kang, and Y. Shin. *Band Gap Closing in a Synthetic Hall Tube of Neutral Fermions*. Phys. Rev. Lett. **122**, 065303 (2019).
[43] Y.-J Lin, K Jiménez-García, and I B Spielman. *Spin-orbit-coupled Bose-Einstein condensates*. Nature **471**, 83–86 (2011).
[44] V. Galitski and I.B. Spielman. *Spin–orbit coupling in quantum gases*. Nature **494**, 49 (2013).
[45] L. F. Livi, G. Cappellini, M. Diem, L. Franchi, C. Clivati, M. Frittelli, F. Levi, D. Calonico, J. Catani, M. Inguscio, and L. Fallani. *Synthetic Dimensions and Spin-Orbit Coupling with an Optical Clock Transition*. Phys. Rev. Lett. **117**, 220401 (2016).
[46] Zhan Wu, Long Zhang, Wei Sun, Xiao-Tian Xu, Bao-Zong Wang, Si-Cong Ji, Youjin Deng, Shuai Chen, Xiong-Jun Liu, and Jian-Wei Pan. *Realization of two-dimensional spin-orbit coupling for Bose-Einstein condensates*. Science **354**, 83–88 (2016).
[47] S. Kolkowitz, S. L. Bromley, T. Bothwell, M. L. Wall, G. E. Marti, A. P. Koller, X. Zhang, A. M. Rey, and J. Ye. *Spin-orbit-coupled fermions in an optical lattice clock*. Nature **542**, 66–70 (2017).
[48] N. Goldman and J. Dalibard. *Periodically Driven Quantum Systems: Effective Hamiltonians and Engineered Gauge Fields*. Phys. Rev. X **4**, 031027 (2014).
[49] André Eckardt. *Colloquium: Atomic quantum gases in periodically driven optical lattices*. Rev. Mod. Phys. **89**, 011004 (2017).

[50] J. Struck, C. Ölschläger, M. Weinberg, P. Hauke, J. Simonet, A. Eckardt, M. Lewenstein, K. Sengstock, and P. Windpassinger. *Tunable Gauge Potential for Neutral and Spinless Particles in Driven Optical Lattices*. Phys. Rev. Lett. **108**, 225304 (2012).

[51] N. Fläschner, B. S. Rem, M. Tarnowski, D. Vogel, D.-S. Lühmann, K. Sengstock, and C. Weitenberg. *Experimental reconstruction of the Berry curvature in a Floquet Bloch band*. Science **352**, 1091–1094 (2016).

[52] Matthias Tarnowski, F Nur Ünal, Nick Fläschner, Benno S Rem, André Eckardt, Klaus Sengstock, and Christof Weitenberg. *Measuring topology from dynamics by obtaining the Chern number from a linking number*. Nat. Commun. **10**, 1728 (2019).

[53] Takuya Kitagawa, Erez Berg, Mark Rudner, and Eugene Demler. *Topological characterization of periodically driven quantum systems*. Phys. Rev. B **82**, 235114 (2010).

[54] Mark S. Rudner, Netanel H. Lindner, Erez Berg, and Michael Levin. *Anomalous Edge States and the Bulk-Edge Correspondence for Periodically Driven Two-Dimensional Systems*. Phys. Rev. X **3**, 031005 (2013).

[55] D. J. Thouless. *Quantization of particle transport*. Phys. Rev. B **27**, 6083–6087 (1983).

[56] Marcos Atala, Monika Aidelsburger, Julio T Barreiro, Dmitry Abanin, Takuya Kitagawa, Eugene Demler, and Immanuel Bloch. *Direct measurement of the Zak phase in topological Bloch bands*. Nat. Phys. **9**, 795–800 (2013).

[57] L. Duca, T. Li, M. Reitter, I. Bloch, M. Schleier-Smith, and U. Schneider. *An Aharonov-Bohm interferometer for determining Bloch band topology*. Science **347**, 288–292 (2015).

[58] M Lohse, C Schweizer, O Zilberberg, M Aidelsburger, and I Bloch. *A Thouless quantum pump with ultracold bosonic atoms in an optical superlattice*. Nat. Phys. **12**, 350–354 (2016).

[59] Shuta Nakajima, Takafumi Tomita, Shintaro Taie, Tomohiro Ichinose, Hideki Ozawa, Lei Wang, Matthias Troyer, and Yoshiro Takahashi. *Topological Thouless pumping of ultracold fermions*. Nat. Phys. **12**, 296–300 (2016).

[60] Shou-Cheng Zhang and Jiangping Hu. *A Four-Dimensional Generalization of the Quantum Hall Effect*. Science **294**, 823–828 (2001).

[61] Yaacov E. Kraus, Zohar Ringel, and Oded Zilberberg. *Four-Dimensional Quantum Hall Effect in a Two-Dimensional Quasicrystal*. Phys. Rev. Lett. **111**, 226401 (2013).

[62] Michael Lohse, Christian Schweizer, Hannah M Price, Oded Zilberberg, and Immanuel Bloch. *Exploring 4D quantum Hall physics with a 2D topological charge pump*. Nature **553**, 55–58 (2018).

[63] Stephan Rachel. *Interacting topological insulators: a review*. Reports on Progress in Physics **81**, 116501 (2018).

[64] M. Eric Tai, Alexander Lukin, Matthew Rispoli, Robert Schittko, Tim Menke, Dan Borgnia, Philipp M Preiss, Fabian Grusdt, Adam M Kaufman, and Markus Greiner. *Microscopy of the interacting Harper-Hofstadter model in the two-body limit*. Nature **546**, 519–523 (2017).

[65] Sylvain de Léséleuc, Vincent Lienhard, Pascal Scholl, Daniel Barredo, Sebastian Weber, Nicolai Lang, Hans Peter Büchler, Thierry Lahaye, and Antoine Browaeys. *Observation of a symmetry-protected topological phase of interacting bosons with Rydberg atoms*. Science **365**, 775 (2019).

[66] Luca D'Alessio and Marcos Rigol. *Long-time Behavior of Isolated Periodically Driven Interacting Lattice Systems*. Phys. Rev. X **4**, 041048 (2014).
[67] Achilleas Lazarides, Arnab Das, and Roderich Moessner. *Equilibrium states of generic quantum systems subject to periodic driving*. Phys. Rev. E **90**, 012110 (2014).
[68] M. Weinberg, C. Ölschläger, C. Sträter, S. Prelle, A. Eckardt, K. Sengstock, and J. Simonet. *Multiphoton interband excitations of quantum gases in driven optical lattices*. Phys. Rev. A **92**, 043621 (2015).
[69] Martin Reitter, Jakob Näger, Karen Wintersperger, Christoph Sträter, Immanuel Bloch, André Eckardt, and Ulrich Schneider. *Interaction Dependent Heating and Atom Loss in a Periodically Driven Optical Lattice*. Phys. Rev. Lett. **119**, 200402 (2017).
[70] Rémi Desbuquois, Michael Messer, Frederik Görg, Kilian Sandholzer, Gregor Jotzu, and Tilman Esslinger. *Controlling the Floquet state population and observing micromotion in a periodically driven two-body quantum system*. Phys. Rev. A **96**, 053602 (2017).
[71] Michael Messer, Kilian Sandholzer, Frederik Görg, Joaquín Minguzzi, Rémi Desbuquois, and Tilman Esslinger. *Floquet Dynamics in Driven Fermi-Hubbard Systems*. Phys. Rev. Lett. **121**, 233603 (2018).
[72] T. Boulier, J. Maslek, M. Bukov, C. Bracamontes, E. Magnan, S. Lellouch, E. Demler, N. Goldman, and J. V. Porto. *Parametric Heating in a 2D Periodically Driven Bosonic System: Beyond the Weakly Interacting Regime*. Phys. Rev. X **9**, 011047 (2019).
[73] K. Wintersperger, M. Bukov, J. Näger, S. Lellouch, E. Demler, U. Schneider, I. Bloch, N. Goldman, and M. Aidelsburger. *Parametric Instabilities of Interacting Bosons in Periodically Driven 1D Optical Lattices*. Phys. Rev. X **10**, 011030 (2020).
[74] Antonio Rubio-Abadal, Matteo Ippoliti, Simon Hollerith, David Wei, Jun Rui, S. L. Sondhi, Vedika Khemani, Christian Gross, and Immanuel Bloch. *Floquet Prethermalization in a Bose-Hubbard System*. Phys. Rev. X **10**, 021044 (2020).
[75] D. Tong. Lectures on the Quantum Hall Effect. e-print (2016), arXiv:1606.06687.
[76] T. Dittrich, I. Gert-Ludwig, P. Hänggi, B. Kramer, G. Schön, and W. Zwerger. *Quantum Transport and Dissipation*, chapter 2, pages 79–147. WILEY-VCH (1998). ISBN 978-3-527-29261-6.
[77] A. Altland and B. Simons. *Condensed Matter Field Theory*, chapter 9, pages 496–601. Cambridge University Press, 2 edition (2010). ISBN 978-0-521-76975-4.
[78] E. Fradkin. *Field Theories of Condensed Matter Physics*, chapter 12, pages 432–479. Cambridge University Press, 2 edition (2013). ISBN 978-0-521-76444-5.
[79] P. Coleman. *Introduction to Many-Body Physics*, chapter 18, pages 720–773. Cambridge University Press, 1 edition (2015). ISBN 978-0-521-86488-6.
[80] Klaus von Klitzing. *The quantized Hall effect*. Rev. Mod. Phys. **58**, 519–531 (1986).
[81] Th. Englert and K. Von Klitzing. *Analysis of ρ_{xx} minima in surface quantum oscillations on (100) n-type silicon inversion layers*. Surface Science **73**, 70 (1978).
[82] L. D. Landau and E. M. Lifschitz. *Quantenmechanik*, volume III of *Lehrbuch der theoretischen Physik*, chapter XV, pages 437–443. Akademie-Verlag, Berlin, 2 edition (1966).
[83] Jae-yoon Choi, Sebastian Hild, Johannes Zeiher, Peter Schauß, Antonio Rubio-Abadal, Tarik Yefsah, Vedika Khemani, David A. Huse, Immanuel Bloch, and

Christian Gross. *Exploring the many-body localization transition in two dimensions*. Science **352**, 1547–1552 (2016).

[84] Pranjal Bordia, Henrik Lüschen, Ulrich Schneider, Michael Knap, and Immanuel Bloch. *Periodically driving a many-body localized quantum system*. Nat. Phys. **13**, 460–464 (2017).

[85] Joseph E. Avron and Ruedi Seiler. *Quantization of the Hall Conductance for General, Multiparticle Schrödinger Hamiltonians*. Phys. Rev. Lett. **54**, 259 (1985).

[86] S. Pancharatnam. *Generalized theory of interference, and its applications*. Proceedings of the Indian Academy of Sciences - Section A **44**, 247–262 (1956).

[87] John Hamal Hubbard and Barbara Burke Hubbard. *Vector Calculus, Linear Algebra, and Differential Forms*, chapter 6, pages 564–703. Matrix Editions, Ithaca, NY, 5 edition (2015). ISBN 978-0-9715766-8-1.

[88] Di Xiao, Ming-Che Chang, and Qian Niu. *Berry phase effects on electronic properties*. Rev. Mod. Phys. **82**, 1959–2007 (2010).

[89] Ryogo Kubo. *Statistical-Mechanical Theory of Irreversible Processes. I. General Theory and Simple Applications to Magnetic and Conduction Problems*. Journal of the Physical Society of Japan **12**, 570–586 (1957).

[90] Henrik Bruus and Karsten Flensberg. *Many-body Quantum Theory in Condensed Matter Physics*, chapter 6, pages 92–101. Oxford University Press (2004). ISBN 978-0-19-856633-5.

[91] P. Coleman. *Introduction to Many-Body Physics*, chapter 9, pages 292–331. Cambridge University Press, 1 edition (2015). ISBN 978-0-521-86488-6.

[92] Thierry Giamarchi, Anibal Iucci, and Christophe Berthod. Introduction to Many Body physics. e-print (2013). URL `http://dqmp.unige.ch/giamarchi/local/people/thierry.giamarchi/pdf/many-body.pdf`.

[93] F. D. M. Haldane. *Model for a Quantum Hall Effect without Landau Levels: Condensed-Matter Realization of the "Parity Anomaly"*. Phys. Rev. Lett. **61**, 2015–2018 (1988).

[94] P. G. Harper. *The General Motion of Conduction Electrons in a Uniform Magnetic Field, with Application to the Diamagnetism of Metals*. Proc. Phys. Soc. A **68**, 879 (1955).

[95] G. H. Wannier. *A Result Not Dependent on Rationality for Bloch Electrons in a Magnetic Field*. physica status solidi (b) **88**, 757–765 (1978).

[96] N Goldman. *Characterizing the Hofstadter butterfly's outline with Chern numbers*. J. Phys. B: At. Mol. Opt. Phys. **42**, 055302 (2009).

[97] János K. Asbóth, László Oroszlány, and András Pályi. *A Short Course on Topological Insulators*, volume 919 of *Lecture Notes in Physics*. Springer International Publishing, Cham (2016). ISBN 978-3-319-25605-4. doi: 10.1007/978-3-319-25607-8.

[98] Lei Wang, Matthias Troyer, and Xi Dai. *Topological Charge Pumping in a One-Dimensional Optical Lattice*. Phys. Rev. Lett. **111**, 026802 (2013).

[99] Rui Li and Michael Fleischhauer. *Finite-size corrections to quantized particle transport in topological charge pumps*. Phys. Rev. B **96**, 085444 (2017).

[100] C. Schweizer, M. Lohse, R. Citro, and I. Bloch. *Spin Pumping and Measurement of Spin Currents in Optical Superlattices*. Phys. Rev. Lett. **117**, 170405 (2016).

[101] Yaacov E. Kraus, Yoav Lahini, Zohar Ringel, Mor Verbin, and Oded Zilberberg. *Topological States and Adiabatic Pumping in Quasicrystals*. Phys. Rev. Lett. **109**, 106402 (2012).

[102] Oded Zilberberg, Sheng Huang, Jonathan Guglielmon, Mohan Wang, Kevin P Chen, Yaacov E. Kraus, and Mikael C Rechtsman. *Photonic topological boundary pumping as a probe of 4D quantum Hall physics*. Nature **553**, 59–62 (2018).

[103] Serge Aubry and Gilles André. *Analyticity breaking and Anderson localization in incommensurate lattices*. Ann. Israel Phys. Soc **3**, 18 (1980).

[104] S. Das Sarma, Song He, and X. C. Xie. *Mobility edge in a model one-dimensional potential*. Phys. Rev. Lett. **61**, 2144–2147 (1988).

[105] D. J. Thouless. *Localization by a Potential with Slowly Varying Period*. Phys. Rev. Lett. **61**, 2141–2143 (1988).

[106] S. Das Sarma, Song He, and X. C. Xie. *Localization, mobility edges, and metal-insulator transition in a class of one-dimensional slowly varying deterministic potentials*. Phys. Rev. B **41**, 5544–5565 (1990).

[107] J. Biddle, B. Wang, D. J. Priour, and S. Das Sarma. *Localization in one-dimensional incommensurate lattices beyond the Aubry-André model*. Phys. Rev. A **80**, 021603 (2009).

[108] Y. Lahini, R. Pugatch, F. Pozzi, M. Sorel, R. Morandotti, N. Davidson, and Y. Silberberg. *Observation of a Localization Transition in Quasiperiodic Photonic Lattices*. Phys. Rev. Lett. **103**, 013901 (2009).

[109] J. Biddle and S. Das Sarma. *Predicted Mobility Edges in One-Dimensional Incommensurate Optical Lattices: An Exactly Solvable Model of Anderson Localization*. Phys. Rev. Lett. **104**, 070601 (2010).

[110] Michael Schreiber, Sean S. Hodgman, Pranjal Bordia, Henrik P. Lüschen, Mark H. Fischer, Ronen Vosk, Ehud Altman, Ulrich Schneider, and Immanuel Bloch. *Observation of many-body localization of interacting fermions in a quasirandom optical lattice*. Science **349**, 842–845 (2015).

[111] G. Roati, C. D'Errico, L. Fallani, M. Fattori, C. Fort, M. Zaccanti, G. Modugno, M. Modugno, and M. Inguscio. *Anderson localization of a non-interacting Bose-Einstein condensate*. Nature **453**, 895 (2008).

[112] Q Niu and D J Thouless. *Quantised adiabatic charge transport in the presence of substrate disorder and many-body interaction*. J. Phys. A: Math. Gen. **17**, 2453–2462 (1984).

[113] Qian Niu, D. J. Thouless, and Yong-Shi Wu. *Quantized Hall conductance as a topological invariant*. Phys. Rev. B **31**, 3372–3377 (1985).

[114] Haruki Watanabe. *Insensitivity of bulk properties to the twisted boundary condition*. Phys. Rev. B **98**, 155137 (2018).

[115] Matthew B. Hastings and Spyridon Michalakis. *Quantization of Hall Conductance for Interacting Electrons on a Torus*. Commun. Math. Phys. **334**, 433–471 (2015).

[116] Koji Kudo, Haruki Watanabe, Toshikaze Kariyado, and Yasuhiro Hatsugai. *Many-Body Chern Number without Integration*. Phys. Rev. Lett. **122**, 146601 (2019).

[117] Steven R. White. *Density matrix formulation for quantum renormalization groups*. Phys. Rev. Lett. **69**, 2863–2866 (1992).

[118] U. Schollwöck. *The density-matrix renormalization group*. Rev. Mod. Phys. **77**, 259–315 (2005).

[119] Ulrich Schollwöck. *The density-matrix renormalization group in the age of matrix product states*. Annals of Physics **326**, 96 – 192 (2011). January 2011 Special Issue.

[120] Claudius Hubig, Felix Lachenmaier, Nils-Oliver Linden, Teresa Reinhard, Leo Stenzel, Andreas Swoboda, and Martin Grundner. *The* SyTen *Toolkit*. URL https://syten.eu.

[121] Claudius Hubig. *Symmetry-Protected Tensor Networks*. PhD thesis, LMU München (2017). URL https://edoc.ub.uni-muenchen.de/21348/. urn:nbn:de:bvb:19-213484.

[122] Stefan Rommer and Stellan Östlund. *Class of ansatz wave functions for one-dimensional spin systems and their relation to the density matrix renormalization group*. Phys. Rev. B **55**, 2164–2181 (1997).

[123] J Dukelsky, M. A Martín-Delgado, T Nishino, and G Sierra. *Equivalence of the variational matrix product method and the density matrix renormalization group applied to spin chains*. EPL **43**, 457–462 (1998).

[124] Steven R. White. *Density matrix renormalization group algorithms with a single center site*. Phys. Rev. B **72**, 180403(R) (2005).

[125] C. Hubig, I. P. McCulloch, U. Schollwöck, and F. A. Wolf. *Strictly single-site DMRG algorithm with subspace expansion*. Phys. Rev. B **91**, 155115 (2015).

[126] C. Hubig, I. P. McCulloch, and U. Schollwöck. *Generic construction of efficient matrix product operators*. Phys. Rev. B **95**, 035129 (2017).

[127] M B Hastings. *An area law for one-dimensional quantum systems*. J. Stat. Mech. **2007**, P08024–P08024 (2007).

[128] J. Eisert, M. Cramer, and M. B. Plenio. *Colloquium: Area laws for the entanglement entropy*. Rev. Mod. Phys. **82**, 277–306 (2010).

[129] F. Verstraete and J. I. Cirac. *Matrix product states represent ground states faithfully*. Phys. Rev. B **73**, 094423 (2006).

[130] Garnet Kin-Lic Chan and Martin Head-Gordon. *Highly correlated calculations with a polynomial cost algorithm: A study of the density matrix renormalization group*. J. Chem. Phys. **116**, 4462–4476 (2002).

[131] Ö. Legeza and J. Sólyom. *Optimizing the density-matrix renormalization group method using quantum information entropy*. Phys. Rev. B **68**, 195116 (2003).

[132] A. O. Mitrushenkov, Roberto Linguerri, Paolo Palmieri, and Guido Fano. *Quantum chemistry using the density matrix renormalization group II*. J. Chem. Phys. **119**, 4148–4158 (2003).

[133] Gerrit Moritz, Bernd Artur Hess, and Markus Reiher. *Convergence behavior of the density-matrix renormalization group algorithm for optimized orbital orderings*. J. Chem. Phys. **122**, 024107 (2005).

[134] E. Fertitta, B. Paulus, G. Barcza, and Ö. Legeza. *Investigation of metal–insulator-like transition through the ab initio density matrix renormalization group approach*. Phys. Rev. B **90**, 245129 (2014).

[135] F. Verstraete and J. I. Cirac. Renormalization algorithms for Quantum-Many Body Systems in two and higher dimensions. e-print (2004), arXiv:cond-mat/0407066.

[136] J. Jordan, R. Orús, G. Vidal, F. Verstraete, and J. I. Cirac. *Classical simulation of infinite-size quantum lattice systems in two spatial dimensions*. Phys. Rev. Lett. **101**, 250602 (2008).

[137] E.M. Stoudenmire and Steven R. White. *Studying Two-Dimensional Systems with*

the Density Matrix Renormalization Group. Annu. Rev. Condens. Matter Phys. **3**, 111–128 (2012).

[138] Juan Osorio Iregui, Matthias Troyer, and Philippe Corboz. *Infinite matrix product states versus infinite projected entangled-pair states on the cylinder: A comparative study*. Phys. Rev. B **96**, 115113 (2017).

[139] Bo-Xiao Zheng, Chia-Min Chung, Philippe Corboz, Georg Ehlers, Ming-Pu Qin, Reinhard M. Noack, Hao Shi, Steven R. White, Shiwei Zhang, and Garnet Kin-Lic Chan. *Stripe order in the underdoped region of the two-dimensional Hubbard model*. Science **358**, 1155–1160 (2017).

[140] A. A. Aligia, C. D. Batista, and F. H. L. Eßler. *Numerical method for detecting incommensurate correlations in the Heisenberg zigzag ladder*. Phys. Rev. B **62**, 3259–3263 (2000).

[141] Adolfo G. Grushin, Johannes Motruk, Michael P. Zaletel, and Frank Pollmann. *Characterization and stability of a fermionic $\nu = 1/3$ fractional Chern insulator*. Phys. Rev. B **91**, 035136 (2015).

[142] W. Zhu, Shou-Shu Gong, Tian-Sheng Zeng, Liang Fu, and D. N. Sheng. *Interaction-Driven Spontaneous Quantum Hall Effect on a Kagome Lattice*. Phys. Rev. Lett. **117**, 096402 (2016).

[143] G. Ehlers, J. Sólyom, Ö. Legeza, and R. M. Noack. *Entanglement structure of the Hubbard model in momentum space*. Phys. Rev. B **92**, 235116 (2015).

[144] Johannes Motruk, Michael P. Zaletel, Roger S. K. Mong, and Frank Pollmann. *Density matrix renormalization group on a cylinder in mixed real and momentum space*. Phys. Rev. B **93**, 155139 (2016).

[145] Leo Stenzel. A DMRG study of the Fermi-Hubbard model in hybrid space. Master's thesis (2016). URL `https://www.theorie.physik.uni-muenchen.de/TMP/theses/thesisstenzel.pdf`.

[146] G. Ehlers, S. R. White, and R. M. Noack. *Hybrid-space density matrix renormalization group study of the doped two-dimensional Hubbard model*. Phys. Rev. B **95**, 125125 (2017).

[147] I. P McCulloch and M Gulácsi. *The non-Abelian density matrix renormalization group algorithm*. EPL **57**, 852–858 (2002).

[148] Natalia Chepiga. *Dimerization and exotic criticality in spin-S chains*. PhD thesis, EPFL Lausanne (2017). URL `http://infoscience.epfl.ch/record/226465`. urn:nbn:ch:bel-epfl-thesis7621-7.

[149] Takahiro Fukui, Yasuhiro Hatsugai, and Hiroshi Suzuki. *Chern Numbers in Discretized Brillouin Zone: Efficient Method of Computing (Spin) Hall Conductances*. J. Phys. Soc. Japan **74**, 1674–1677 (2005).

[150] E M Stoudenmire and Steven R White. *Minimally entangled typical thermal state algorithms*. New J. Phys. **12**, 055026 (2010).

[151] Sebastian Paeckel, Thomas Köhler, Andreas Swoboda, Salvatore R. Manmana, Ulrich Schollwöck, and Claudius Hubig. *Time-evolution methods for matrix-product states*. Ann. Phys. (N. Y.) **411**, 167998 (2019).

[152] C. Hubig, J. Haegeman, and U. Schollwöck. *Error estimates for extrapolations with matrix-product states*. Phys. Rev. B **97**, 045125 (2018).

[153] Dougal Maclaurin, David Duvenaud, Matt Johnson, and Jamie Townsend. *Autograd package for Python and Numpy code*. URL `https://github.com/HIPS/autograd`.

[154] Zhihao Xu and Shu Chen. *Topological Mott insulators of ultracold atomic mixtures induced by interactions in one-dimensional optical superlattices*. Phys. Rev. B **88**, 045110 (2013).

[155] Haiping Hu, Shu Chen, Tian-Sheng Zeng, and Chuanwei Zhang. *Topological Mott insulator with bosonic edge modes in one-dimensional fermionic superlattices*. Phys. Rev. A **100**, 023616 (2019).

[156] L. Barbiero, L. Santos, and N. Goldman. *Quenched dynamics and spin-charge separation in an interacting topological lattice*. Phys. Rev. B **97**, 201115(R) (2018).

[157] Masaya Nakagawa, Tsuneya Yoshida, Robert Peters, and Norio Kawakami. *Breakdown of topological Thouless pumping in the strongly interacting regime*. Phys. Rev. B **98**, 115147 (2018).

[158] A. Hayward, C. Schweizer, M. Lohse, M. Aidelsburger, and F. Heidrich-Meisner. *Topological Charge Pumping in the Interacting Bosonic Rice-Mele Model*. Phys. Rev. B **98**, 245148 (2018).

[159] M J Rice and E J Mele. *Elementary Excitations of a Linearly Conjugated Diatomic Polymer*. Phys. Rev. Lett. **49**, 1455–1459 (1982).

[160] Shi-Liang Zhu, Z.-D Wang, Y.-H Chan, and L.-M Duan. *Topological Bose-Mott Insulators in a One-Dimensional Optical Superlattice*. Phys. Rev. Lett. **110**, 075303 (2013).

[161] Xiaolong Deng and Luis Santos. *Topological transitions of interacting bosons in one-dimensional bichromatic optical lattices*. Phys. Rev. A **89**, 033632 (2014).

[162] Tianhe Li, Huaiming Guo, Shu Chen, and Shun-Qing Shen. *Complete phase diagram and topological properties of interacting bosons in one-dimensional superlattices*. Phys. Rev. B **91**, 134101 (2015).

[163] Yoshihito Kuno, Keita Shimizu, and Ikuo Ichinose. *Various topological Mott insulators and topological bulk charge pumping in strongly-interacting boson system in one-dimensional superlattice*. New J. Phys. **19**, 123025 (2017).

[164] Zheng-Wei Zuo, Guo-Ling Li, and Liben Li. *Statistically induced topological phase transitions in a one-dimensional superlattice anyon-Hubbard model*. Phys. Rev. B **97**, 115126 (2018).

[165] T Egami, S Ishihara, and M Tachiki. *Lattice effect of strong electron correlation: Implication for ferroelectricity and superconductivity*. Science **261**, 1307–1310 (1993).

[166] Michele Fabrizio, Alexander O Gogolin, and Alexander A Nersesyan. *From band insulator to Mott insulator in one dimension*. Phys. Rev. Lett. **83**, 2014 (1999).

[167] Yasutami Takada and Manabu Kido. *Effect of Electron Correlation on the Bragg Reflection*. J. Phys. Soc. Japan **70**, 21–24 (2001).

[168] Shoji Yamamoto. *Pressure-induced phase transitions of halogen-bridged binuclear metal complexes* $R_4[Pt_2(P_2O_5H_2)_4X] \cdot nH_2O$. Phys. Rev. B **64**, 140102(R) (2001).

[169] M. E. Torio, A. A. Aligia, and H. A. Ceccatto. *Phase diagram of the Hubbard chain with two atoms per cell*. Phys. Rev. B **64**, 121105(R) (2001).

[170] Arno P Kampf, M Sekania, GI Japaridze, and Ph Brune. *Nature of the insulating phases in the half-filled ionic Hubbard model*. J. Phys. Condens. Matter **15**, 5895 (2003).

[171] Jizhong Lou, Shaojin Qin, Tao Xiang, Changfeng Chen, Guang-Shan Tian, and Zhaobin Su. *Transition from band insulator to Mott insulator in one dimension: Critical behavior and phase diagram*. Phys. Rev. B **68**, 045110 (2003).

[172] A. A. Aligia. *Charge dynamics in the Mott insulating phase of the ionic Hubbard model*. Phys. Rev. B **69**, 041101(R) (2004).

[173] C. D. Batista and A. A. Aligia. *Exact Bond Ordered Ground State for the Transition between the Band and the Mott Insulator*. Phys. Rev. Lett. **92**, 246405 (2004).

[174] S. R. Manmana, V. Meden, R. M. Noack, and K. Schönhammer. *Quantum critical behavior of the one-dimensional ionic Hubbard model*. Phys. Rev. B **70**, 155115 (2004).

[175] Hiromi Otsuka and Masaaki Nakamura. *Ground-state phase diagram of the one-dimensional Hubbard model with an alternating chemical potential*. Phys. Rev. B **71**, 155105 (2005).

[176] P. Lombardo, R. Hayn, and G. I. Japaridze. *Insulator-metal-insulator transition and selective spectral-weight transfer in a disordered strongly correlated system*. Phys. Rev. B **74**, 085116 (2006).

[177] S. S. Kancharla and E. Dagotto. *Metallic interface at the boundary between band and Mott insulators*. Phys. Rev. B **74**, 195427 (2006).

[178] M. E. Torio, A. A. Aligia, G. I. Japaridze, and B. Normand. *Quantum phase diagram of the generalized ionic Hubbard model for AB_n chains*. Phys. Rev. B **73**, 115109 (2006).

[179] N. Paris, K. Bouadim, F. Hebert, G. G. Batrouni, and R. T. Scalettar. *Quantum Monte Carlo Study of an Interaction-Driven Band-Insulator–to–Metal Transition*. Phys. Rev. Lett. **98**, 046403 (2007).

[180] Krzysztof Byczuk, Michael Sekania, Walter Hofstetter, and Arno P. Kampf. *Insulating behavior with spin and charge order in the ionic Hubbard model*. Phys. Rev. B **79**, 121103(R) (2009).

[181] L. Tincani, R. M. Noack, and D. Baeriswyl. *Critical properties of the band-insulator-to-Mott-insulator transition in the strong-coupling limit of the ionic Hubbard model*. Phys. Rev. B **79**, 165109 (2009).

[182] Arti Garg, H. R. Krishnamurthy, and Mohit Randeria. *Doping a Correlated Band Insulator: A New Route to Half-Metallic Behavior*. Phys. Rev. Lett. **112**, 106406 (2014).

[183] L S Murcia-Correa, R Franco, and J Silva-Valencia. *Quantum phases of AB_2 fermionic chains*. J. Phys.: Conf. Ser. **687**, 012066 (2016).

[184] Karla Loida, Jean-Sébastien Bernier, Roberta Citro, Edmond Orignac, and Corinna Kollath. *Probing the Bond Order Wave Phase Transitions of the Ionic Hubbard Model by Superlattice Modulation Spectroscopy*. Phys. Rev. Lett. **119**, 230403 (2017).

[185] J. Hubbard and Brian Hilton Flowers. *Electron correlations in narrow energy bands*. Proc. R. Soc. Lond. A **276**, 238–257 (1963).

[186] Tian-Sheng Zeng, Ce Wang, and Hui Zhai. *Charge Pumping of Interacting Fermion Atoms in the Synthetic Dimension*. Phys. Rev. Lett. **115**, 095302 (2015).

[187] Luca Taddia, Eyal Cornfeld, Davide Rossini, Leonardo Mazza, Eran Sela, and Rosario Fazio. *Topological Fractional Pumping with Alkaline-Earth-Like Atoms in Synthetic Lattices*. Phys. Rev. Lett. **118**, 230402 (2017).

[188] J. E. Avron, R Seiler, and B Simon. *Homotopy and Quantization in Condensed Matter Physics*. Phys. Rev. Lett. **51**, 51–53 (1983).

[189] Pasquale Marra, Roberta Citro, and Carmine Ortix. *Fractional quantization of the topological charge pumping in a one-dimensional superlattice*. Phys. Rev. B **91**, 125411 (2015).

[190] Pasquale Marra and Roberta Citro. *Fractional quantization of charge and spin in topological quantum pumps*. Eur. Phys. J. Spec. Top. **226**, 2781–2791 (2017).

[191] Johannes Motruk and Frank Pollmann. *Phase transitions and adiabatic preparation of a fractional Chern insulator in a boson cold-atom model*. Phys. Rev. B **96**, 165107 (2017).

[192] Leon Schoonderwoerd, Frank Pollmann, and Gunnar Möller. Interaction-driven plateau transition between integer and fractional Chern Insulators. e-print (2019), arXiv:1908.00988.

[193] Ari M Turner, Frank Pollmann, and Erez Berg. *Topological phases of one-dimensional fermions: An entanglement point of view*. Phys. Rev. B **83**, 075102 (2011).

[194] J Sirker, M Maiti, N P Konstantinidis, and N Sedlmayr. *Boundary fidelity and entanglement in the symmetry protected topological phase of the SSH model*. J. Stat. Mech. Theor. Exp. **2014**, P10032 (2014).

[195] Fabian HL Essler, Holger Frahm, Frank Göhmann, Andreas Klümper, and Vladimir E Korepin. *The one-dimensional Hubbard model*. Cambridge University Press (2005).

[196] Ulrich Schollwöck, Johannes Richter, Damian JJ Farnell, and Raymond F Bishop. *Quantum magnetism*, volume 645. Springer (2008).

[197] Andreas Sorge. *pyfssa 0.7.6*. Zenodo (2015).

[198] O. Melchert. autoScale.py—A program for automatic finite-size scaling analyses: A user's guide. e-print (2009), arXiv:0910.5403.

[199] Shaojin Qin, Tai-Kai Ng, and Zhao-Bin Su. *Edge states in open antiferromagnetic Heisenberg chains*. Phys. Rev. B **52**, 12844–12848 (1995).

[200] Andrew M. Essin and Victor Gurarie. *Bulk-boundary correspondence of topological insulators from their respective Green's functions*. Phys. Rev. B **84**, 125132 (2011).

[201] Y. Hatsugai and T. Fukui. *Bulk-edge correspondence in topological pumping*. Phys. Rev. B **94**, 041102(R) (2016).

[202] H. M. Price and N. R. Cooper. *Mapping the Berry curvature from semiclassical dynamics in optical lattices*. Phys. Rev. A **85**, 033620 (2012).

[203] H. M. Price, O. Zilberberg, T. Ozawa, I. Carusotto, and N. Goldman. *Measurement of Chern numbers through center-of-mass responses*. Phys. Rev. B **93**, 245113 (2016).

[204] Samuel Mugel, Alexandre Dauphin, Pietro Massignan, Leticia Tarruell, Maciej Lewenstein, Carlos Lobo, and Alessio Celi. *Measuring Chern numbers in Hofstadter strips*. SciPost Phys. **3**, 012 (2017).

[205] Alexandre Dauphin and Nathan Goldman. *Extracting the Chern Number from the Dynamics of a Fermi Gas: Implementing a Quantum Hall Bar for Cold Atoms*. Phys. Rev. Lett. **111**, 135302 (2013).

[206] C. Repellin, J. Léonard, and N. Goldman. Hall drift of fractional Chern insulators in few-boson systems. e-print (2020), arXiv:2005.09689.

[207] Johannes Motruk and Ilyoun Na. Detecting fractional Chern insulators in optical lattices through quantized displacement. e-print (2020), arXiv:2005.09860.

[208] Sebastian Greschner, Michele Filippone, and Thierry Giamarchi. *Universal Hall Response in Interacting Quantum Systems*. Phys. Rev. Lett. **122**, 083402 (2019).
[209] Takeshi Y. Saito and Shunsuke Furukawa. *Devil's staircases in synthetic dimensions and gauge fields*. Phys. Rev. A **95**, 043613 (2017).
[210] Nicola Marzari, Arash A. Mostofi, Jonathan R. Yates, Ivo Souza, and David Vanderbilt. *Maximally localized Wannier functions: Theory and applications*. Rev. Mod. Phys. **84**, 1419–1475 (2012).
[211] Sinisa Coh and David Vanderbilt. *Electric Polarization in a Chern Insulator*. Phys. Rev. Lett. **102**, 107603 (2009).
[212] Fabian Grusdt and Michael Höning. *Realization of fractional Chern insulators in the thin-torus limit with ultracold bosons*. Phys. Rev. A **90**, 053623 (2014).
[213] Jutho Haegeman, Christian Lubich, Ivan Oseledets, Bart Vandereycken, and Frank Verstraete. *Unifying time evolution and optimization with matrix product states*. Phys. Rev. B **94**, 165116 (2016).
[214] Mikito Koshino and Tsuneya Ando. *Quantum Hall Effect on the Hofstadter Butterfly*. J. Phys. Soc. Jpn. **73**, 3243–3246 (2004).
[215] Dario Hügel, Hugo U. R. Strand, Philipp Werner, and Lode Pollet. *Anisotropic Harper-Hofstadter-Mott model: Competition between condensation and magnetic fields*. Phys. Rev. B **96**, 054431 (2017).
[216] Vieri Mastropietro. *Persistence of gaps in the interacting anisotropic Hofstadter model*. Phys. Rev. B **99**, 155154 (2019).
[217] L. Tanzi, C. R. Cabrera, J. Sanz, P. Cheiney, M. Tomza, and L. Tarruell. *Feshbach resonances in potassium Bose-Bose mixtures*. Phys. Rev. A **98**, 062712 (2018).
[218] Wei-Lin Tu, Frank Schindler, Titus Neupert, and Didier Poilblanc. *Competing orders in the Hofstadter t-J model*. Phys. Rev. B **97**, 035154 (2018).
[219] Gyu-Boong Jo, Ye-Ryoung Lee, Jae-Hoon Choi, Caleb A. Christensen, Tony H. Kim, Joseph H. Thywissen, David E. Pritchard, and Wolfgang Ketterle. *Itinerant Ferromagnetism in a Fermi Gas of Ultracold Atoms*. Science **325**, 1521–1524 (2009).
[220] J. Spatek and A.M. Oleś. *Ferromagnetism in narrow s-band with inclusion of intersite correlations*. Physica B+C **86-88**, 375 – 377 (1977).
[221] Jozef Spalek. t-J model then and now: A personal perspective from the pioneering times. e-print (2007), arXiv:0706.4236.
[222] Horst L. Stormer, Daniel C. Tsui, and Arthur C. Gossard. *The fractional quantum Hall effect*. Rev. Mod. Phys. **71**, S298–S305 (1999).
[223] Ady Stern. *Anyons and the quantum Hall effect—A pedagogical review*. Annals of Physics **323**, 204–249 (2008).
[224] Chetan Nayak, Steven H. Simon, Ady Stern, Michael Freedman, and Sankar Das Sarma. *Non-Abelian anyons and topological quantum computation*. Rev. Mod. Phys. **80**, 1083–1159 (2008).
[225] D.N. Sheng, Zheng-Cheng Gu, Kai Sun, and L. Sheng. *Fractional quantum Hall effect in the absence of Landau levels*. Nat. Commun. **2**, 389 (2011).
[226] M. Gerster, M. Rizzi, P. Silvi, M. Dalmonte, and S. Montangero. *Fractional quantum Hall effect in the interacting Hofstadter model via tensor networks*. Phys. Rev. B **96**, 195123 (2017).

[227] N. Regnault and B. Andrei Bernevig. *Fractional Chern Insulator*. Phys. Rev. X **1**, 021014 (2011).
[228] Titus Neupert, Luiz Santos, Claudio Chamon, and Christopher Mudry. *Fractional Quantum Hall States at Zero Magnetic Field*. Phys. Rev. Lett. **106**, 236804 (2011).
[229] Yang-Le Wu, B. Andrei Bernevig, and N. Regnault. *Zoology of fractional Chern insulators*. Phys. Rev. B **85**, 075116 (2012).
[230] Michael P. Zaletel, Roger S. K. Mong, and Frank Pollmann. *Topological Characterization of Fractional Quantum Hall Ground States from Microscopic Hamiltonians*. Phys. Rev. Lett. **110**, 236801 (2013).
[231] Adolfo G. Grushin, Álvaro Gómez-León, and Titus Neupert. *Floquet Fractional Chern Insulators*. Phys. Rev. Lett. **112**, 156801 (2014).
[232] Xiao-Yu Dong, Adolfo G. Grushin, Johannes Motruk, and Frank Pollmann. *Charge Excitation Dynamics in Bosonic Fractional Chern Insulators*. Phys. Rev. Lett. **121**, 086401 (2018).
[233] Scott D. Geraedts, Michael P. Zaletel, Roger S. K. Mong, Max A. Metlitski, Ashvin Vishwanath, and Olexei I. Motrunich. *The half-filled Landau level: The case for Dirac composite fermions*. Science **352**, 197–201 (2016).
[234] Paolo Rosson, Michael Lubasch, Martin Kiffner, and Dieter Jaksch. *Bosonic fractional quantum Hall states on a finite cylinder*. Phys. Rev. A **99**, 033603 (2019).
[235] Hui Li and F. D. M. Haldane. *Entanglement Spectrum as a Generalization of Entanglement Entropy: Identification of Topological Order in Non-Abelian Fractional Quantum Hall Effect States*. Phys. Rev. Lett. **101**, 010504 (2008).
[236] Alexandru Petrescu and Karyn Le Hur. *Chiral Mott insulators, Meissner effect, and Laughlin states in quantum ladders*. Phys. Rev. B **91**, 054520 (2015).
[237] Marcello Calvanese Strinati, Eyal Cornfeld, Davide Rossini, Simone Barbarino, Marcello Dalmonte, Rosario Fazio, Eran Sela, and Leonardo Mazza. *Laughlin-like States in Bosonic and Fermionic Atomic Synthetic Ladders*. Phys. Rev. X **7**, 021033 (2017).
[238] Alexandru Petrescu, Marie Piraud, Guillaume Roux, I. P. McCulloch, and Karyn Le Hur. *Precursor of the Laughlin state of hard-core bosons on a two-leg ladder*. Phys. Rev. B **96**, 014524 (2017).
[239] Egidijus Anisimovas, Giedrius Žlabys, Brandon M. Anderson, Gediminas Juzeliūnas, and André Eckardt. *Role of real-space micromotion for bosonic and fermionic Floquet fractional Chern insulators*. Phys. Rev. B **91**, 245135 (2015).
[240] Mantas Račiūnas, Giedrius Žlabys, André Eckardt, and Egidijus Anisimovas. *Modified interactions in a Floquet topological system on a square lattice and their impact on a bosonic fractional Chern insulator state*. Phys. Rev. A **93**, 043618 (2016).
[241] Jong Yeon Lee, Chong Wang, Michael P. Zaletel, Ashvin Vishwanath, and Yin-Chen He. *Emergent Multi-Flavor* QED_3 *at the Plateau Transition between Fractional Chern Insulators: Applications to Graphene Heterostructures*. Phys. Rev. X **8**, 031015 (2018).